UNIVERSIDADE FEDERAL DE SÃO CARLOS
CENTRO DE CIÊNCIAS EXATAS E DE TECNOLOGIA
DEPARTAMENTO DE QUÍMICA
PROGRAMA DE PÓS-GRADUAÇÃO EM QUÍMICA

3D-printed aerogels and solution-blow spun fibers modified with metal-organic framework/molybdenum disulfide for adsorption and photodegradation of environmental contaminants

Ana Laura Martins Mulkson Alves*

Thesis presented as a part of the requirements to obtain a Ph.D. DEGREE in SCIENCES, concentration area: CHEMISTRY.

Advisor: Dr. Daniel Souza Corrêa

***Scholarship: CAPES**

São Carlos – SP
2025

UNIVERSIDADE FEDERAL DE SÃO CARLOS

Centro de Ciências Exatas e de Tecnologia
Programa de Pós-Graduação em Química

Folha de Aprovação

Defesa de Tese de Doutorado da candidata Ana Laura Martins Mulkson Alves, realizada em 31/01/2025.

Comissão Julgadora:

Prof. Dr. Daniel Souza Correa (EMBRAPA)

Profa. Dra. Luiza Amim Mercante (UFBA)

Prof. Dr. Thiers Massami Uehara (Protech PD)

Profa. Dra. Raquel Fernandes Pupo Nogueira (UNESP)

Prof. Dr. Eduardo Bessa Azevedo (IQSC/USP)

O Relatório de Defesa assinado pelos membros da Comissão Julgadora encontra-se arquivado junto ao Programa de Pós-Graduação em Química.

“Não sei o quanto o mundo é bom
Mas ele está melhor
Desde que você chegou
E explicou o mundo pra mim”
(Nando Reis)

Agradecimentos

Aos meus pais, Luciana e Péricles, meus maiores exemplos e incentivadores. Agradeço por sempre acreditarem na minha capacidade, por me estimularem a ir cada vez mais longe e por oferecerem todo o suporte necessário para que eu pudesse me dedicar aos estudos e seguir na vida acadêmica. Mesmo distantes fisicamente, sempre estiveram presentes. Obrigada por serem meu porto seguro e os meus melhores amigos.

À minha irmã Helena, que sempre foi minha parceira e amiga, tornando todo este processo mais leve com nossas conversas diárias e com todo o amor transmitido, tanto à distância quanto nos momentos de retorno para casa. Ao meu irmão Hermes, meu companheiro de jornada na vida acadêmica e exemplo de dedicação. Meu parceiro de vida em São Carlos, juntamente com minha cunhada Natália. Minha imensa gratidão a vocês por serem e continuarem sendo minha base familiar em São Carlos.

Ao meu noivo, Thiago, por ser o melhor companheiro de vida, por me apoiar em cada decisão, seja ela pequena ou grandiosa, por compartilhar comigo momentos especiais e por estar ao meu lado em todos os momentos de dificuldade. Agradeço por todo o amor e pela família que estamos construindo juntos.

Ao meu filho de quatro patas Rogerinho, que trouxe muito amor para mim e pro Thiago pelos 3 meses que passamos juntos. Obrigada por ser nosso filhote lindo, por ter sido o cachorro mais amoroso e companheiro, mamãe te ama e sente muita saudade.

Ao meu orientador, Daniel Souza Corrêa, por todo o incentivo, atenção e dedicação, pelas inúmeras oportunidades e pela confiança no meu trabalho. Agradeço também por todos os ensinamentos, sempre transmitidos com muita paciência. Sua orientação foi essencial para o meu desenvolvimento como profissional, e você se tornou um grande exemplo para mim na área. Obrigada por me guiar e por oferecer todo o suporte necessário ao longo do desenvolvimento do meu projeto de doutorado.

À minha amiga e parceira de laboratório Tamires, que foi meu primeiro contato em São Carlos. Obrigada pelos vários momentos de alegria compartilhados, dentro e fora do laboratório. Ao meu amigo Francisco, que foi um super parceiro de trabalho, e

além de tudo um grande amigo. Obrigada por todo incentivo e por embarcar comigo em diversos projetos, me fazendo acreditar no meu potencial como pesquisadora.

Aos demais colegas de laboratório e ex-membros do grupo, Luis, Rafaela Machado, Rodrigo, Rafaela André, Augusto, Kelcilene, Murilo, Patrícia, Mirela, Douglas, Jakeline e Luiza, pela ajuda e pelo auxílio nas ideias do projeto, e pelos momentos de descontração durante nossas conversas

À Embrapa Instrumentação, pela infraestrutura oferecida e pelo apoio de todos os profissionais dos diferentes setores, que sempre estiveram à disposição. Um agradecimento especial a Adriana, Ana, Paulinho, Viviane e Alice.

À Universidade Federal de Sâo Carlos (UFSCar) pela oportunidade de desenvolver meu projeto de doutorado, aos professores da Pós-Graduação em Química que contribuíram para a minha formação, e aos funcionários do departamento.

O presente trabalho foi realizado com apoio da Coordenação de Aperfeiçoamento de Pessoal de Nível Superior - Brasil (CAPES) - Código de Financiamento 001. Além do financiamento do projeto de doutorado 607122/2021-00, também forneceu apoio financeiro para a participação em congressos.

Às minhas amigas de infância, que escolhi para sempre como minhas irmãs, Suelen, Karen e Miclaine. Agradeço por sempre se fazerem presentes em minha vida, por me apoiarem e por serem minhas parceiras há tanto tempo.

LIST OF TABLES

LIST OF FIGURES

LIST OF SCHEMES

RESUMO

IMPRESSÃO 3D DE AEROGEIS E FIBRAS FIADAS POR SOPRO DE SOLUÇÃO, MODIFICADAS COM ESTRUTURAS METAL-ORGÂNICAS/ DISSULFETO DE MOLIBDÊNIO PARA ADSORÇÃO E FOTODEGRADAÇÃO DE CONTAMINANTES AMBIENTAIS. A remoção de contaminantes orgânicos em sistemas aquosos, como os corantes sintéticos, representa um desafio significativo devido à limitada eficiência dos métodos convencionais usualmente empregados. A presença de corantes no ambiente pode causar diversos impactos negativos, uma vez que esses compostos frequentemente apresentam toxicidade e persistência. Nesse contexto, torna-se imprescindível o desenvolvimento de novos métodos e materiais eficientes que sejam capazes de remover e degradar esses contaminantes. Neste trabalho, sintetizamos um material à base do MOF (*metal-organic framework*) MIL-88A e MoS_2 com o objetivo de desenvolver um fotocatalisador eficiente para a remoção de contaminantes ambientais. Testes de fotodegradação utilizando o corante azul de metileno (MB) como modelo, com o material na forma de pó, demonstraram uma eficiência superior a 90 % em 120 min. Para facilitar o processo de reutilização e minimizar a aglomeração dos fotocatalisadores em solução, o MOF/MoS_2 foi imobilizado em duas plataformas distintas: i) aerogéis fabricados por impressão 3D e ii) fibras de polivinilpirrolidona (PVP)/SiO_2 produzidas pela técnica de fiação por sopro em solução (SBS). Os aerogéis fabricados por impressão 3D foram produzidos a partir de gelatina, carboximetilcelulose e alginato, incorporando 5 % e 7.5 % em massa do MOF/MoS_2, sendo denominados como HD (sem MOF/MoS_2), HD/MOF/MoS_2 5 % e HD/MOF/MoS_2 7.5 %. Testes de adsorção dos aerogeis mostraram eficiências de 16.77 %, 28.66 % e 95.86 %, respectivamente. Nos testes de fotodegradação, todos os aerogéis apresentaram eficiências superiores a 80 %. Já as fibras de PVP/SiO_2 produzidas pela técnica de SBS foram submetidas a um tratamento térmico para remoção parcial da porção polimérica, e posterior incorporação do MOF/MoS_2. Nos testes de remoção de MB utilizando fibras PVP/SiO_2/MOF/MoS_2, observou-se uma eficiência superior a 90 % em 48 h. Além disso, verificou-se que as fibras de PVP/SiO_2 também contribuíram para os processos de adsorção e fotodegradação, sugerindo um efeito sinérgico. Finalmente, a plataforma PVP/SiO_2/MOF/MoS_2 demonstrou versatilidade na remoção de outros corantes e para o antibiótico tetraciclina. Dessa forma, os resultados obtidos para ambas as plataformas, indicam potencial para auxiliar na mitigação de contaminantes ambientais.

ABSTRACT

3D-PRINTED AEROGELS AND SOLUTION-BLOW SPUN FIBERS MODIFIED WITH METAL-ORGANIC FRAMEWORK/MOLYBDENUM DISULFIDE FOR ADSORPTION AND PHOTODEGRADATION OF ENVIRONMENTAL CONTAMINANTS. The removal of organic contaminants from aqueous systems, such as synthetic dyes, poses a significant challenge due to the limited efficiency of conventional methods typically employed. The presence of dyes in the environment can lead to various negative impacts, as these compounds often exhibit toxicity and persistence. In this context, the development of novel and efficient methods and materials capable of not only removing but also degrading such contaminants is imperative. In this work, a material based on MOF (metal-organic framework) MIL-88A and MoS_2 was synthesized to develop an efficient photocatalyst for environmental contaminant removal. Photodegradation tests using methylene blue (MB) as a model dye, with the material in powder form, demonstrated an efficiency exceeding 90 % within 120 min. To facilitate reuse and minimize photocatalyst aggregation in solution, the MOF/MoS_2 was immobilized onto two distinct platforms: I) aerogels fabricated via 3D printing and ii) polyvinylpyrrolidone (PVP)/SiO_2 fibers produced by solution blow spinning (SBS). The 3D-printed aerogels were fabricated using gelatin, carboxymethylcellulose, and alginate, incorporating 5 % and 7.5 % by weight of MOF/MoS_2, and were designated as HD (without MOF/MoS_2), HD/MOF/MoS_2 5 %, and HD/MOF/MoS_2 7.5 %. Adsorption tests showed efficiencies of 16.77 %, 28.66 %, and 95.86 %, respectively. In photodegradation experiments, all aerogels achieved efficiencies exceeding 80 %. The PVP/SiO_2 fibers produced by SBS underwent thermal treatment to for partial removal of the polymeric portion before incorporating MOF/MoS_2. In MB removal tests using PVP/SiO_2/MOF/MoS_2 fibers, efficiencies greater than 90 % were observed within 48 h. Additionally, the PVP/SiO_2 fibers contributed to both adsorption and photodegradation processes, suggesting a synergistic effect. Finally, the PVP/SiO_2/MOF/MoS_2 platform demonstrated versatility in removal other dyes and the antibiotic tetracycline. Thus, the results obtained for both platforms indicate their potential for mitigating environmental contaminants.

Summary

1. INTRODUCTION

The increasing contamination of water resources has become a global concern, driven by various factors, such as population growth and rapid industrial development.[1] Dyes are a notable example of pollutants widely released into the environment without prior treatment. Industries such as paper, rubber, plastics, food processing, and especially textiles, are large consumers of dyes, with approximately 100,000 commercial dyes in use.[1,2] The annual production of dyes is estimated to reach 700,000 tons, with around 15 % released into the environment without treatment.[2] In additional to environmental impacts, dyes are classified as toxic, mutagenic, and potentially carcinogenic substances, posing threats to human health and biodiversity.[3] Among the various types of dyes, methylene blue stands out as one of the most widely used. It is a synthetic cationic dye with a heterocyclic aromatic chemical structure.[2,4]

To reduce the presence of these contaminants, several methods have been developed, which can be grouped into three main categories: physical methods, including filtration membranes[5] and adsorption[6,7]; chemical methods, encompassing coagulation[8] or flocculation[9,10] combined with flotation and filtration[11], as well as advanced oxidation processes[12]; and biological methods, such as aerobic and anaerobic microbial degradation[13,14] and enzyme[15] application.[16] Among these methods, advanced oxidation processes, particularly photocatalysis, have emerged as highly effective. Key advantages of photocatalysis include its ability to convert contaminants into simple, non-toxic molecules and the potential use of sunlight as an energy source for this conversion, making the process more sustainable.[16,17]

Materials commonly used in photocatalytic processes include semiconductors like TiO_2, ZnO, SnO_2, WO_3, e Fe_2O_3, among others. However, these semiconductors have inherent limitations that can hinder photocatalytic efficiency.[18] The main limitations include their absorption range, often restricted to the UV region, and the rapid recombination of electron-hole (e^-/h^+) pairs, which results in low catalytic efficiency and limited redox capacity.[19]

Modification strategies for these semiconductors, along with the use of alternative materials, have been recently explored to enhance photocatalytic performance. In this context, the present work investigated the use of metal-organic frameworks (MOFs) as photocatalysts for pollutant degradation. Additionally,

heterojunctions were formed between the MOF and MoS_2 to optimize photocatalytic efficiency further. Another strategy explored in this study was the immobilization and incorporation of the photocatalysts onto materials with high surface area, aimed at facilitating their recovery and reuse. To this end, the photocatalysts were immobilized onto two different substrates: i) composite PVP/SiO_2 fibers produced by solution blow spinning and ii) 3D printed polymeric aerogels, providing an efficient platform for practical application in environmental remediation.

1.1 DYES

Dyes are colored, highly soluble chemical compounds widely used across various industrial sectors. These compounds can be classified into two main categories: natural and synthetic. Natural dyes are derived from biological sources, such as animals, plants, fruits, and minerals, and are known for their low toxicity.[3] In contrast, synthetic dyes are chemically synthesized, offering a wide range of available colors and being more cost-effective than natural dyes. However, synthetic dyes can exhibit high toxicity, posing a significant environmental risk.[1,16]

Dye molecules are structurally complex and consist of two primary components: chromophores, responsible for coloration and often acting as electron acceptors, and auxochromes, which typically act as electron donors, conferring affinity to the dyed substrate.[1,3] Within the class of synthetic dyes, these compounds can be further subdivided based on their application (such as acidic, basic, reactive, and direct dyes) or according to the chromophore group present, such as nitro, azo, nitroso, among others.[20]

Methylene blue (MB) is a widely used example of a synthetic dye, with the molecular formula $C_{16}H_{18}N_3SCl$ (MW 319.85 g/mol). This dye is classified as cationic, basic, and direct, as it can be applied directly to the material to be dyed by immersion.[2] Table 1.1 presents data on MB toxicity in relation to exposure doses.[4]

Table 1.1 Toxicity of MB doses from various human studies.[4]

Toxic doses (mg/kg)	Symptoms/Manifestation
2-5	Hemolytic anemia, fever, methemoglobinemia, nausea, vomiting, chest pain, dyspnea, hypertension.
>5	Fatal serotonin toxicity.
20-80	Refractory hypotension, reduced renal blood flow, fainting, and skin discoloration.

The methylene blue molecule has a structurally complex and chemically stable conformation, containing nitrogen functional groups, aromatic rings, and conjugated double bonds. These characteristics make it difficult to decompose by simple photolysis, necessitating the use of advanced systems for efficient removal, such as photocatalytic processes.[4]

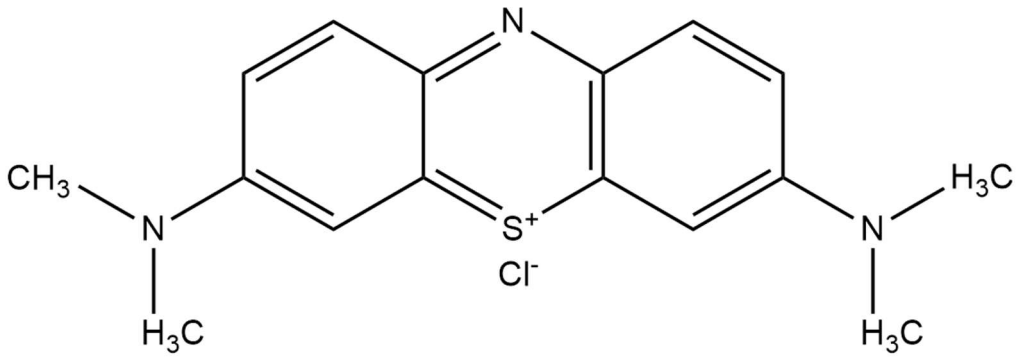

Figure 1.1. Structure of methylene blue. (Author image)

1.2 PHOTOCATALYTIC PROCESS

Advanced oxidation processes (AOPs) encompass effective treatments for the removal of organic and inorganic contaminants through reactions involving oxidizing species, including hydroxyl radicals (•OH) and other reactive oxygen species (ROS), such as superoxide radicals ($^{\bullet}O_2^-$).[21] AOPs can occur in homogeneous or heterogeneous systems, with the latter involving the addition of photocatalysts to the reaction medium. The IUPAC defines a photocatalyst as a "catalyst capable of absorbing light and promoting chemical transformations of the reaction partners".[22]

One of the primary advantages of photocatalytic processes over traditional treatments is their ability to degrade environmentally persistent compounds, resulting

in less toxic products, thereby making photocatalysis a sustainable and eco-friendly technology.[1] In heterogeneous photocatalysis, photocatalysts work by converting light energy (UV, visible, or solar) into chemical energy, promoting oxidation and reduction reactions that lead to the total or partial mineralization of contaminants.[23] The mechanism involved in heterogeneous photocatalysis include some steps: (1) adsorption of contaminants onto the catalyst surface; (2) light absorption, enabling the formation of electron-hole pairs (e^-/h^+); (3) charge carrier transfer to the catalyst surface; and (4) reactions of charge carriers and radicals with contaminants, producing less toxic byproducts.[24] The equations representing the above stages are described as follows:

$$\text{Photocatalyst} + (E_g \leq h\nu) \rightarrow h^+ (BV) + e^- (BC) \quad (1)$$

$$H_2O + h^+ \rightarrow H^+ + {}^\bullet OH \quad (2)$$

$$OH^- + h^+ \rightarrow {}^\bullet OH \quad (3)$$

$$O_2 + e^- \rightarrow {}^\bullet O_2^- \quad (4)$$

$$H_2O + {}^\bullet O_2^- \rightarrow {}^\bullet HO_2 + OH^- \quad (5)$$

$$H_2O_2 + e^- \rightarrow {}^\bullet OH + OH^- \quad (6)$$

$$e^- + h^+ + {}^\bullet OH + \text{contaminants} \rightarrow \text{byproducts} + CO_2 + H_2O \quad (7)$$

The generation of charge carriers (e^-/h^+) occurs when electrons are promoted from the valence band (VB) to the conduction band (CB) after light irradiation. These charge carriers can react with H_2O and O_2 molecules to form radicals that promote contaminant degradation (Figure 1.1). Additionally, e^-/h^+ pairs can directly contribute to degradation through oxidation and reduction reactions.[23,25] However, several factors can affect photocatalytic efficiency, including catalyst morphology, light source intensity, band gap, and charge carrier stability.[25]

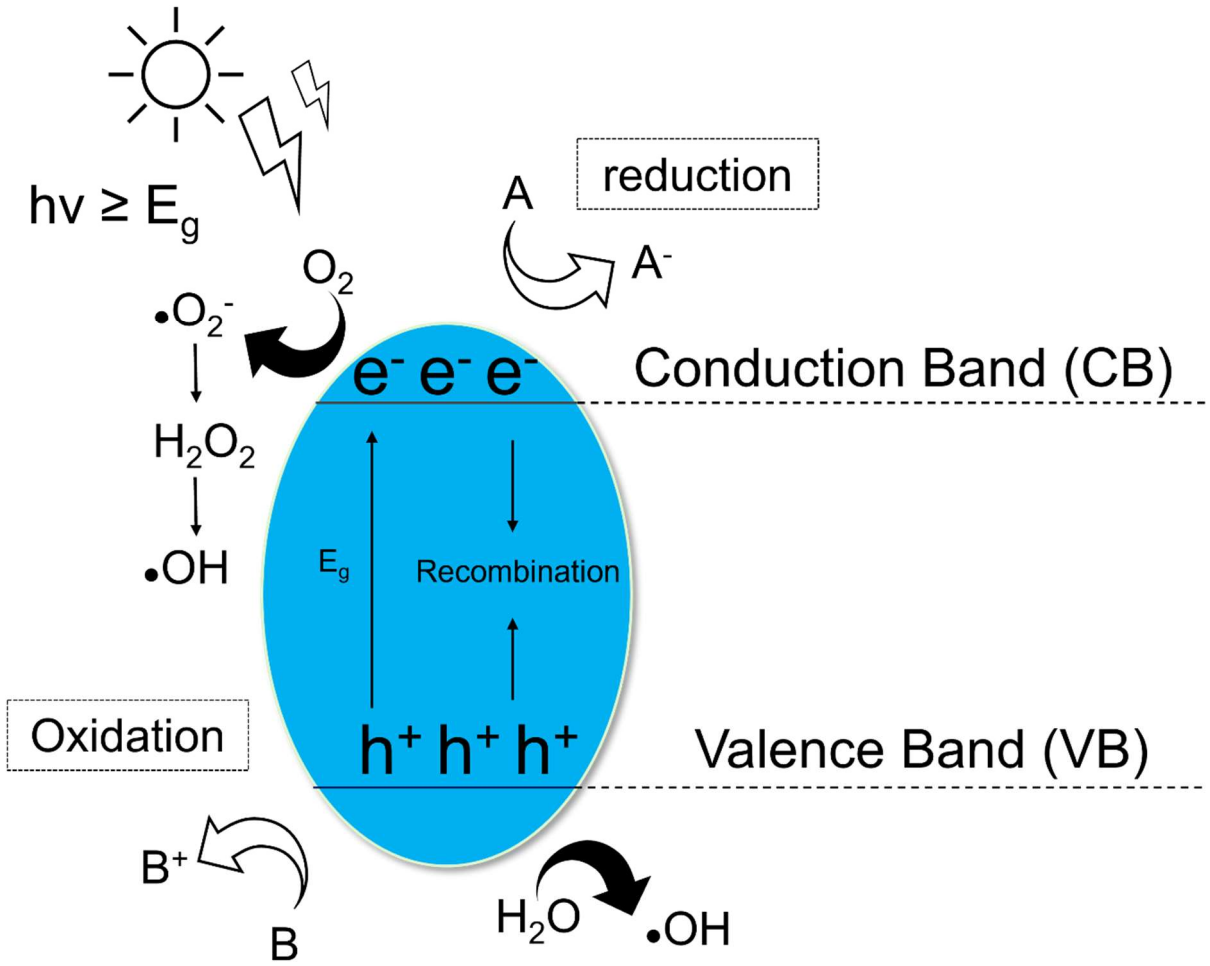

Figure 1.2. Photodegradation mechanism for heterogeneous catalysis. (Author image)

Catalyst morphology directly influences photocatalytic efficiency. Generally, it is assumed that a higher surface area can provide more active sites for interactions with contaminant molecules, making nanocatalysts potentially more effective than larger catalysts. However, semiconductor morphology also impacts properties such as band gap width and crystallinity, which directly affect the separation of photogenerated charges and, consequently, catalytic efficiency. Thus, semiconductors with high surface area and reduced dimensions may paradoxically exhibit low catalytic efficiency if they have low crystallinity or a high band gap.[26,27]

Additionally, the intensity of incident light directly influences the number of photons available to interact with the catalyst. Higher light intensity provides a greater number of photons, resulting in an increase in energy available to promote charge carrier generation.[28–30] The material's band gap is another critical factor, as it determines the wavelengths at which electron-hole pairs (e^-/h^+) can be generated. For this to occur, the band gap must be equal to or less than the energy of the incident

light, allowing electrons to be excited from the valence band (VB) to the conduction band (CB). Catalysts with high band gap values require more energy to activate these transitions, limiting the use of visible light. Therefore, one primary objective in photocatalysis is to develop materials with reduced band gaps, allowing more efficient use of visible light.[31] Finally, the stability of e^-/h^+ pairs is crucial for efficient degradation reactions. The rapid recombination of these charge carriers compromises the photocatalytic process, rendering it inefficient.[32]

The main reactive species involved in the photocatalytic process are h^+, e^-, and $^\bullet OH$. However, other species, such as superoxide radicals ($^\bullet O_2^-$), can also actively participate in the reactions. To assess the influence of each reactive species during the degradation process and to determine the reaction mechanism, specific chemical compounds known as scavengers are added to the solution containing the contaminant and the photocatalyst. These scavengers selectively inhibit the action of reactive species. By comparing degradation rates, the relative influence of each species on the process can be inferred.[33]

The most used scavengers to inhibit $^\bullet OH$ radicals include alcohols such as tert-butyl alcohol, isopropyl alcohol, or methanol. For $^\bullet O_2^-$ radicals, compounds like benzoquinone, ascorbic acid, and acrylamide are frequently employed. Ammonium oxalate and ethylenediaminetetraacetic acid (EDTA) are used for h^+ inhibition, while benzoic acid, silver nitrate, potassium dichromate, and hydrogen peroxide are utilized for e^- inhibition.[33]

Among the wide variety of available semiconductors, TiO_2 remains as the most extensively studied in the field of photocatalysis. Its photocatalytic properties were first described by Fujishima and Honda in 1972, who reported the photochemical splitting of water into hydrogen and oxygen in the presence of TiO_2.[34] This breakthrough inspired numerous subsequent studies, establishing TiO_2 as a benchmark material due to its high chemical stability, low cost, low toxicity, and high efficiency in pollutant degradation.[35,36] Other metal oxides, such as ZnO, SnO_2, WO_3, and Fe_2O_3, have also been explored for photocatalytic applications.[1]

Despite the various advantages associated with the application of metal oxides like TiO_2, there are limitations that hinder their performance. Key limitations include low solar light conversion efficiency, susceptibility to photochemical corrosion, rapid

particle agglomeration, and fast recombination of e^-/h^+ pairs. These factors drive the development of new materials and strategies to mitigate these drawbacks. [37,38] In this context, metal-organic frameworks (MOFs) have emerged as promising alternatives.

1.3 METAL-ORGANIC FRAMEWORKS (MOFs)

Metal-organic frameworks (MOFs), also known as porous coordination polymers (PCPs), are crystalline compounds consisting of metal ions or clusters connected by organic linkers, forming continuous three-dimensional networks.[39] The first MOF was reported in 1989 by Robson and collaborators,[40,41] but the term "MOF" only officially entered the literature in 1995.[42] Since then, a large number of different MOFs has been synthesized, often named based on the discovery location, followed by a number indicating chronological order, such as MIL-n (Matérial de Institut Lavoisier), HKUST-n (Hong Kong University of Science and Technology), and UiO-n (University of Oslo).[43]

Building MOFs from organic and inorganic components allows for a wide variety of geometries, providing diverse functionalities. Beyond structural variability, the bonds between the linkers and appropriate metals enable the formation of pores with different sizes and shapes.[44,45] One of the main advantages of MOFs is the robustness of the metal-ligand connections, which are strong enough to ensure structural stability and result in permanent porosity.[46] Additionally, for photocatalytic applications, MOFs have the advantage of being able to absorb visible light.[47] Figure 1.2 illustrates some MOFs and their absorption wavelengths, considering their band-gap values.

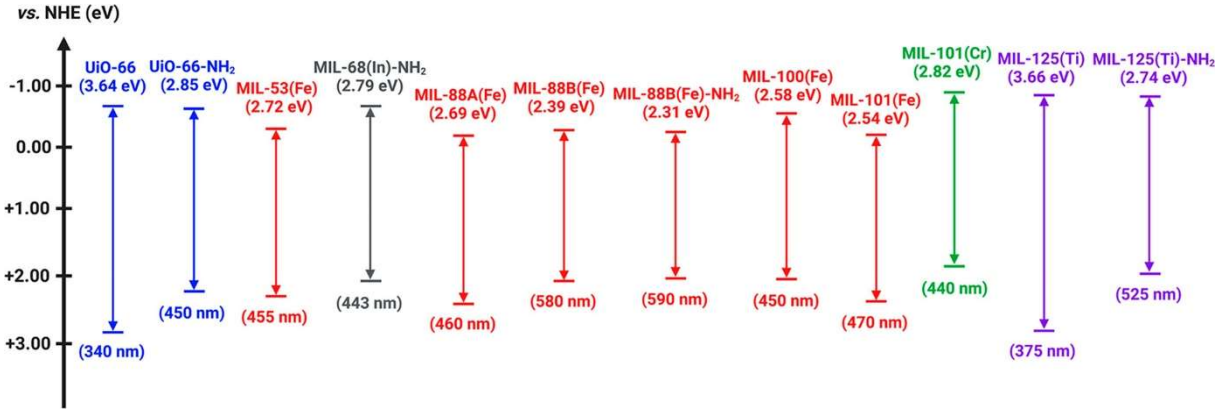

Figure 1.3. Band-gap energies and absorption wavelengths for some MOFs. Reprinted with permission from Wen et al [48] Copyright 2021, American Chemical Society.

Among various types of MOFs, those with iron (Fe) metal centers (Fe-MOFs) are notable for catalytic applications due to their abundance and environmental compatibility.[49] As photocatalysts, Fe-MOFs present two types of mechanisms: the generation of holes and electrons from the photoexcitation of Fe-O clusters and ligand-to-metal charge transfer (LMCT), where the organic linkers act as antennas to absorb light and subsequently generate electrons.[50,51] The generated electrons are transferred to the cluster surfaces, as shown in Figure 1.3. In addition to these mechanisms, there are ligand-to-ligand, metal-to-ligand, and metal-to-metal-to-ligand charge transfer mechanisms.[50]

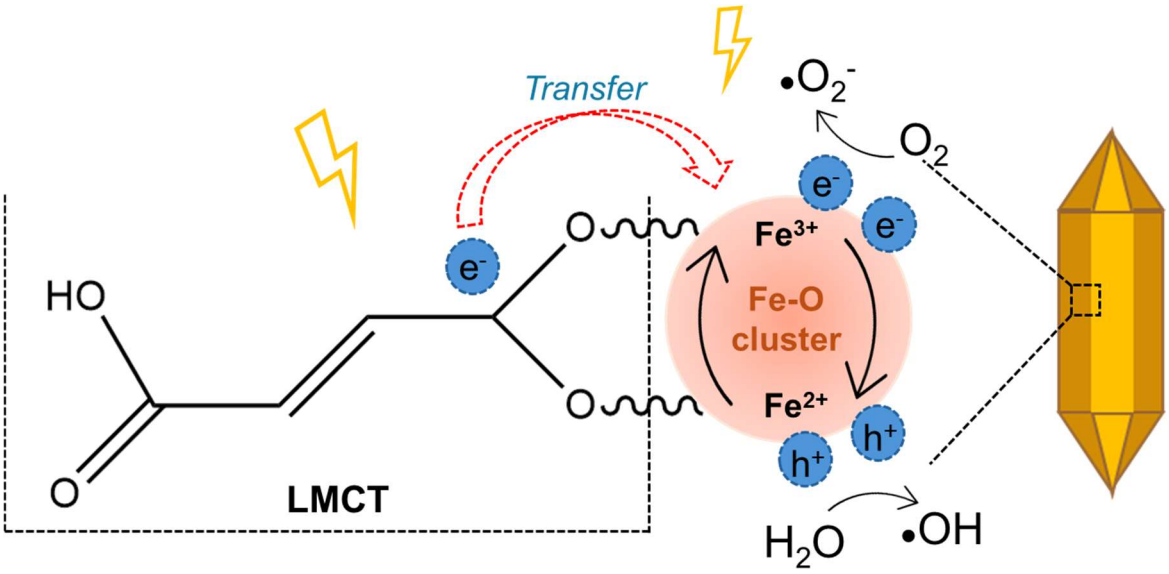

Figure 1.4. Photocatalysis mechanism for MIL-88A MOFs. (Author image).

Another important feature of Fe-MOFs is their ability to perform redox reactions in the presence of auxiliary oxidants, such as H_2O_2, in processes called photo-Fenton.[52] In these reactions, H_2O_2 interacts with Fe-O clusters in the MOF, resulting in $^{\bullet}OH$ radicals (Eqs. 8 and 9) that significantly contribute to contaminant degradation. Moreover, under light irradiation, H_2O_2 can capture photogenerated e^-, promoting additional $^{\bullet}OH$ radical formation and delaying e^-/h^+ recombination (Eqs. 10 and 11).[53]

$$Fe^{3+} + H_2O_2 \rightarrow Fe^{2+} + {}^{\bullet}HOO + H^+ \quad (8)$$

$$Fe^{2+} + H_2O_2 \rightarrow Fe^{3+} + {}^{\bullet}HO + OH^- \quad (9)$$

$$Fe\text{-}MOF + hv \rightarrow h^+ + e^- \quad (10)$$

$$e^- + H_2O_2 \rightarrow {}^{\bullet}HO + OH^- \quad (11)$$

The chemical stability of MOFs in aqueous systems is also critical for their applications in heterogeneous photocatalysis. As previously mentioned, the interaction strength between the metal center and the organic ligand is key to the structural stability of MOFs. According to the HSAB (hard/soft acid-base) theory, more stable complexes are formed by combining hard acids and bases or soft acids and bases. For instance, Fe^{3+} ions are hard Lewis's acids that form stable complexes with carboxylic ligands, as in fumaric acid, used in MOFs like MIL-88A.[54] Other metal centers capable of forming stable structures with carboxylate ligands include Ti^{4+}, Zr^{4+}, Al^{3+}, and Cr^{3+} (Figure 1.4).[55]

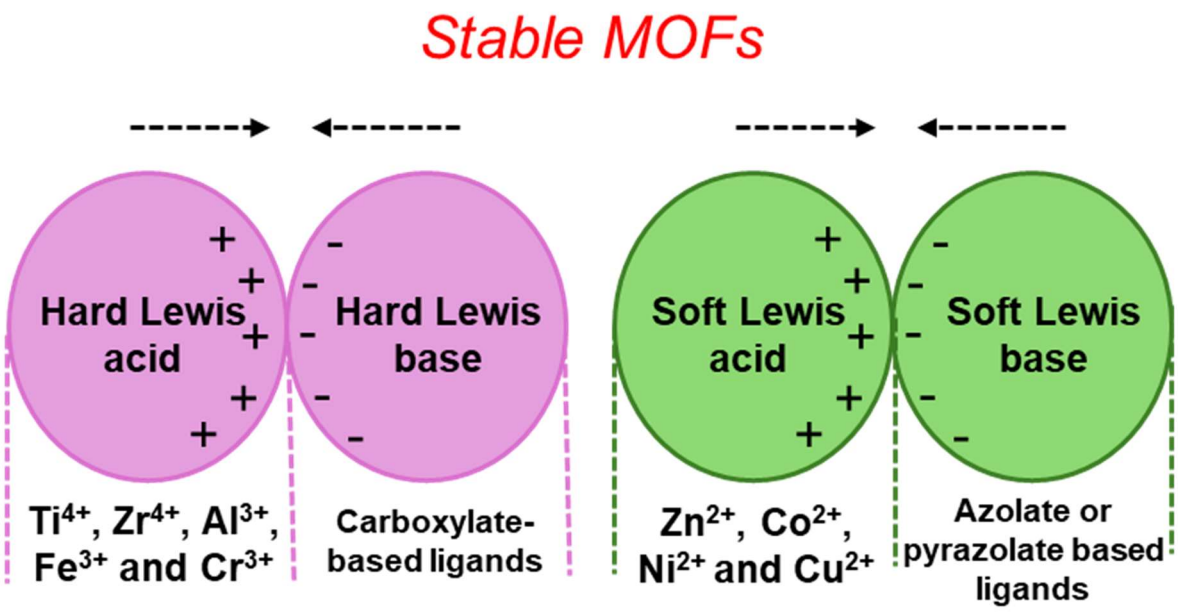

Figure 1.5. Method of obtaining MOFs according to HSAB theory. (Author image).

However, under adverse conditions, such as pH variations, ligand displacement may occur, resulting in MOF structure collapse. For MIL-88A, studied in this work, its stability in basic media is significantly lower than in neutral or acidic media. In basic conditions, MIL-88A undergoes structural breakdown due to the cleavage of iron-fumarate bonds, where fumarate is displaced due to the high affinity between Fe^{3+} ions and OH^-, as OH^- ions are hard bases.[56]

The instability of MOFs in acidic solutions is partially related to the pKa of their ligands, as ligands with high pKa values exhibit greater proton affinity. When the solution pH is lower than the ligand's pKa, H^+ ions compete with metal ions for ligand coordination, leading to MOF degradation.[55]

Another important factor is the stability of organic ligands in the presence of oxidants generated during photocatalysis. Ligands with electron-withdrawing groups, such as carboxylates, halogens, and nitro groups, have lower electron density, making them less susceptible to oxidation. In contrast, ligands with electron-donating groups, such as amines, hydroxyls, alkoxides, and alkyl groups, possess electron-rich regions, making them more vulnerable to oxidation reactions.[48,57]

Despite the numerous advantages attributed to MOFs, the rapid recombination of e^-/h^+ pairs remains a challenge. Various strategies have been developed to address this issue, including doping and modification of MOFs, introduction of defects, and the construction of heterojunctions.[37] Among these approaches, heterojunction construction is the most promising due to its unique advantages, such as the formation of distinct band structures that significantly enhance photocatalytic efficiency.[58]

1.4 MOLYBDENUM DISULFIDE (MoS_2)

In this study, molybdenum disulfide (MoS_2), an n-type semiconductor, was selected to form a heterojunction with the MOF MIL-88A. MoS_2 belongs to the class of transition metal dichalcogenides (TMDCs) and exhibits a two-dimensional (2D) layered structure.[59] It has been extensively investigated for photocatalytic applications due to its high specific surface area, excellent optical absorption capacity, and high charge carrier mobility. However, when used as an individual photocatalyst, the rapid recombination of electron-hole (e^-/h^+) pairs compromises its photocatalytic efficiency, similar to what is observed in other semiconductors.[60,61]

MoS_2 has a layered structure similar to graphene, where the interactions between layers occur predominantly through van der Waals forces. This characteristic allows the modulation of the bandgap depending on the number of layers, with a tendency to increase as the material thickness decreases. Additionally, it has been observed that during the transition from multilayer to monolayer, MoS_2 undergoes a change in its bandgap nature, shifting from an indirect to a direct transition.[59,60]

Layered MoS_2 can exhibit three types of crystalline structures, which vary according to the stacking arrangement and the coordination between Mo and S atoms. These structures are classified as follows: 2H, when molybdenum atoms adopt a trigonal prismatic coordination; 1T, when the coordination is octahedral; and 3R, when

the coordination forms a hexagonal arrangement. Among these, the 2H phase is the most stable under standard conditions, while the 1T and 3R phases are metastable and can be easily converted into the 2H phase under appropriate conditions.[59]

In the context of photocatalysis, low-dimensional MoS_2 is considered more promising due to its enhanced response to visible light.[61]

1.5 HETEROJUNCTION

The construction of heterojunctions involves the combination of two distinct semiconductors, which can interact in three primary configurations, known as: 1) broken gap; 2) straddling gap; and 3) staggered gap (Figure 1.5).[62]

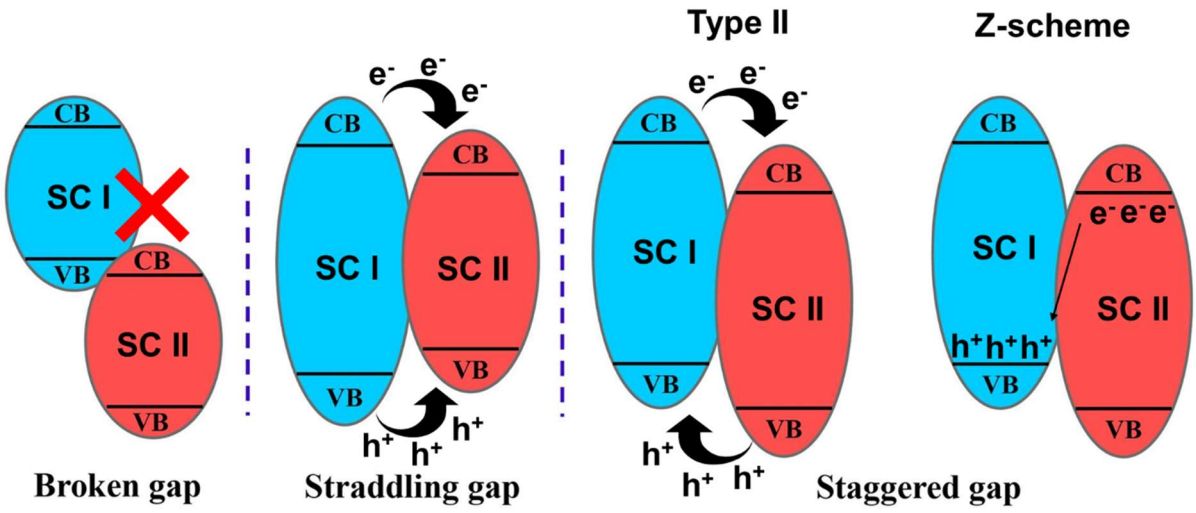

Figure 1.6. Heterojunction types. (Adapted image) Reprinted with permission from Che et al. [62] Copyright 2023, Elsevier.

In broken gap heterojunctions, there is no overlap between the two semiconductors, resulting in a significant gap between them and inhibiting charge transfer.[58,63]

In a straddling gap heterojunction, the conduction and valence bands of one semiconductor are contained within the bands of the other semiconductor. As illustrated in Figure 1.5, photogenerated electrons and holes in semiconductor I (SC I) migrate to semiconductor II (SC II), which has a smaller band gap. This process results in rapid recombination of charge carriers and consequently reduces redox capacity, as SC II has lower redox potentials.[58,63]

In a staggered gap heterojunction, both the valence and conduction bands of SC I are in regions of more negative potential than the corresponding bands of SC II.[58,63] However, in this configuration, electron and hole transfer can occur in two different ways, classified as type II heterojunction and Z-scheme. In the type II heterojunction, generated holes migrate to the less positive valence band (from SC I to SC II) while electron transfer occurs to the less negative conduction band (from SC II to SC I). Although this type of heterojunction promotes efficient charge separation, its oxidation and reduction capabilities are limited due to charge migration to bands with lower redox potential. On the other hand, in the Z-scheme heterojunction, electrons migrate from the lower CB of SC II to the upper VB of SC I, where they recombine with the holes. This configuration ensures that the valence and conduction bands with higher redox capacity remain available, inhibiting the recombination of h+/e- pairs, and is thus more efficient than the type II heterojunction.[62,64]

The construction of a staggered gap heterojunction can be achieved with either semiconductors of the same nature or with different types, such as the junction between p-type (hole-rich) and n-type (electron-rich) semiconductors. The combination of different semiconductors is considered the most effective due to the presence of an internal electric field that facilitates charge separation.[62]

The junction between two different semiconductors, forming a p-n type heterojunction, can occur in two ways. In the first configuration, the p-type semiconductor, for reduction, has its Fermi level close to the valence band, while the n-type semiconductor, for oxidation, has its Fermi level near the conduction band. Upon contact, electrons migrate from the p-semiconductor to the n-semiconductor until the Fermi levels equalize, resulting in the formation of an internal electric field, as illustrated in Figure 1.6. This electric field can facilitate the separation and transfer of charge carriers, enhancing photocatalytic performance. Upon light irradiation, the charge transfer mechanism may follow type II or Z-scheme.[62,64,65]

Another configuration, shown in Figure 1.6, involves p-type semiconductors for oxidation and n-type for reduction. In this model, electron transfer is more likely to follow the Z-scheme, which is thermodynamically permitted.[62]

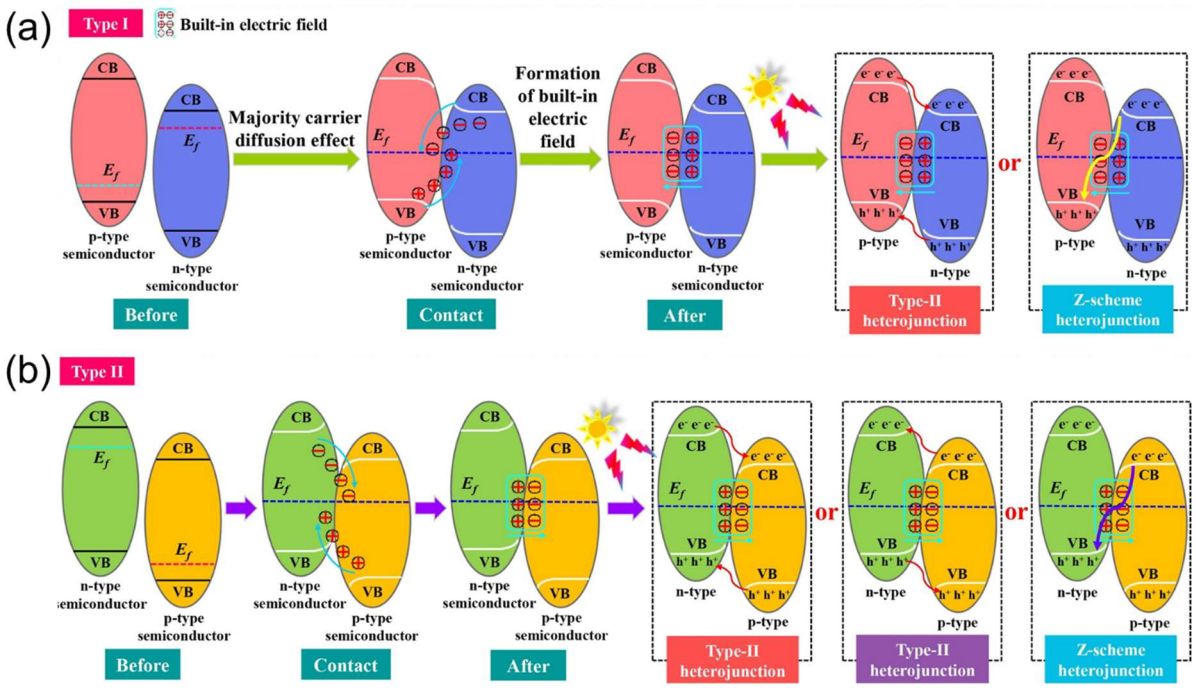

Figure 1.7. Types of charge carrier migration in p-n heterojunctions. Reprinted with permission from Che et al. [62] Copyright 2023, Elsevier.

One possible strategy to determine the charge transfer mechanism in staggered gap heterojunctions (whether it is type II or Z-scheme) is the scavenger method. For this method, it is essential to determine the positions of the conduction and valence bands of the semiconductors involved. If the conduction and valence bands are properly aligned with respect to the redox potentials of $H_2O/^{\bullet}OH$ and $O_2/^{\bullet}O_2^-$, the formation of radicals and, consequently, the type of charge transfer can be predicted. In the configuration illustrated in Figure 1.7, considering that the $^{\bullet}O_2^-$ radical is the main active species during the photocatalytic process, the charge transfer mechanism is characterized as a Z-scheme. In contrast, in the case of a type II heterojunction, electrons would migrate to a conduction band with a reduction potential inadequate for the formation of $^{\bullet}O_2^-$ radicals.[63]

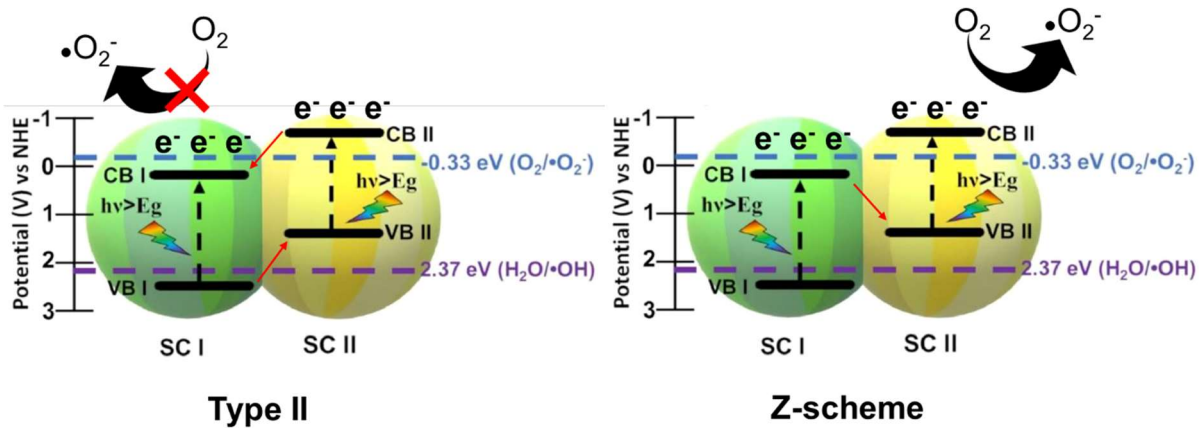

Figure 1.8. Distinction between type II and Z scheme charge transfers. (Image adapted)[63]

Considering the MIL-88A/MoS_2 heterojunction proposed in this work, the MOF MIL-88A can be classified as a p-type semiconductor, as reported in the literature, while MoS_2 is recognized as an n-type semiconductor. Thus, the combination of these materials results in a p-n type heterojunction.[66,67]

A challenge in using photocatalysts is their recovery and separation from aqueous media to enable their reuse.[68] Recycling the material not only provides economic benefits but also positively contributes to environmental sustainability.[69,70] Among the strategies to overcome this limitation, the immobilization of photocatalysts in solid matrices, such as 3D-printed structures and polymeric fibers, stands out as an effective approach.

1.6 IMMOBILIZATION OF PHOTOCATALYSTS

1.6.1 3D printing

3D printing is a widely applied additive manufacturing (AM) technology for fabricating three-dimensional materials, enabling the creation of complex structures without the need for molds. Material geometries are constructed layer-by-layer from cross-sectional slices generated through computer-aided design (CAD) software.[71,72]

One of the 3D printing techniques utilized in AM is direct ink writing (DIW), a versatile extrusion-based method. DIW printers are equipped with a robotic system capable of movement in three dimensions (XYZ) with a precision reaching a few micrometers (1–3 μm). The robot's movements are controlled by software that

translates the predefined 3D design into G-code commands, directing the printing process.[73] This software also allows for adjusting key parameters such as ink flow, print speed, layer thickness, among others.

The DIW method enables the fabrication of structures using various material combinations, including ceramics, metals, polymers, and carbon-based compounds for formulating the printing “ink” or hydrogel.[73,74]

The prepared ink must possess appropriate rheological properties for extrusion, requiring that material concentrations be adjusted so that the hydrogel demonstrates: (1) a predominance of elastic over viscous behavior; (2) structural breakdown and dominance of viscous behavior to ensure flow through the nozzle; and (3) rapid recovery to its original state post-deposition.[75] Thus, rheological studies provide a means to evaluate the printability of these hydrogels through parameters such as viscosity and viscoelasticity. When a liquid is forced to flow, resistance due to cohesive forces among molecules is observed, with viscosity being the measure used to evaluate the liquid's resistance to shear deformation. Consequently, hydrogels can be classified as either Newtonian or non-Newtonian fluids. Newtonian fluids exhibit constant viscosity with increasing shear stress.[76] Printable hydrogels, however, are categorized as non-Newtonian fluids, meaning their viscosity depends on the applied shear rate, and they may be further classified as shear-thinning (pseudoplastic) or shear-thickening (dilatant) fluids. According to Figure 1.8, materials displaying shear-thinning behavior show a decrease in viscosity with increasing shear rate, facilitating hydrogel flow during the printing process.[77]

In addition to viscosity, viscoelasticity is also a crucial parameter in 3D printing. To evaluate viscoelasticity, the storage modulus (G’), representing the gel's elastic behavior; the loss modulus (G”), representing its viscous behavior; and the linear viscosity region (LVR) are considered.[74] For instance, polymeric hydrogels exhibit a linear plateau (LVR) at low shear rates, indicating that the hydrogel will not flow during extrusion until a critical point is reached (G’ = G”), and the critical stress is exceeded (G” > G’), at which the hydrogel primarily behaves as a liquid.[77]

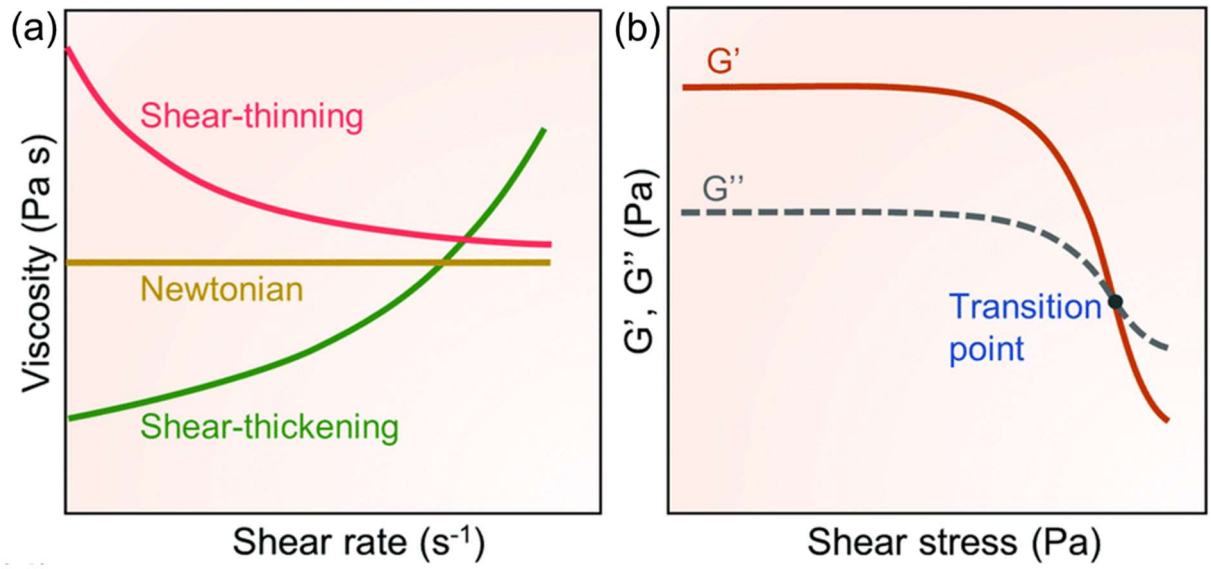

Figure 1.9. (a) Viscosity as a function of shear stress for Newtonian and non-Newtonian fluids and (b) moduli of G' and G" as a function of shear rate (Adapted image).[76]

Another important phenomenon observed for non-Newtonian fluids is thixotropy. Thixotropy can be defined as the reduction in viscosity with time as a shear rate is applied to a sample, followed by the recovery of viscosity when the flow is stopped. Thus, thixotropy allows the assessment of the sample's viscosity at three distinct stages: before, during, and after the application of the shear rate.[78] This behavior enables the evaluation of how much of the initial viscosity can be recovered, that is, the fluid's ability to return to its original state, as well as the time required for this recovery.[75,78]

Hydrogels are generally defined as highly hydrated, crosslinked three-dimensional (3D) networks.[79] The presence of hydrophilic groups, such as carboxyl (-COOH), amide ($-CONH_2$), amine ($-NH_2$), and hydroxyl (-OH) groups, endows hydrogels with a high capacity to absorb large amounts of water into their pores or interstitial spaces.[74,79] Natural polymers like alginate, cellulose, gelatin, and chitosan are widely used for hydrogel synthesis due to their biocompatibility, non-toxicity, and biodegradability. However, filaments printed with single-polymer hydrogels often fail to retain their shape, resulting in spreading and deformation post-printing.[80] Gelatin, for example, is a natural polymer frequently utilized in hydrogel synthesis due to its low cost, abundance, hydrophilicity, biodegradability, and non-toxicity. To enhance

printability and mechanical properties, polymers such as carboxymethylcellulose and sodium alginate are often added.[81,82]

In addition to selecting appropriate hydrogel components, implementing a post-printing crosslinking step is crucial. This process reinforces the structure, increases crosslink density, and improves interactions between the polymer chains. Crosslinking can be achieved by either physical or chemical methods. Among these, a commonly used and straightforward approach involves physical interactions using metal ions.[83,84] Interactions between metal ions (M^{n+}) and polymers are characterized by their high affinity, arising from the interaction between M^{n+} ions, which act as electrophiles, and the more electronegative groups within the polymers, which serve as nucleophiles. When two polymers are present, interactions occur both between the polymer networks and between the polymers and metal ions.[83,84] Various metal ions can be utilized in the crosslinking process, and Figure 1.9 illustrates the crosslinking process of a hydrogel composed of gelatin, sodium alginate, and carboxymethylcellulose with calcium ions (Ca^{2+}).

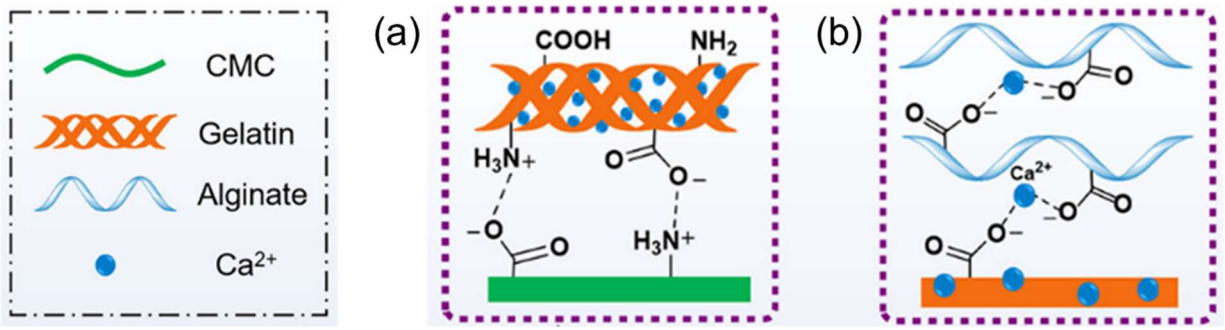

Figure 1.10. Crosslinking promoted by (a) interactions between polymer chains and (b) interactions of the carboxylic groups ($-COO^-$) of the polymers with Ca^+ ions (Adapted image). Reprinted with permission from Zheng et al. [85] Copyright 2020, Elsevier.

For applications in adsorption and catalysis, it is preferable for the hydrogel to be free of liquid, resulting in structures known as aerogels. The term "aerogel" is widely used to describe materials without restrictions on their composition or preparation method, and according to the International Union of Pure and Applied Chemistry (IUPAC), it is defined as a "gel composed of a microporous solid in which the dispersed phase is a gas".[76] However, discrepancies can be found in the literature regarding the definition of a material as an aerogel. Some studies describe aerogels as dried gels

with high porosity greater than 90 %[86], while others define them as structures with porosity greater than 50%.[87]

The most common drying methods for obtaining aerogels include freeze-drying, ambient drying, and supercritical drying. Supercritical drying is widely used to produce aerogels, though it has disadvantages, such as high cost, significant energy consumption, and the risks associated with the extreme temperature and pressure conditions required for the process. Alternatively, ambient drying involves the slow evaporation of the solvent below its boiling point and at atmospheric pressure. However, this method can result in structural collapse due to high capillary pressure and substantial volume shrinkage.[76] In freeze-drying, the hydrogel is initially frozen, followed by a sublimation process of the solvent in a vacuum environment. During the phase transition from liquid to solid, volume changes may occur due to density differences between phases and pore expansion. Despite these variations, freeze-drying is considered a moderately costly technique conducted under relatively mild conditions.[76,88]

Aerogels intended for photocatalytic applications can be modified with nanoparticles, such as metal oxides, metal-organic frameworks (MOFs), or combinations of semiconductor materials. Incorporating semiconductors into porous polymeric matrices can enhance photocatalytic efficiency due to the advantages inherent to this combination. The insertion of nanoparticles reduces the spacing between polymer networks by crosslinking chains with the added materials, resulting in interconnected pores. This modification favors mass and charge transport while increasing the specific surface area, optimizing interaction with the reaction medium.[89]

In certain cases, the metal ions used for polymer crosslinking can also play an active role in photocatalysis, as reported for iron. The interaction of iron with UV light promotes the formation of reactive radicals, which contribute to the catalytic process.[90] Additionally, carboxylate groups present in polymers can enhance catalytic efficiency, as they undergo photooxidation, leading to the generation of additional radicals.[91]

1.6.2 Solution Blow Spinning (SBS)

The production of polymeric fibers has been extensively explored in various research fields due to their advantageous properties, such as flexibility, high surface

area-to-volume ratio, malleability, elasticity, ease of fabrication, and the potential for surface modification to create functional materials.[92]

Fiber production methods include electrospinning, centrifugal spinning, blow spinning, and microfluidic spinning techniques, in which fibers are generated by extruding a polymer solution subjected to different types of external forces. Depending on the method employed, these forces may be electric, centrifugal, or gas flow-based. The extrusion of the polymer generates jets that stretch, forming fibers through a drying process and solvent evaporation.[92,93]

The solution blow spinning (SBS) method has been widely investigated due to its high productivity, simplicity, and versatility. In SBS, polymer jets are formed by gas flow; thus, the system configuration consists of an external nozzle through which gas flows and an internal nozzle for the polymer solution flow, a source of compressed gas (such as air, nitrogen, synthetic air, oxygen, or argon), a collector system for fiber deposition, and an infusion pump that controls the polymer solution flow, as illustrated in Figure 1.10.[92,94] During SBS operation, the polymer solution, forced through the nozzle in a continuous flow, forms a droplet at the nozzle tip. When gas flow is applied to the system, this droplet transforms into a cone, analogous to the Taylor cone observed in electrospinning. When the critical gas pressure is exceeded, the aerodynamic forces overcome the solution's surface tension force, resulting in the formation of a jet from the cone, which is directed to the collector where the formed fibers are deposited.[95]

The adjustable parameters for fiber production include process variables such as solution flow rate, gas pressure, working distance between the nozzle and collector, inner nozzle protrusion relative to the outer nozzle, and nozzle diameter.[94] Additionally, solution parameters, such as solvent type and solution concentration, as well as environmental factors, such as temperature and humidity, also play roles. All these parameters influence the morphology and quality of the produced fibers. High-concentration, high-viscosity solutions tend to produce fibers with larger diameters, while low-volatility solvents or reduced working distances may hinder proper fiber formation, resulting in film formation. Higher pressures generally yield finer fibers, while lower pressures produce larger-diameter fibers. Temperature and humidity also affect the solvent evaporation process and, consequently, fiber formation. However, these

parameters must be adjusted synergistically, as the final fiber quality depends on the interaction of all these factors.[92,95]

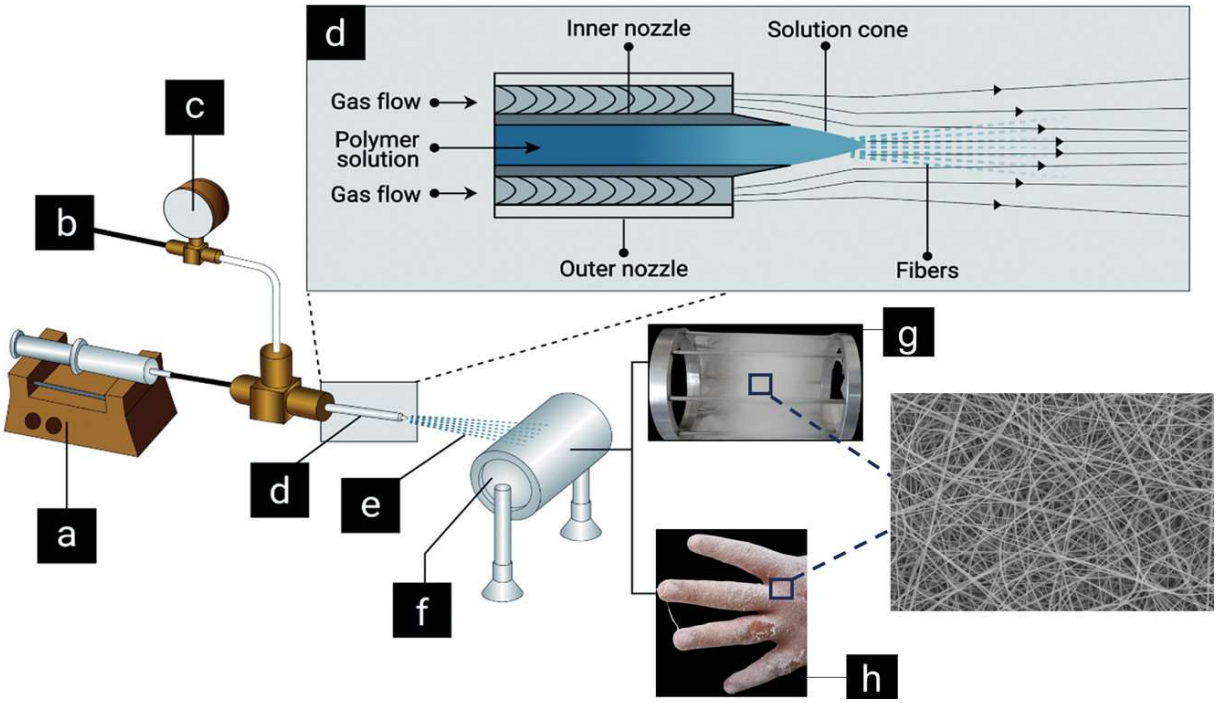

Figure 1.11. Representation of a solution blow spinning (SBS) equipment. (a) Infusion pump; (b) pressurized gas; (c) pressure gauge; (d) nozzle; (e) polymeric nanofibers directed to the collector; (f) collector; (g) fibers deposited on the collector; (h) fibers in situ. Reprinted with permission from dos Santos et al [92] Copyright 2020, American Chemical Society.

In addition to polymeric fibers, inorganic fibers, such as titanium fibers[96], silicon carbide[97], and alumina fibers[98], also have notable advantages, especially in applications such as photocatalysis, batteries, and capacitors, where their structural and chemical characteristics provide superior performance under certain conditions.[99]

For applications in photocatalytic activities, this study focused on fibers composed of SiO_2. An interesting polymer choice for the synthesis of these fibers is polyvinylpyrrolidone (PVP), due to its high solubility, mechanical strength, thermal resistance, and qualities such as biocompatibility, non-toxicity, biodegradability, and pH stability. The SiO_2 precursor is tetraethyl orthosilicate (TEOS), which, when added to PVP, enhances thermal stability.[100]

The preparation of SiO_2 fibers is casing the sol-gel method, which can be performed in solvents such as water, ethanol, or methanol, given the good solubility of

PVP and TEOS in these media, along with the addition of acids to catalyze the polymerization reaction of TEOS.[101,102] Initially, the sol is formed by adding TEOS followed by a strong acid, resulting in a liquid system. This solution is then incorporated into the polymer solution to form a gel, which exhibits higher viscosity. The sol-gel method is based on hydrolysis and condensation reactions. In the sol phase, the hydrolysis of silicon alkoxide (TEOS) in acidic media generates silanol groups that link through condensation reactions, forming a three-dimensional network dispersed within the polymer solution. Polymer aids in fiber formation during the SBS process.[103] Subsequent steps include the thermal treatment of fibers to partially remove the polymer phase.

1.7 STATE OF THE ART

The use of MOFs as photocatalysts has been extensively explored in literature, as well as the formation of heterojunctions between two different materials to enhance and improve photocatalytic processes. Chen et al[104] investigated the efficiency of the heterojunction formed between molybdenum disulfide and zeolitic imidazolate framework structures (MoS_2/ZIF-8) in the photodegradation of the antibiotics ciprofloxacin (CIP) and tetracycline hydrochloride (TC). The results indicated that the proposed heterojunction was effective in separating electron-hole pairs (e^-/h^+), as well as exhibited significant absorption in the visible spectrum. Due to these characteristics, the heterojunction demonstrated superior efficiency in the photodegradation of antibiotics compared to isolated MoS_2, while maintaining stability over reuse cycles.

Li et al[105] proposed the MIL-88A/Bi_2WO_6 heterojunction for the photodegradation of rhodamine B dye and the antibiotic tetracycline. For both contaminants, the heterojunction yielded promising results in processes driven by visible light as the energy source. Comparatively, MIL-88A and Bi_2WO_6 showed degradation efficiencies of 46.5% and 51%, respectively, for tetracycline, while the heterojunction achieved an efficiency of 70.6% in just 80 minutes. In addition to improving catalytic efficiency, the heterojunction exhibited greater stability of the electron-hole pairs (e^-/h^+) compared to the isolated materials. Analyses conducted to determine the photodegradation mechanism and studies of band potentials indicated that the conduction band of the MOF was primarily responsible for forming $\bullet O_2^-$ radicals, which played a crucial role in contaminant degradation.

Zhang et al[106] dispersed aggregated MOFs (ZIF-8) on carbon nitride nanosheets (C_3N_4) within an agar aerogel to create a material that could be easily reused. The C_3N_4 nanosheets played a dual role by controlling the growth of MOF particles and contributing to the photocatalytic process in dye degradation. The modified aerogel was evaluated under visible light irradiation, achieving near-complete dye removal in only 50 minutes and maintaining efficiency for up to five reuse cycles.

Yadav et al[68] immobilized BiOX (Cl, Br, and I) on alumina-based ceramic fibers (Al_2O_3) as a support material to facilitate the separation of photocatalysts from the aqueous medium and mitigate agglomeration issues typical of powdered photocatalysts. In addition to serving as an efficient support, the ceramic fibers provided a high surface area, which can significantly enhance the adsorption process for contaminants[107,108].

Considering the extensive development of industrial activities and the consequent generation of waste, there is a continuous demand for innovative, efficient, and viable methods and materials for pollutant treatment. Therefore, in the present study, a heterojunction between MIL-88A MOF and MoS_2 was developed, subsequently immobilized within suitable substrates to create an effective alternative for the removal of environmental contaminants.

2 OBJECTIVES

The primary objective of this work was to develop a heterojunction between MIL-88A metal-organic frameworks and molybdenum disulfide to obtain an effective material in the adsorption/photodegradation of contaminants. This heterojunction was subsequently incorporated into aerogels produced via 3D printing and also immobilized on the surface of PVP/SiO_2 composite fibers prepared by the solution blow spinning (SBS) method.

2.1 Specific Objectives

- Synthesizing MIL-88A MOF and MoS_2, followed by promoting the MOF/MoS_2 heterojunction;

- Incorporating the MOFs/MoS_2 heterojunction into polymeric hydrogels processed via 3D printing for the subsequent production of functionalized aerogels;

- Immobilizing via spray coating the MOFs/MoS_2 heterojunction on the surface of PVP/SiO_2 composite fibers produced by solution blow spinning;

- Characterizing the obtained materials through thermal analysis, morphological analysis, rheology, porosity, water absorption, photoluminescence, chemical composition, and determination of band gap energy (Eg) and crystalline planes;

- Evaluating the efficiency of the obtained materials in adsorption/photodegradation processes for MB dye.

- Investigating the mechanisms of adsorption and interaction of the dye on the materials, as well as the photodegradation mechanisms;

- Assessing the stability of the materials over reuse cycles.

Overview of Chapters

The results section is divided into two chapters. Chapter 1 contains the article published in Materials Today Chemistry, entitled "**3D-printed MOF/MoS_2 aerogel for dye adsorption and photocatalytic degradation**"[109]. Chapter 2 presents the article in preparation, entitled **"MIL88A/MoS_2 heterojunction supported on PVP/SiO_2 fibers for mitigating environmental pollutants**". Thus, the materials used, methodologies applied, and results obtained are presented within each manuscript.

3 Chapter 1: 3D-printed MOF/MoS_2 aerogel for dye adsorption and photocatalytic degradation

Ana Laura M.M Alves[a,b], Francisco V. dos Santos[a,c], Daniel S. Correa[a,b,c*]

[a]Nanotechnology National Laboratory for Agriculture, Embrapa Instrumentação, 13560-970, São Carlos, SP, Brazil.

[b]PPGQ, Department of Chemistry, Center for Exact Sciences and Technology, Federal University of São Carlos, 13565-905, São Carlos, SP, Brazil

[c]Materials Engineering Department, São Carlos School of Engineering, University of São Paulo, 13563–120 São Carlos, SP, Brazil.

Corresponding author: daniel.correa@embrapa.br

*** Artigo publicado na revista Materials Today Chemistry, 40, (2024), 102248.**

DOI: https://doi.org/10.1016/j.mtchem.2024.102248

Abstract

The escalating challenge of water resources contamination, attributed to toxic pollutants, requires urgent attention from both governments and society. Furthermore, the inefficacy of conventional water treatment methods emphasizes the critical necessity for exploring the development of affordable, renewable, and high-performance materials, which should, for instance, enable the mutual adsorption and photocatalytic degradation of organic pollutants. In the present paper, we used the 3D printing technique to manufacture a novel aerogel based on alginate, gelatin, and carboxymethylcellulose incorporated with 5 and 7.5 wt % of MOF/MoS_2. FTIR spectra and EDS analysis evidenced the presence of MOF/MoS_2 in the structure of the aerogels, while Helium pycnometer analysis and SEM micrographs demonstrated that the aerogels have low density and a porous structure with porosity above 80%. The swelling test showed that the aerogels displayed a high water absorption capacity (1400 %) after 70 h of immersion. The rheology test demonstrated that elastic behavior prevails over viscous behavior (G' > G") and the incorporation of 7.5 wt % MOF/MoS_2 favored shear thinning and viscosity recovery in the hydrogel. Adsorption tests to methylene blue (employed as a model) showed that the aerogel (HD) without the presence of MOF/MoS_2 and the aerogels HD/MOF/MoS_2 5 % and MOF/MoS_2 7.5 % showed removal efficiencies of 16.77 %, 28.66 %, and 95.86 %, respectively. Conversely, the photodegradation test showed that HD/MOF/MoS_2 5 % and HD/MOF/MoS_2 7.5 % had an efficiency of 89 % and HD of 80 %. Therefore, the results demonstrated that the novel aerogels produced are promising candidates for the adsorption and photodegradation of dye while being low-cost, environmentally friendly, and easy to manufacture.

Keywords: 3D printing; natural polymers; aerogel; organic contaminants; photocatalysis.

3.1 Introduction

The accelerated industrial development, characterized by a significant consumption of varied resources, has resulted in the disposal of a considerable amount of persistent organic contaminants, including dyes, pesticides, pharmaceuticals, and aromatic hydrocarbons, into aquatic ecosystems. Particularly, synthetic dyes from the textile industry are pollutants that are difficult to degrade, and their bioaccumulation results in carcinogenic and cytotoxic effects [110]. Therefore, there is an urgent need to develop novel remediating approaches to tackle these organic pollutants [50,111]. Among the methods used for contaminants removal, photocatalysis is considered highly promising due to its ability to generally convert organic pollutants into non-toxic compounds (CO_2 and H_2O), in addition to the possibility of using solar energy during the process [50].

Catalysts based on TiO_2 [112], ZnO [113], MOFs [114], MoS_2 [115], and BiOBr [116], have been widely used in the degradation of organic contaminants. Additionally, a strategy to improve their photocatalytic properties and increase their degradation efficiency is to combine two semiconductors to form a heterojunction [117–119]. In this direction, MOF MIL-88A and bismuth tungstate (Bi_2WO_6) have been used isolated in the degradation of the antibiotic tetracycline, with efficiencies of 46.5 % and 51 %, respectively, after 80 minutes, while MIL-88A/Bi_2WO_6 junction exhibited better performance, with an efficiency of 70.6 % [105]. Nevertheless, a challenge in using particulate catalysts is their recovery for reuse. To address this shortcoming, a possible strategy to facilitate their application and reuse is to fix them in varied matrices [120,121]. Recently, NH_2-MIL-125(Ti) MOF and MoS_2-based catalysts were synthesized and incorporated into carbon fibers, demonstrating high efficiency (94.3 %) in the removal of methylene blue (MB) dye [122]. Other hydrogel-based matrices have also been employed effectively for pollutant removal[123–126].

Hydrogels based on polysaccharides, such as alginate and carboxymethylcellulose, and polypeptides such as gelatin, have great potential for the development of functional materials applied in the remediation of contaminated water resources. Advantageous properties include hydrophilicity, porosity, biodegradability, wide availability, non-toxicity, reusability, and low cost [127,128]. Furthermore, the synergy between alginate, carboxymethylcellulose (CMC), and gelatin allows increasing the

interactions between the polymers, improving the mechanical resistance of the hydrogel, as well as allowing the efficient cross-linking of the polymer chains through the addition of metallic ions such as Ca^{2+}, Ba^{2+}, and Fe^{3+} [81,129–131].

In recent years, the 3D printing technique has gained prominence in producing platforms from hydrogels, capable of meeting the demands required for environmental applications [132–134]. Aiming to enhance the performance of these materials in removing organic pollutants, a viable solution is to freeze-dry the printed material, thus creating highly porous aerogels, with low density and high surface area [76,88,135]. The combination of these characteristics with the ability to process this material into different sizes and shapes enables the creation of versatile structures for various applications [136].

In this context, here we produced aerogels based on alginate, CMC, and gelatin incorporated with MOF MIL88-A/MoS_2 using the 3D printing technique. The system was shown capable of promoting the mutual adsorption and photodegradation of organic pollutants, in which methylene blue dye was employed as a model, as illustrated in Scheme 1.

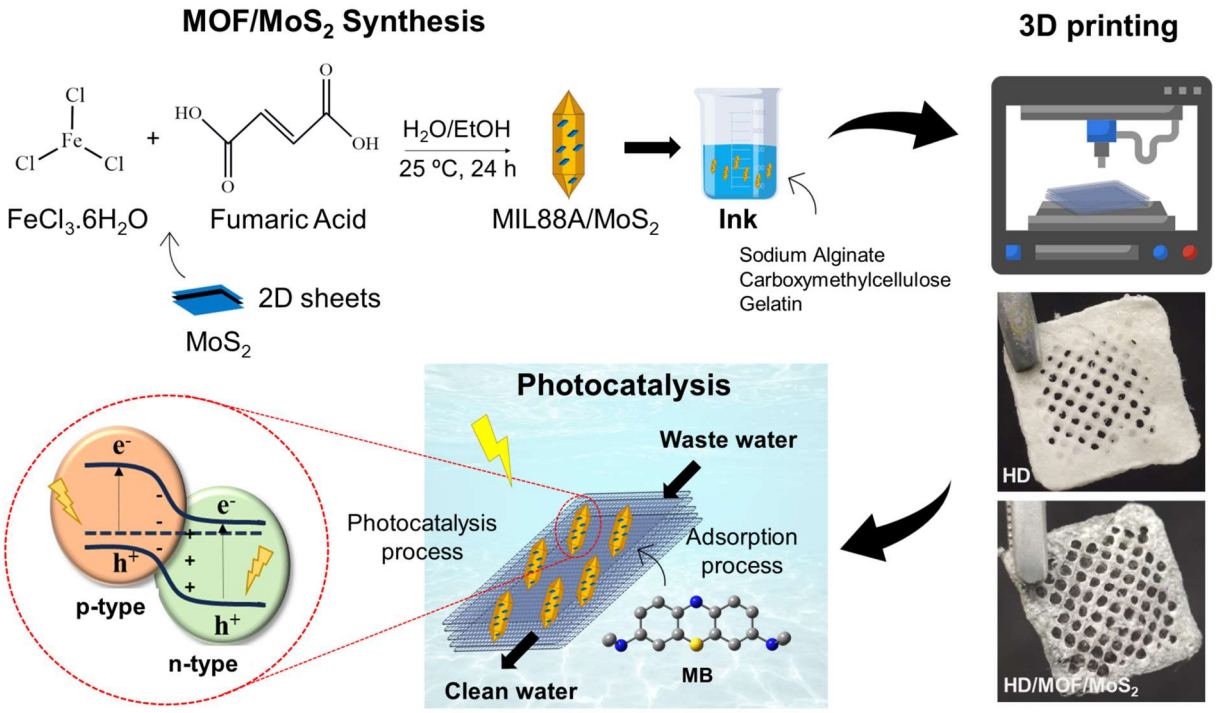

Scheme 1. Schematic illustration of the manufacture of aerogels incorporated with MOF MIL88A/MoS_2 used in photocatalysis experiments for degradation of dyes present in water. Reprinted with permission from dos Alves et al[109] Copyright 2024, Elsevier.

3.2 Materials and Methods

3.2.1 Materials

Iron (III) chloride hexahydrate ($FeCl_3.6H_2O$) was acquired from Sigma-Aldrich, fumaric acid ($C_4H_4O_4$) from Scientific Exodus, L-Cysteine ($C_3H_7NO_2S$) from Panreac, sodium molybdate (Na_2MoO_4) from Synth, ethanol (≥ 99.5 %). Alginic acid sodium salt from brown algae (CAS registry number: 9005-38-3, weight-averaged molecular weight (Mw) = 250.000 - 350.000 Da, medium viscosity ratio of D-mannuronate to L-gulunorate (M/G ratio) = 1.56) from Sigma-Aldrich. Carboxymethylcellulose sodium salt P.A. (CAS registry number: 9004-32-4, viscosity 1 % solution: 2000 – 3000 cps, pH 1 % solution: 6.5 – 8.5) from Synth. Gelatin extracted from porcine skin (type A, CAS registry number 9000-70-8), weight-averaged molecular weight Mw = 50.000 – 100.000 Da, gel strength 300 g Bloom) from Sigma-Aldrich. Sodium phosphate (Na_2HPO_4), and monosodium phosphate (NaH_2PO_4) from Scientific Exodus and Barium Chloride ($BaCl_2$) from Synth.

3.2.2 Methods

3.2.2.1 Preparation of MOF/MoS_2-based photocatalysts

3.2.2.1.1 Synthesis of MoS_2

The MoS_2 was synthesized by hydrothermal method according to the literature [137]. Firstly, 0.2517 g of L-cysteine and 0.19 g of sodium molybdate were dissolved in 15 mL and 10 mL of ultrapure water, respectively. After 5 min of stirring, with total dissolution, the solutions were mixed in a 50 mL Teflon cup, which was transferred to a stainless reactor. The synthesis temperature was set at 200 °C for 1020 min, with a heating rate of 3 °C.min^{-1}. At the end of the synthesis, the suspension was centrifuged for 10 min at 8000 rpm, washed with ultrapure water 3 times, and dried in a circulation oven at 40 °C for 48 h.

3.2.2.1.2 Preparation of MOF/MoS_2

The heterojunction MOF/MoS_2 was prepared based on the addition of MoS_2, obtained previously, to the MOF synthesis. Specifically, the procedure for obtaining MOF MIL-88A was based on a methodology previously described in the literature, with some modifications [53]. Firstly, 1.0812 g of $FeCl_3.6H_2O$ and 0.464 g of fumaric acid were

dissolved in 10 mL of ultrapure water and 10 mL of ethanol, respectively. Both solutions were stirred until completely dissolved. Next, the solutions were mixed and 100 mg of MoS_2 was then added to it. The final mixture was kept under stirring for 24 hours at room temperature. The solid denoted as MOF/MoS_2, was centrifugated for 10 min at 8000 rpm and washed 3 times with water and ethanol. Finally, it was dried in a circulation oven at 40 °C for 48 h.

3.2.2.1.3 Fabrication 3D printing aerogels

The development of hydrogels for 3D printing was based on a combination of SA, CMC, and Gel biopolymers. SA allows ionic cross-linking of polymer chains via Ba^{+2}, CMC was used to improve thinning behavior, and gelatin was used to make hydrogels thermoresponsive. So, the 3D printing hydrogels were prepared by first solubilizing sodium alginate (SA) and carboxymethylcellulose (CMC) in 10 mL of PBS under constant stirring at 50°C. The gelatin was solubilized in 5 mL of PBS at 40 °C in another beaker. After the gelatin (Gel) was solubilized, the MOF/MoS_2 was added. Next, the Gel/MOF/MoS_2 suspension was mixed (v/v) with the SA/CMC solution to obtain Gel/SA/CMC printing hydrogels (5 % w/v) containing MOF/MoS_2 at concentrations of 5 and 7.5 wt %. The hydrogels HD, HD/MOF/MoS_2 5 %, and HD/MOF/MoS_2 7.5 % were then stored under refrigeration (~ 4 ºC) until used for printing. After printing, the hydrogels were immersed in a 0.1 mol.L^{-1} $BaCl_2$ solution for 10 minutes for cross-linking[138–140].

Finally, the hydrogels were frozen at -20 °C and freeze-dried for 48 h, forming a porous aerogel. The aerogel containing only the biopolymers was named HD, and the aerogels containing the particulate in different amounts were named HD/MOF/MoS_2 5 % and HD/MOF/MoS_2 7.5 %. The structures were built by the Simplify 3D software and manufactured using a 3D printer (Genesis™, Solutions 3D Biotechnology, Brazil), with 0.01 mm accuracy in the x and y axes, and 0.005 mm accuracy in the z-axis. The pieces were printed in a square format containing 10 layers of 0.15 mm each, and the dimensions were fixed at 20 × 20 × 1.5 mm. The printing parameters (optimized in subsidiary experiments) were: speed of 400 mm/min, needle diameter of 0.41 mm, extrusion multiplier of 0.04, and temperature of 25 ºC. The choice of Ba^{2+} as a crosslinking agent is justified by its high affinity with SA, which results in the formation of a dense polymeric network, providing mechanical resistance to the material [141,142]

3.2.3 Microstructure characterization

The morphologies of samples were investigated by scanning electron microscopy (SEM) using a JEOL JSM-6510 and the chemical composition was determined by energy dispersive X-ray spectrometer (EDS) with JEOL JSM-6510 Fourier transform infrared (FTIR) spectra were obtained in ATR mode using Bruker equipment (Vertex 70), from 4000 – 400 cm^{-1}, using 64 scans and a resolution of 4 cm^{-1}. The X-ray diffraction analyses (XRD) were carried out in a Shimadzu XRD-6000 equipment, from 5 to 70°, scanning velocity of 2°.min^{-1}. The thermogravimetric analysis (TGA) was carried out using a SDT650 (instrument TA), at a ramp rate of 10 °C. min^{-1}, temperature range of 25 – 600 °C under nitrogen atmosphere.

To determine the porosity of the aerogels, the values of bulk density (ρ_b) and skeletal density (ρ_s) were obtained. The bulk density was calculated using equation (1) [143], where the volume was calculated from measurements (n =5) obtained by a digital caliper (Mitutoyo with instrumental error ± 0.02 mm), and the mass was obtained on an analytical balance (Shimadzu-AUY220). The skeletal density was determined using a helium pycnometer (MVP-6DC from Quantachrome Instruments). The porosity and pore volume of the aerogels were determined using equations (2) and (3) [143], respectively.

$$\rho_b = \frac{\text{aerogel mass}}{\text{aerogel volume}} \qquad Eq.(1)$$

$$Porosity\ (\%) = \left(1 - \frac{\rho_b}{\rho_s}\right) \times\ 100 \qquad Eq.(2)$$

$$Pore\ volume\ (cm^3.g^{-1}) = \left(\frac{1}{\rho_b} - \frac{1}{\rho_s}\right) \qquad Eq.(3)$$

3.2.4 Degree of swelling

The degree of swelling (S_d %) was analyzed according to the water absorption capacity of the printed structures, at room temperature. The masses were weighed at specific time intervals until a constant weight was obtained. The S_d % was determined using equation (4) [144]:

$$S_d\% = \frac{w_t - w_0}{w_0} \times\ 100 \qquad Eq.(4)$$

, where w_0 is the initial mass and w_t is the mass of the sample at time t.

3.2.5 Rheological analysis

The rheological behavior of the hydrogels was analyzed using a Physica Anton Paar MCR 301 Rheometer. Tests were performed at 25 °C using a plate-to-plate geometry (PP25) with a diameter of 25 mm and a gap of 1 mm. For that, amplitude sweep tests were performed at a constant frequency of 10 rad.s^{-1} with strain in the range of 0.1 to 1000 % to determine the region of linear viscoelasticity (LVR). After determining the LVR, a flow sweep was performed, applying a shear stress from 0.01 to 100 %. Finally, the viscosity recovery test was carried out as a function of time (thixotropy) to simulate hydrogel printing conditions. For this, the test was performed in three intervals: (i) applying a constant low shear rate of 0.1 s^{-1} for 60 s, (ii) a high shear rate of 100 s^{-1} for 10 s, and (iii) a low shear rate of 0.1 s^{-1} for 70 s. All characterizations were performed in triplicate.

3.2.6 Adsorption experiments

For adsorption analysis, HD, HD/MOF/MoS_2 5 and 7.5 % aerogel structures weighing 40 – 60 mg were immersed in 20 mL of MB solutions with a concentration of 5 mg.L^{-1}. These experiments were conducted in the dark. After specific time intervals, approximately 3 mL of aliquots were collected, and the MB adsorption was analyzed at the maximum absorption wavelength of 664 nm using a UV spectrophotometer. Control analyses were performed with HD/MOF 5 and 7.5 %. The removal efficiency was calculated according to equation (5), and the adsorbed quantity of pollutant at time *t* (q_t, mg.g^{-1}) was calculated according to equation (6) [7]:

$$R\,\% = \frac{C_0 - C_t}{C_0} \times 100 \qquad \text{Eq. (5)}$$

$$q_t = \frac{(C_0 - C_t) \times V}{m} \qquad \text{Eq. (6)}$$

, where C_0 is the initial dye concentration (mg.L^{-1}), C_t is the concentration at time t (mg. L^{-1}), V is the volume (L), and m is the adsorbent mass (g).

The adsorption experiment results were evaluated using pseudo-first order and pseudo-second order kinetic models, according to equations (7) and (8) [7], respectively:

$$q_t = q_e(1 - \exp(-k_1 t)) \quad \text{Eq. (7)}$$

$$q_t = \frac{t}{\left(\frac{1}{k_2 q_e^2}\right) + \left(\frac{t}{q_e}\right)} \quad \text{Eq. (8)}$$

, where q_e (mg.g^{-1}) is the amount of dye adsorbed in the equilibrium, k_1, and k_2 are the equilibrium constants of pseudo-first order and pseudo-second order, respectively, and t is the contact time (min).

3.2.7 Photocatalytic degradation experiments

For the photodegradation analysis, the experiments were conducted according to the procedure described in section 3.2.6, but firstly, the solutions were left in the dark for 30 min and after this time, the solutions were irradiated by 6 UV lamps (Fig. S1). As in degradation tests, control analyses were performed with HD/MOF 5 and 7.5 %. The degradation efficiency (R%) was calculated according to equation (5), described previously. Reuse tests were performed with the HD, HD/MOF/MoS_2 5 and 7.5 % aerogels, where the structures were washed with ultrapure water and dried at room temperature after each cycle.

3.3 Results and discussion

3.3.1 Rheology

The viscoelastic behavior of materials based on polymers for 3D printing can be understood through the response of the G' and G" moduli as a function of deformation or tension [145–147]. This behavior provides important information about the ability to obtain self-supporting 3D-printed structures [148]. Fig. 3.1(a) shows the behavior of G' and G" for HD, HD/MOF/MoS_2 5 % and 7.5 % hydrogels depending on the variation of deformation. It is observed that for all hydrogels within the LVR (G' > G"), suggesting that the hydrogels produced have elastic (solid) material behavior. On the other hand, outside the LVR, G' and G" are affected by the imposed deformation rate, therefore, it was observed that at approximately 300 % deformation the flow point (G' = G") occurred [149,150]. After this point, G" surpasses G, showing that viscous behavior (liquid) prevails over elastic behavior (solid). This result demonstrates that the hydrogels could flow under deformation and suggests their potential for use in 3D extrusion printing applications. Furthermore, it is also noted that the incorporation of the MOF/MoS_2

increased both the G' and G" values, indicating an increase in mechanical resistance [151,152].

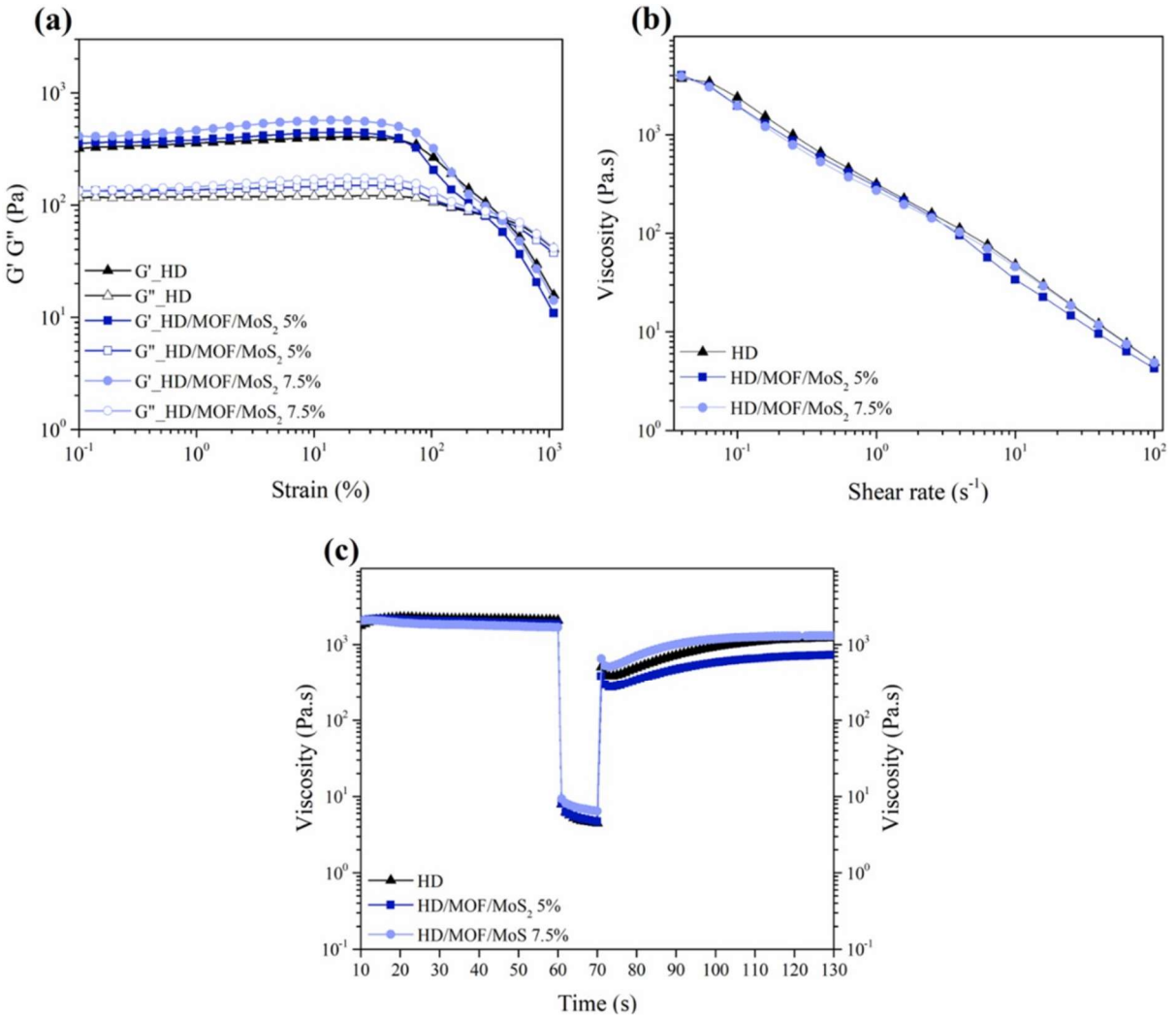

Figure 3.1. Rheological characterization of hydrogels HD; HD/MOF/MoS_2 5 % and HD/MOF/MoS_2 7.5 %. (a) G' and G" (MPa) as a function of strain (%). (b) viscosity (Pa.s) as a function of shear rate (s^{-1}). (c) viscosity as a function of time (s). Reprinted with permission from dos Alves et al[109] Copyright 2024, Elsevier.

Aiming to evaluate the shear-thinning behavior, Fig. 3.1(b) presents the viscosity curves (flow curve) as a function of the shear rate of HD, HD/MOF/MoS_2 5 %, and 7.5 % hydrogels. It is observed that at low shear rates of 0.01 – 0.1 s^{-1}, HD, HD/MOF/MoS_2 5 %, and HD/MOF/MoS_2 7.5 % hydrogels present zero viscosity (η_o) of 3710, 4017, and 3903 Pa.s, respectively. This result suggests that materials constructed from hydrogels have their mechanical stability preserved after deposition on the printing surface [153]. On the other hand, above 0.1 s^{-1} it is possible to notice that the η_o value reduces as the shear rate increases, which behavior is characteristic of pseudoplastic materials (shear-thinning) and ideal for 3D printing by extrusion [154]. At a rate of 100 s^{-}

[1], HD, HD/MOF/MoS_2 5 %, and HD/MOF/MoS_2 7.5 % hydrogels presented viscosity values of 4.91, 4.26, and 4.85 Pa.s, respectively. This result illustrates the capability of hydrogels to flow effectively under high shear rates, a desirable characteristic for materials intended for 3D printing through extrusion [155]. To investigate the influence of the incorporation of MOF/MoS_2 in the hydrogels, the viscosity curves (Fig. S2, S3, and S4) were adjusted as a function of the shear rate using the Cross model [156] which takes into account the viscosity values at zero (η_o) and infinity (η_∞), the consistency index (k), the applied shear rate ($\dot{\gamma}$), and the Cross-flow index (m) that allows the pseudoplastic character to be evaluated, according to equation (9) [156]:

$$\eta = \eta_\infty + \frac{(\eta_o - \eta_\infty)}{(1 + k\dot{\gamma}^m)} \qquad Eq.(9)$$

The adjusted values presented in Table 3.1 reveal that all hydrogels exhibit n < 1, consistent with the pseudoplastic nature of materials. The values of n were determined using the relationship (m = 1 - n).

Table 3.1. Based on the Cross model, the coefficient values (n and K) adjusted for HD, HD/MOF/MoS_2 5 %, and HD/MOF/MoS_2 7.5 % hydrogels.

Hydrogel	n	K (Pa.s^n)	R^2
HD	0.29 ± 0.04	8.85 ± 1.09	0.977
HD/MOF/MoS_2 5%	0.19 ± 0.02	13.25 ± 0.90	0.995
HD/MOF/MoS_2 7.5%	0.17 ± 0.03	13.89 ± 1.10	0.994

It is observed in Table 3.1 highlights a reduction in the value of n as the concentration of MOF/MoS_2 increased, indicating an enhancement in the shear-thinning behavior with the incorporation of MOF/MoS_2 in the hydrogels. Therefore, the HD/MOF/MoS_2 7.5 % hydrogel exhibited a reduced value of n = 0.17, indicating a greater tendency for molecular entanglements to align more easily in the direction of shear flow. Consequently, the viscosity decreases with increasing shear flow rate [157]. Conversely, the HD hydrogel presented n = 0.29, indicating that the shear-thinning behavior is less pronounced when compared to the other two hydrogels.

The hydrogels were also evaluated regarding their initial recovery capacity after deposition on the printing surface. Thus, the thixotropy test was carried out at intervals of three times (3ITT) to evaluate the viscosity recovery capacity as a function of time [158], as shown in Fig. 3.1(c). At the time of printing we highlighted three conditions in

which the shear rate varies as the hydrogel is extruded: (1) refers to the hydrogel inside the syringe (low shear), where solid (gel) behavior prevails over viscous behavior (G' > G"), (2) when the hydrogel is forced through the printing nozzle (high shear), the 3D network formed by the cross-linking of the polymer chains is broken by the shear action (G" > G'), and (3) after leaving the needle (low shear) and being deposited on the printing surface, the polymer chains tend to recover the 3D network broken by shear, thus allowing partial or total viscosity recovery (self-healing) over time [159–161]. Table 3.2 presents the viscosity values at three different moments, wherein the first moment the hydrogels were subjected to a shear rate of 0.1 s^{-1} for 60 s (η_1), in the second 100 s^{-1} for 10 s (η_2) and finally 0.1 s^{-1} for 60 s ($\eta 3$).

Table 3.2. Viscosity values of HD, HD/MOF/MoS_2 5 %, and HD/MOF/MoS_2 7.5 % hydrogels at three different times under specific shear rates.

Hydrogel	η_1 (Pa.s)	η_2 (Pa.s)	η_3 (Pa.s)	Recovery (%)
HD	2081 ± 62	4.5 ± 0.7	1221 ± 144	59
HD/MOF/MoS_2 5 %	1860 ± 33	4.70 ± 0.6	733 ± 49	39
HD/MOF/MoS_2 7.5 %	1690 ± 115	6.4 ± 0.3	1307 ± 37	77

As shown in Table 3.2, it is observed that the hydrogels under low shear have initial viscosity values (η_1) ranging from 1700 to 2080 Pa.s. Nevertheless, when the shear rate increased to 100 s^{-1}, all hydrogels showed a low viscosity value (η_2), again highlighting the shear-thinning behavior of the materials. The HD hydrogel composed only of SA/CMC/Gel managed to recover 59 % of the initial viscosity value. On the other hand, the presence of MOF/MoS_2 changed the thixotropic behavior of the hydrogels in the 3ITT test. In the case of the hydrogel HD/MOF/MoS_2 5 %, the viscosity recovery was 39 %, demonstrating that the MOF/MoS_2 increased the thixotropic character of the material. In contrast, increasing the amount of MOF/MoS_2 to 7.5 % allowed the initial viscosity to be recovered by 77 %. This result indicates that increasing the MOF/MoS_2 concentration in the hydrogel favored greater viscosity recovery, which suggests the construction of printed structures with good dimensional stability [162–164].

3.3.2 Characterizations of the aerogels

The morphological characteristics of the printed structures were evaluated with the micrographs shown in Fig. 3.2 and Fig. S7, while the micrographs of MOF/MoS_2 are presented in Fig. S5 and S6. The MOF crystals exhibit elongated hexagonal shapes [165], and the MoS_2 tends to form clusters around the MOF. The measurements obtained for MOF diameters and lengths were 0.221 ± 0.060 μm and 1.063 ± 0.235 μm, respectively. The SEM micrographs shown in Fig. S7 surface and cross-section of HD/MOF/MoS_2 7.5 %, exhibit some structures dispersed throughout the matrix, identified as MOF/MoS_2 incorporated into the hydrogel. The elemental mapping obtained by EDS reveals the elements present in the samples in addition to confirming the presence of MOF/MoS_2 at hydrogels, as illustrated in Fig. S8. The elements C and O originate from polymers, while Fe is derived from the metallic center of the MOF. All structures present barium due to the crosslinking process with $BaCl_2$. SEM micrographs presented in Fig. 3.2(a), (b), and (c) indicate the presence of roughness and irregularities on the material surface, in addition to the presence of small pores. Fig. 3.2(d) and (e) show the macroscopic appearance of the aerogels.

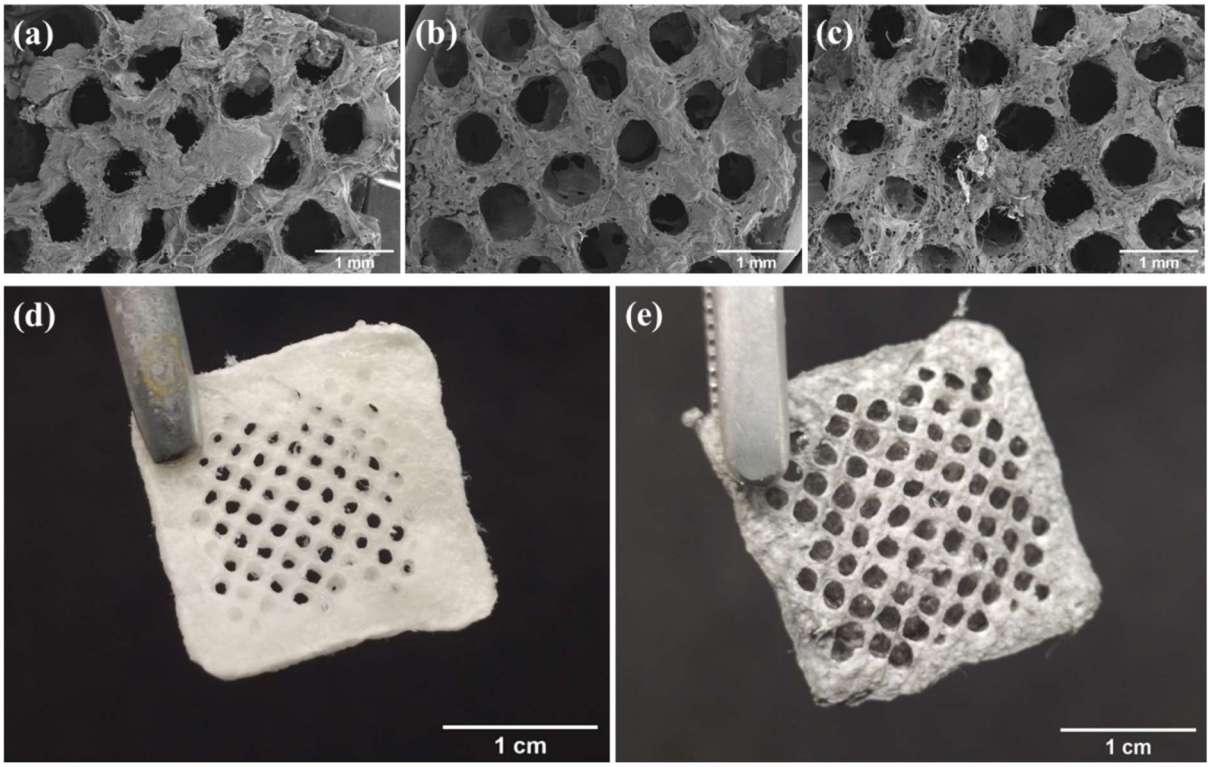

Figure 3.2. Morphological characterization of aerogels. SEM images of printed structures (a) HD; (b) HD/MOF/MoS_2 5 % and (c) HD/MOF/MoS_2 7.5 %. Digital photos (d) HD and (e) HD/MOF/MoS_2 7.5 %, respectively. Reprinted with permission from dos Alves et al[109] Copyright 2024, Elsevier.

During freeze-drying, the ice crystals present in the hydrogels sublime, forming the pores observed in the micrographs SEM (Fig. 3.2) [166]. The irregularities and roughness observed can also be attributed to the freezing and freeze-drying processes [144]. The values of porosity, bulk and skeletal densities, and pore volume were obtained for the materials and are described in Table 3.3. It is noted that the incorporation of MOF/MoS_2 results in an increase in density, while the porosity remains above 80 %, which is consistent with values reported in the literature for polymeric aerogels [167,168].

Table 3.3. Values of porosity, bulk (ρ_b) and skeletal (ρ_s) densities, and pore volume for the developed aerogels.

Sample	Porosity (%)	ρ_b (g.cm^{-3})	ρ_s (g.cm^{-3})	Pore volume (cm^3.g^{-1})
HD	85.04	0.09 ± 0.01	0.60 ± 0.02	9.5
HD/MOF/MoS_2 5 %	81.54	0.15 ± 0.04	0.83 ± 0.04	5.3
HD/MOF/MoS_2 7.5 %	90.00	0.08 ± 0.08	0.87 ± 0.07	11

The FTIR spectra shown in Fig. 3.3(a) allow the identification of the main functional groups of the materials used in the hydrogel formulation. For gelatin, the peaks at 3280, 1627 e 1525 cm^{-1} can be attributed to the stretching vibrations of amine groups (N-H), amide I vibration, and amide II vibration, respectively [82]. For alginate and carboxymethylcellulose, the broader bands observed in the 3500 – 3000 cm^{-1} region represent the stretching vibrations of hydroxyl groups (-OH), and the bands at 1592 and 1415 cm^{-1} characterize the asymmetric and symmetric stretching of carboxylic groups (-COOH), respectively [82,169].

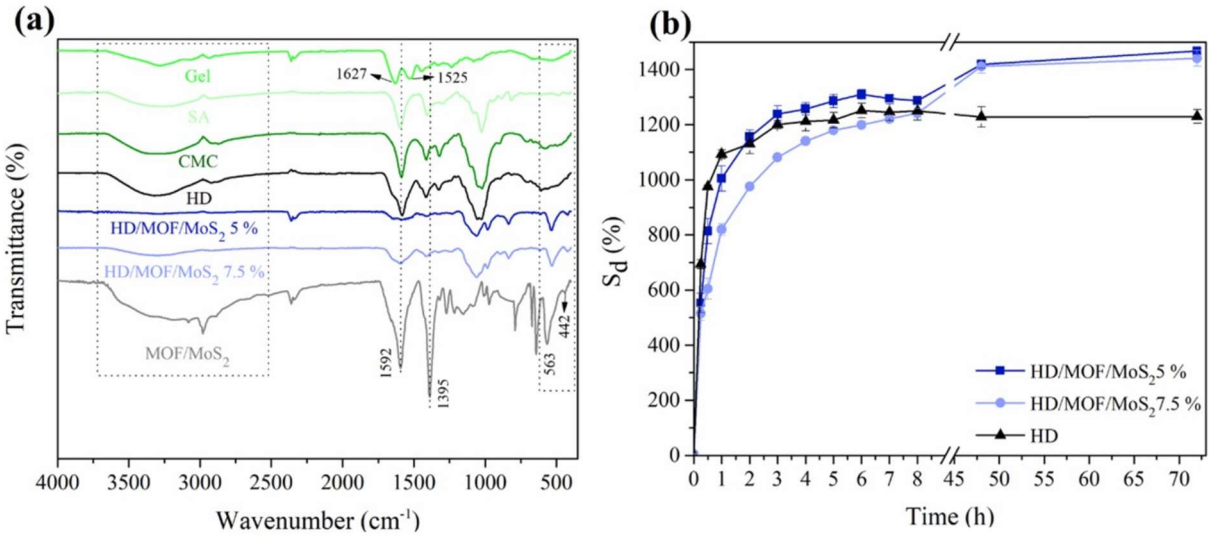

Figure 3.3. (a) FTIR spectra for the Gel, SA, CMC, HD, HD/MOF/MoS_2 5 %, HD/MOF/MoS_2 7.5 %, and MOF/MoS_2, respectively. (b) Swelling capacity of HD/MOF/MoS_2 5 %, HD/MOF/MoS_2 7.5 %, and HD printed materials. Reprinted with permission from dos Alves et al[109] Copyright 2024, Elsevier.

The spectrum of the MOF/MoS_2 shows bands corresponding to Fe-O and Mo-S stretching vibrations at 563 and 442 cm^{-1}, respectively [114,170]. The spectrum HD/MOF/MoS_2 composite spectrum shows the bands corresponding to Fe-O and Mo-S with a shift from 563 to 528 cm^{-1} and from 442 to 416 cm^{-1}, respectively, which may indicate chemical interactions between the polymers and the MOF/MoS_2 crystals. Furthermore, a decrease in the FTIR band intensities was observed in the interval between 3500 – 3000 cm^{-1} and 1592 cm^{-1} – 1415 cm^{-1} regions, corresponding to the stretching of hydroxyl and carboxylic groups of the polymers, respectively, corroborating these interactions [81,171].

The water absorption capacity for the printed structures were investigated and are described in Fig. 3.3(b). The results show greater absorption capacity for the HD/MOF/MoS_2 composites, with S_d % ~1400 % for ~70 h, indicating that the addition of MOF/MoS_2 promoted a performance improvement. This variation can be attributed to the different molecular interactions that occur within the polymer networks of each hydrogel evaluated, which influence water mobility [144]. During the swelling tests, it was found that the structures containing MOF/MoS_2 demonstrated greater fragility over immersion time in water. Additionally, according to the pycnometry results, the high porosity values obtained for the aerogels (> 80%) contribute to the observed swelling behavior.

The TGA curves for the hydrogels are presented in Fig. 3.4(a), and the mass loss, $T_{onset,}$ and T_{endset} results for each stage are detailed in Table 3.4. From the results, it is noted that the decomposition of the three hydrogels analyzed occurs in three distinct stages.

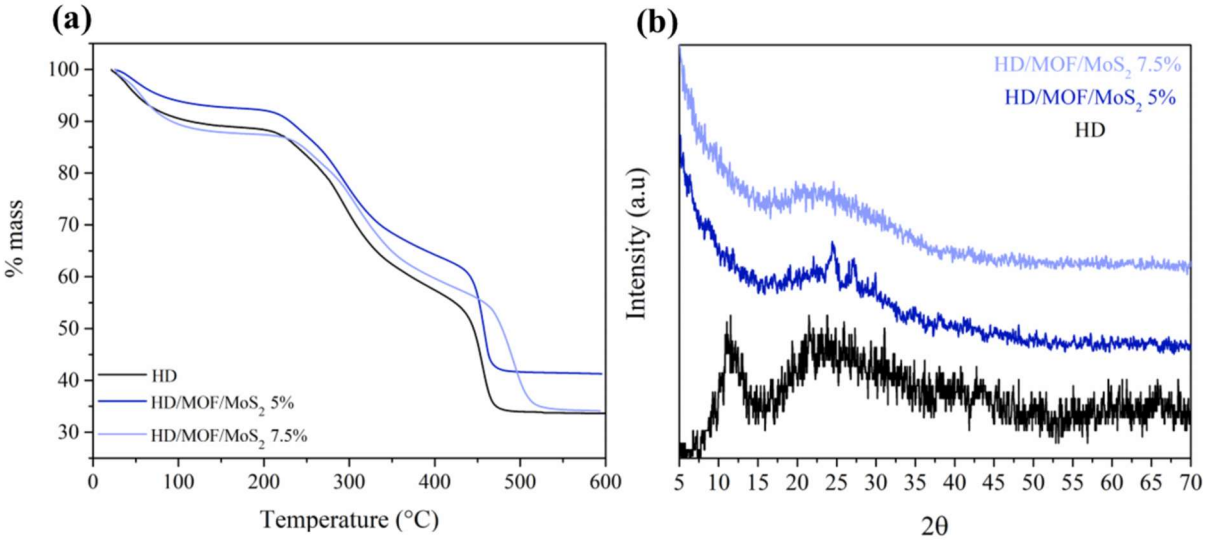

Figure 3.4. (a) TGA curves and (b) XRD analyses for HD, HD/MOF/MoS_2 5 % and HD/MOF/MoS_2 7.5 % printed structures. Reprinted with permission from dos Alves et al[109] Copyright 2024, Elsevier.

The first stage can be associated with loss of moisture present in the samples, representing a small percentage of mass loss. The second and third stages, which represent the greatest loss of mass, are associated with the decomposition of polymers, with the degradation of amino, carboxylic, and hydroxyl groups from gelatin, sodium alginate, and CMC [110,131,172]. However, the hydrogels containing MOF/MoS_2 show a shift in the TGA curves, and the T_{onset} and T_{endset} shift to higher temperatures, indicating the interaction of polymers with MOF/MoS_2 [172].

Table 3.4. Stages of thermal decomposition of HD, HD/MOF/MoS_2 5 % and HD/MOF/MoS_2 7.5 % printed structures.

Sample	Stage 1			Stage 2			Stage 3		
	mass (%)	T_{onset} (°C)	T_{endset} (°C)	mass (%)	T_{onset} (°C)	T_{endset} (°C)	mass (%)	T_{onset} (°C)	T_{endset} (°C)
HD	11	25	140	35	200	430	21	425	480
HD/MOF/MoS_2 5 %	8	25	155	31	205	440	20	433	480
HD/MOF/MoS_2 7.5 %	13	25	162	32	225	465	20	462	526

The XRD analyses for the HD and HD/MOF/MoS_2 samples are shown in Fig. 3.4(b). The HD presents an XRD pattern with a characteristic profile of the polymers that make up the hydrogel, following what is described in the literature [81]. As the polymers in question are not crystalline, the observed peaks have a broad appearance, indicating their amorphous nature. The patterns obtained for the HD/MOF/MoS_2 samples present smoothed peaks, in addition to a new peak in the range of 5 – 10°, indicating interactions or the polymers with Ba^{2+} and MOF/MoS_2 [173].

3.3.3 Adsorption tests

The adsorption efficiency for HD, HD/MOF/MoS_2 5 %, and HD/MOF/MoS_2 7.5 % was evaluated by keeping the samples in the dark with MB solutions at 5 $mg.L^{-1}$, as illustrated in Fig. 3.5. The results show that HD reached its maximum efficiency (16.77 %) in 20 minutes. After this period, a decrease in material efficiency was observed, probably due to the dye desorption process. Conversely, the HD/MOF/MoS_2 5 % and HD/MOF/MoS_2 7.5 % samples exhibited maximum efficiencies of 28.66 % and 95.86 %, respectively, at different time intervals. On the other hand, the results of the control tests conducted with HD/MOF 5% and 7.5 % are described in Fig. S9 and show that the efficiency for these materials did not exceed 20 %.

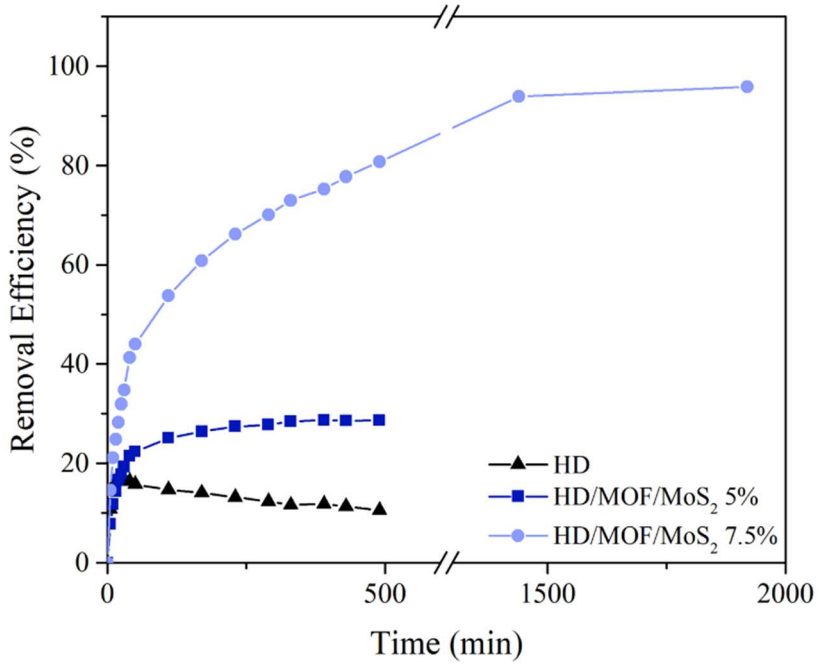

Figure 3.5. Removal efficiency for adsorption of HD, HD/MOF/MoS_2 5 % and HD/MOF/MoS_2 7.5 % aerogels. Reprinted with permission from dos Alves et al[109] Copyright 2024, Elsevier.

The adsorption kinetics were described using the pseudo-first-order and pseudo-second-order models [7], according to the results shown in Table 3.5. The correlation coefficients obtained for HD/MOF/MoS_2 5 % and HD/MOF/MoS_2 7.5 % were better for the pseudo-second-order model, with R^2 values of 0.998 and 0.964, respectively, indicating that the adsorption process is governed by chemisorption, possibly due to the electrostatic interaction between the negatively charged MOF/MoS_2 and the cationic MB. For HD, the best fit was with the pseudo-first-order kinetics, with an R^2 value of 0.999, suggesting physical interactions between HD polymers and MB[174].

Table 3.5. Parameters for adsorption kinetics models of HD, HD/MOF/MoS_2 5 % e HD/MOF/MoS_2 7.5 %.

Model	Material	Parameter	R^2
Pseudo-first order	HD	Q_e = 0.4671 ± 0.0024 k_1 = 0.2215 ± 0.0211	0.999
	HD/MOF/MoS_2 5 %	Q_e = 0.6089 ± 0.0106 k_1 = 0.0446 ± 0.0029	0.975
	HD/MOF/MoS_2 7,5 %	Q_e = 1.793 ± 0.0720 k_1 = 0.0179 ± 0.0028	0.903
Pseudo-second order	HD	Q_e = 0.5348 ± 0.0176 k_2 = 0.5313 ± 0.1035	0.993
	HD/MOF/MoS_2 5 %	Q_e = 0.6524 ± 0.0033 k_2 = 0.0994 ± 0.0027	0.998
	HD/MOF/MoS_2 7,5 %	Q_e = 2.035 ± 0.0614 k_2 = 0.0099 ± 0.0014	0.964

Considering the best kinetic fits the amount of dye adsorbed at equilibrium was q_e = 0.464 ± 0.003 mg.g^{-1} for HD, while the materials containing 5 % and 7.5 % MOF/MoS_2 exhibited q_e values of 0.652 ± 0.003 mg.g^{-1} and 2.04 ± 0.061 mg g^{-1}, respectively, as shown in Fig. 3.6(a) and (b).

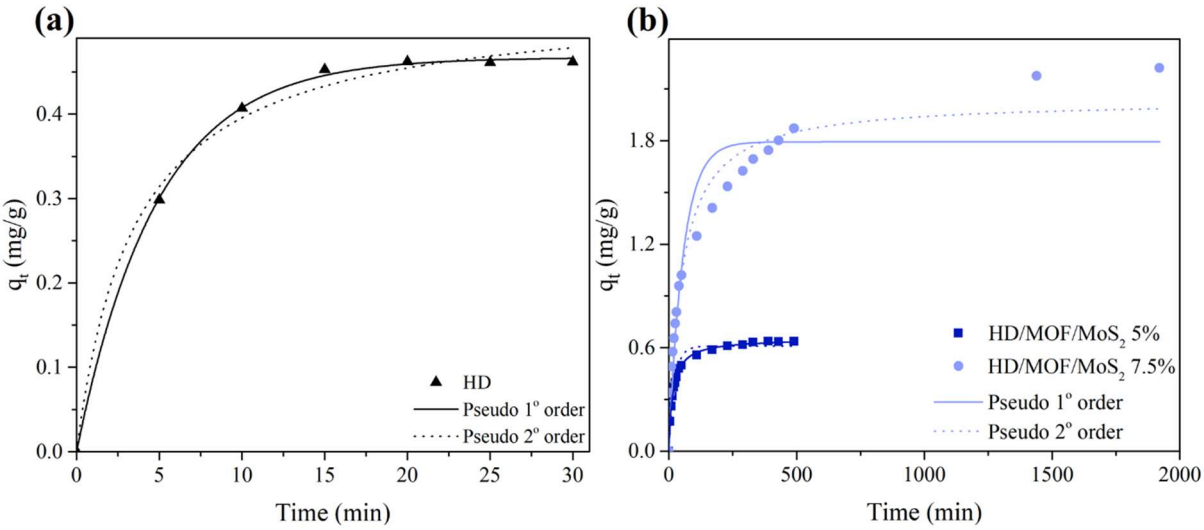

Figure 3.6. Adsorption kinetics models for (a) HD and (b) HD/MOF/MoS_2 5 % and HD/MOF/MoS_2 7.5 % aerogels. Reprinted with permission from dos Alves et al.[109] Copyright 2024, Elsevier.

The low efficiency for HD can be attributed to the low availability of adsorption sites for interaction with MB molecules. The carboxylic groups (COO^-) of SA and CMC that could be available to Interact with the cationic MB are connected to Ba^{2+} from the crosslinking process [84,175]. The Gel, in turn, has available amine groups, inefficient in MB adsorption via electrostatic interactions [176]. However, the addition of MOF/MoS_2 particles to the hydrogel resulted in an increased adsorption efficiency, probably due to the greater number of active sites with affinity to interact with MB molecules via electrostatic interactions [177,178], as shown in Figure 3.7. Considering the results described in the kinetic analyses, it is proposed that the cationic dye MB interacts with the carboxyl groups (COO^-) of the MOF MIL88-A and the Mo-S groups of MoS_2 through electrostatic interactions.

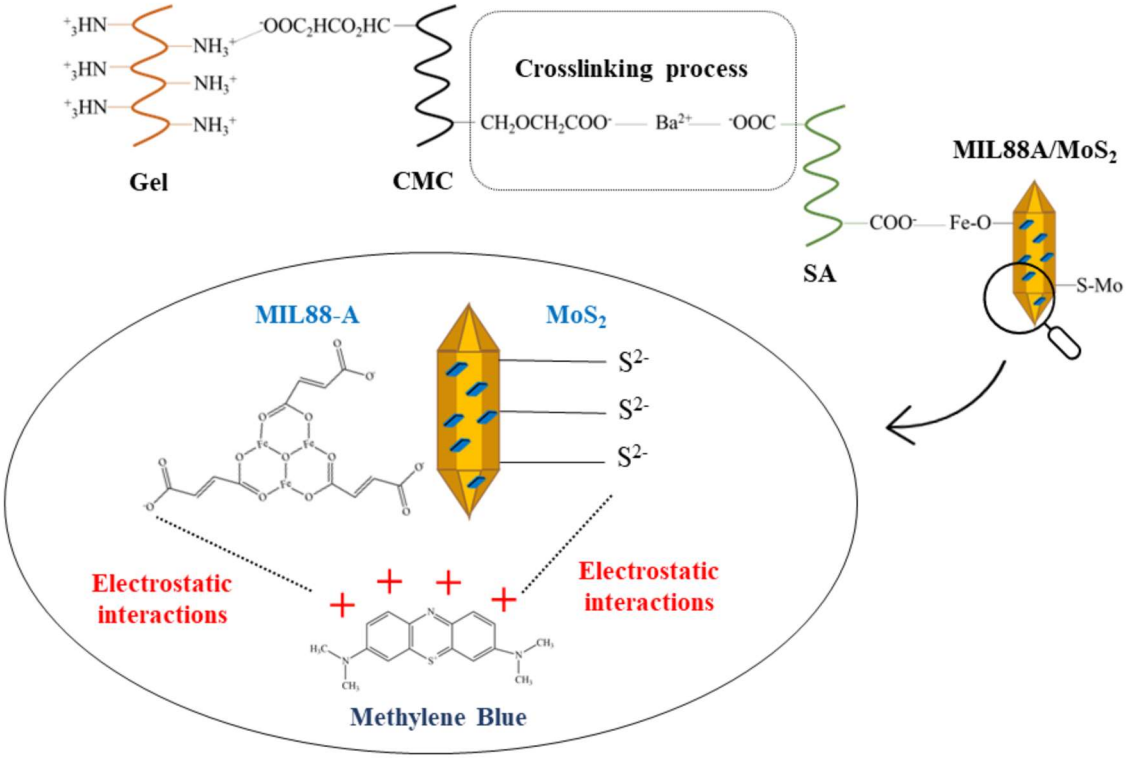

Figure 3.7. Proposed mechanism for adsorption of MB onto HD/MOF/MoS_2. Reprinted with permission from dos Alves et al.[109] Copyright 2024, Elsevier.

3.3.4 Photocatalytic activity

The photocatalytic activity of the materials was evaluated through the degradation of the MB dye under UV light irradiation. The samples were kept in the dark for 30 minutes for the initial dye adsorption in the initial stage, and the results described in Fig.3.8 indicated that, during this period, all the materials exhibited similar efficiency. The results of the control tests are described in Fig. S10, and show that the efficiency for HD/MOF 5 and 7.5 % did not exceed 60 %.

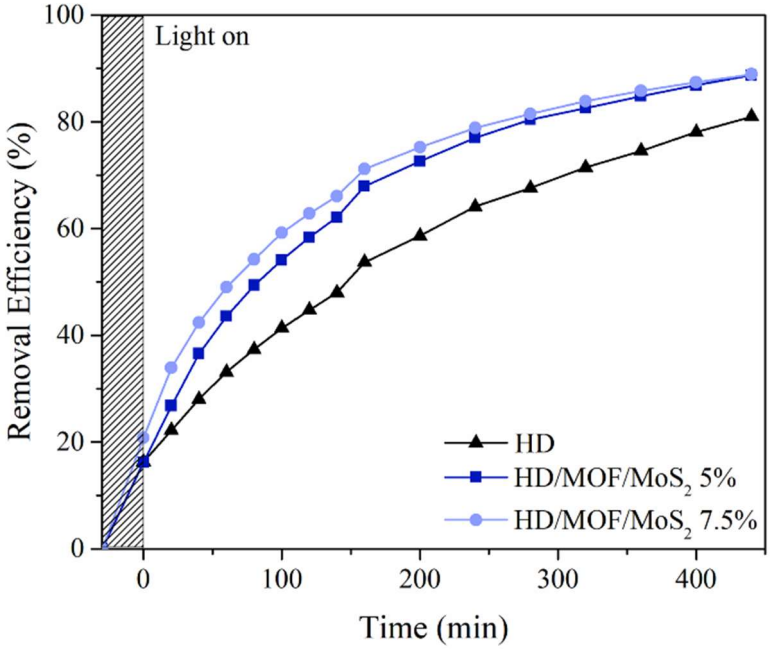

Figure 3.8. Removal efficiency for photocatalytic degradation using HD, HD/MOF/MoS_2 5 % and HD/MOF/MoS_2 7.5 % aerogels. Reprinted with permission from dos Alves et al.[103] Copyright 2024, Elsevier.

Subsequently, the samples were exposed to UV light irradiation for 440 minutes, revealing the progressive degradation of the dye, as described in Fig. 3.9(a) and illustrated in Fig. 3.9(c). At the end of the analysis, the HD/MOF/MoS_2 5 % and 7.5 % materials showed similar results, with efficiencies of approximately 89 %, while HD achieved an efficiency of 81 % (Fig. 3.8). In contrast to the results obtained in the adsorption analyses, HD also displayed promising results for photocatalysis, with efficiency very close to the materials containing the MOF/MoS_2 catalyst. We hypothesize that the observed phenomenon results from the incorporation of Ba^{2+} in the crosslinking process of the hydrogel, as shown in Fig. 3.7. These ions effectively form bonds with the carboxylic groups present in the polymer structures [139,179,180]. During light exposure, electrons originating from these groups can migrate to the barium sites, like what occurs in systems containing semiconductors, resulting in the photodegradation process of MB. Similarly, to HD, HD/MOF/MoS_2 5 % showed improved efficiency during photocatalysis. Some studies in the literature indeed employ barium as a dopant to enhance photocatalytic activity [181,182]. Furthermore, the kinetic degradation curve of the MB dye described in Fig. 3.9(b) was determined using the pseudo-first-order model based on the equation (10) [104]:

$$\ln\left(\frac{C_0}{C}\right) = kt \qquad Eq.(10)$$

The results indicate that the values of k for HD/MOF/MoS_2 5 % and 7.5 % are remarkably similar (0.0044 and 0.0043, respectively) and 1.33 times greater than the k value of HD.

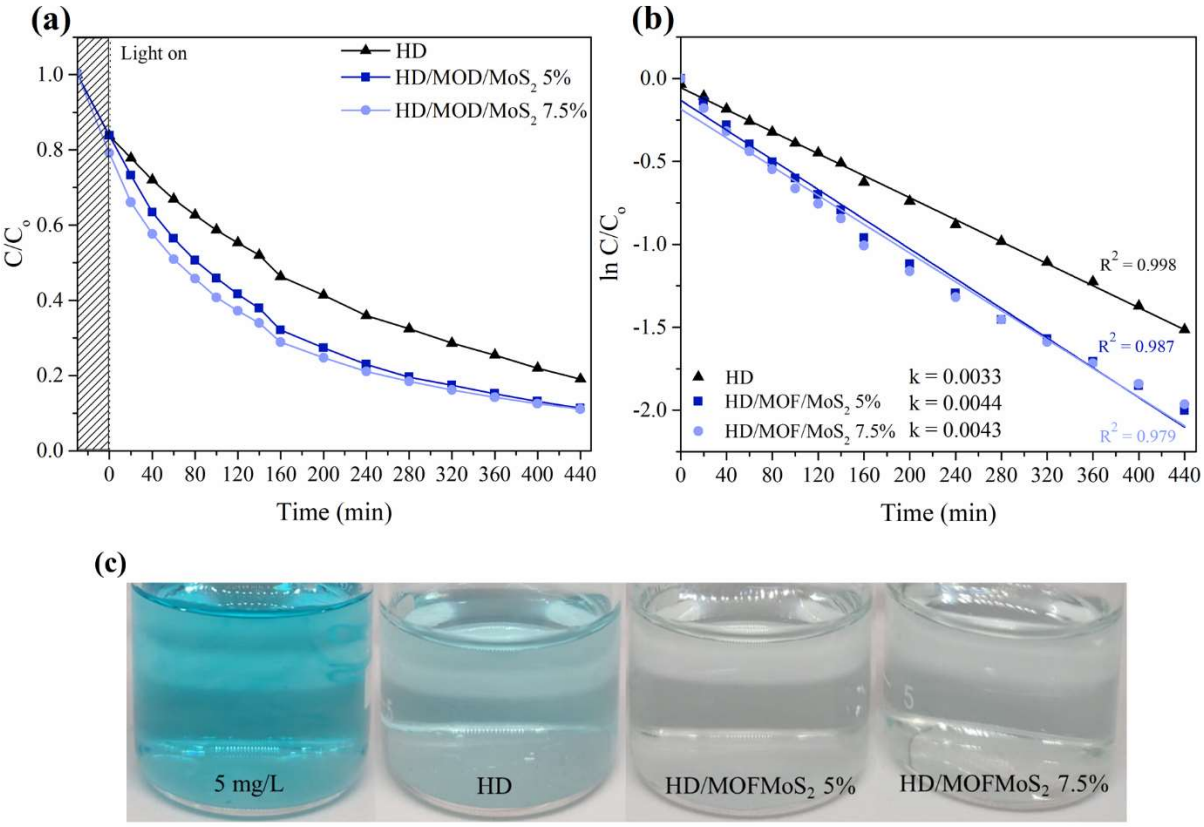

Figure 3.9. (a) Photocatalytic performance of aerogels under UV light; (b) pseudo-first-order kinetic degradation for MB and (c) illustration of dye degradation. Reprinted with permission from dos Alves et al[103] Copyright 2024, Elsevier.

The efficiencies of adsorption and photodegradation of MB by other materials reported in the literature are shown in Table 3.6. Compared to the works reported in the literature, the aerogels in the present study can be considered promising for MB removal, as they are efficient without the use of oxidizing agents, such as H_2O_2, which is employed in some studies as a source of radicals (•OH) to assist in the MB degradation process.

Table 3.6. Adsorption and photodegradation capacities of various materials are reported in the literature.

Catalyst	Photodegradation conditions	Efficiency (%)	Reference
α-MnO_2/GO/CS aerogel	30 mg/L, 60 min, with H_2O_2	90.7	[183]
Carbon aerogel/TiO_2	10 mg/L, 300 min	85	[184]
MnO_2 aerogel	5 mg/L, 70 min	86.7	[185]
$BaTiO_3$	5 mg/L, 50 min	64	[186]
$BaTiO_3$/TiO_2	10 mg/L, 180 min	72	[187]
g-C_3N_4	Without H_2O_2, 180 min With H_2O_2, 90 min	8.29 99.03	[188]
Ce/MoO_3	5 mg/L, 50 min	89	[189]
HD **HD/MOF/MoS_2 5 %** **HD/MOF/MoS_2 7.5 %**	5 mg/L, 440 min	81 89 89	This work
Adsorbent	**Adsorption conditions**	**Efficiency (%)**	**Reference**
cellulose-based composite aerogel	100 mg/L; 30 °C; 12 h	90	[190]
MCC/PDA aerogels	50 mg/L; 48 h	94.4	[191]
β-CD/GO	70 °C, 60 min	90	[192]
Lotus leaf	100 mg/L, pH 7; 4 h	>90	[193]
Co_3O_4/SiO_2	-	95.7	[194]
PT-GO	35 mg/L; pH 8	>90	[195]
HD/MOF/MoS_2 7.5 %	5 mg/L; 24 h	95.86	This work

Abbreviations: Graphene oxide (GO); chitosan (CS); microcrystalline cellulose (MCC); polydopamine (PDA); beta-cyclodextrin (β-CD); persimmon tannin (PT).

The acquired results enabled to propose a mechanism related to the photocatalysis process. Firstly, the phenomenon of adsorption can be observed, where MB adheres to the surface and pores of the printed structures through physical or chemical interactions. In the second stage, the incidence of UV light on the catalysts promotes the transfer of electrons from the valence band to the conduction band, forming hole-electron pairs (h^+/e^-) (equation 11). In this way, the photo-generated electrons can react with the dissolved oxygen in the solution, forming superoxide radicals ($^{\bullet}O_2^-$) (equation 12), while the holes react with water, producing hydroxyl radicals ($^{\bullet}OH$) (equation 13). The obtained radicals react with the dye through oxidation reactions, promoting the degradation of MB. In addition to the radicals, the photo-generated h^+ can also participate in the degradation of dyes (equation 14) [67,105].

$$MOF/MoS_2 + h\nu \rightarrow MOF/MoS_2\ (h^+/e^-) \qquad Eq.(11)$$

$$MOF/MoS_2\ (e^-) + O_2 \rightarrow {}^{\bullet}O_2^- \qquad Eq.(12)$$

$$MOF/MoS_2\ (h^+) + H_2O \rightarrow {}^{\bullet}OH \qquad Eq.(13)$$

$$MOF/MoS_2\ (h^+) + {}^{\bullet}O_2^- + {}^{\bullet}OH + MB \rightarrow subproducts \qquad Eq.(14)$$

3.3.5 Reusability of aerogels

An important aspect to consider is the materials' reusability in multiple photocatalysis cycles, as illustrated in Fig. 3.10(a), (b), and (c). Reusing MOF/MoS_2 in isolation may not be promising for practical applications. Therefore, a viable solution is the incorporation of MOF/MoS_2 into the hydrogel, which will allow for the reuse of these materials.

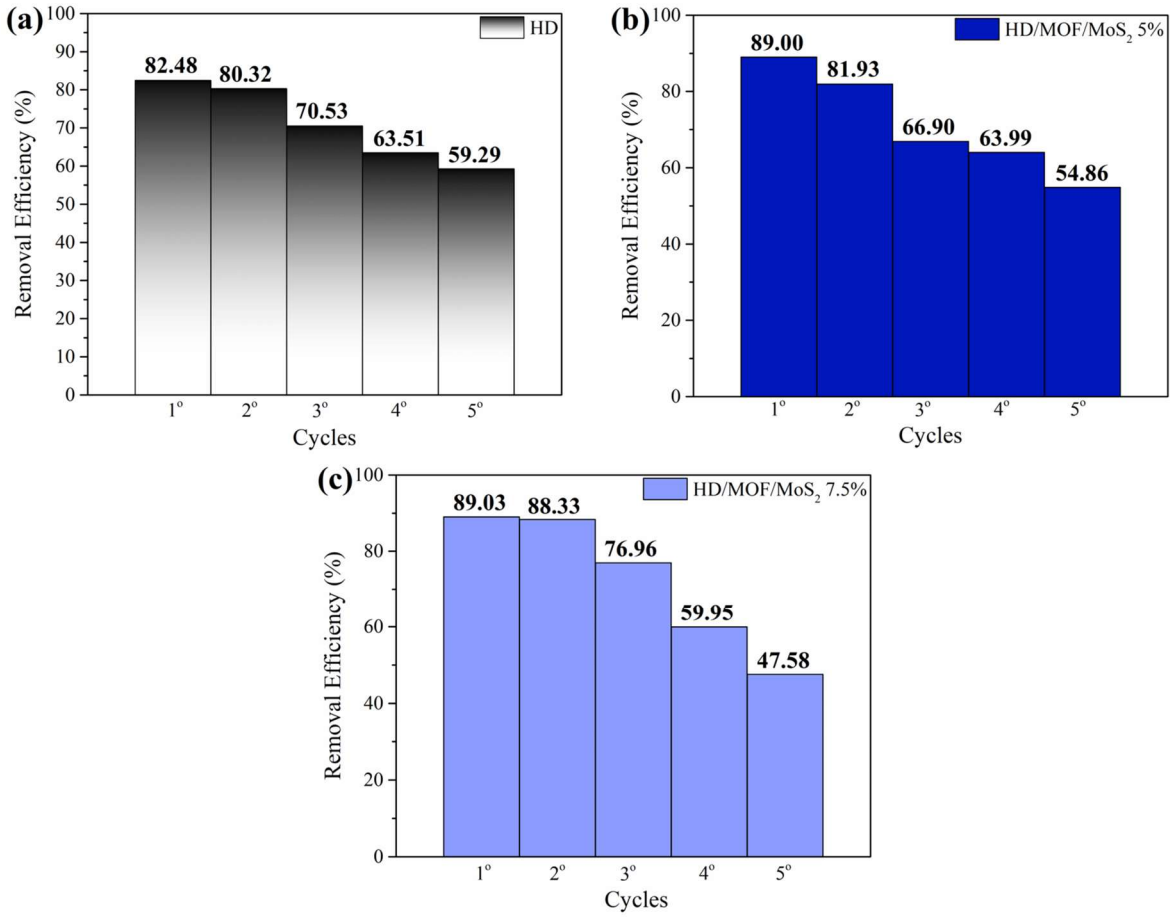

Figure 3.10. Reuse of aerogels. (a) HD; (b) HD/MOF/MoS_2 5 % and (c) HD/MOF/MoS_2 7.5 %. Reprinted with permission from dos Alves et al[103] Copyright 2024, Elsevier.

After each cycle, the materials were washed with ultrapure water and left at room temperature for approximately 24 hours before being used again. After 5 cycles,

there was an efficiency loss of approximately 23 %, 34 %, and 42 % for HD, HD/MOF/MoS_2 5 %, and HD/MOF/MoS_2 7.5 %, respectively. Furthermore, both materials exhibited fracturing after reuse, while HD maintained its structure intact. The presence of MOF/MoS_2 in the aerogel and its interaction with the biopolymers can, in some extent, affect the material's strength, considering that the polymer chains in the hydrogel (HD) connect more strongly. Additionally, MOF/MoS_2 contributed to the greater material's swelling in an aqueous medium.

3.4 Conclusions

Using 3D printing and freeze-drying techniques, we developed a new aerogel based on alginate/carboxymethylcellulose/gelatin incorporated with MOF/MoS_2 for application in dye adsorption and photocatalysis, where methylene blue was used as a model. FTIR, SEM, and EDS analyses confirmed the formation of aerogels, while rheology displayed that the alginate/CMC/gelatin-based hydrogel can flow under deformation, display good shear-thinning behavior, and also allow viscosity recovery of 77 %. Furthermore, the incorporation of MOF/MoS2 at 7.5 wt % improved the rheological properties. The swelling test showed that the presence of MOF/MoS_2 improved the water absorption capacity, making it possible to absorb 1400 % after 70 h. Helium pycnometer analysis showed that the materials have low density and porosity above 80 %. The MB removal results from the adsorption processes showed efficiencies of 16.77 %, 26.66 %, and 95.86 %, for HD, HD/MOF/MoS_2 5 % and HD/MOF/MoS_2 7.5 %, respectively, at different time intervals. However, the results observed in photocatalysis were superior, where the materials showed efficiencies greater than 80 % in a time of 440 min. Finally, the materials were recovered and reused for 5 cycles, to evaluate the stability and catalytic activity. In summary, the produced aerogels are easy to obtain, environmentally friendly and promising candidates for the adsorption and photodegradation of methylene blue dye, as well as they can potentially be explored towards other dyes and environmental contaminants.

4 Chapter 2: MIL88A/MoS_2 heterojunction on PVP/SiO_2 fibers for mitigating environmental pollutants

Ana Laura M. M. Alves[1,2], Rodrigo Schneider[3], Rafaela S. Andre[4], Daniel S. Correa[1]

[1] Nanotechnology National Laboratory for Agriculture (LNNA), Embrapa Instrumentação, 13560-970, São Carlos, SP, Brazil

[2] PPGQ, Department of Chemistry, Center for Exact Sciences and Technology, Federal University of São Carlos (UFSCar), 13565-905, São Carlos, SP, Brazil

[3] Institut Charles Gerhardt Montpellier (ICGM), Université de Montpellier, 00034293, Montpellier, France

[4] THOTECH Soluções & Serviços LTDA, 13500-171, Rio Claro, SP, Brazil

Corresponding author: daniel.correa@embrapa.br

Abstract

The removal of organic contaminants from water sources, such as synthetic dyes, poses a significant challenge due to the inefficiency of conventional treatment methods. Strategies aimed at converting potentially harmful molecules into less toxic species have shown promise and garnered increasing attention. Here we synthesized a functional material based on MOF MIL-88A and MoS_2, aiming to develop an efficient photocatalyst for mitigating environmental contaminants. Photodegradation tests (with methylene blue (MB) dye) using the powder material indicated efficiency greater than 90 % within 120 min. To facilitate the reuse process and prevent the agglomeration of photocatalysts in solution, the MOF/MoS_2 was immobilized on PVP/SiO_2 fibers produced by solution-blow spinning (SBS). The fibers were subjected to thermal treatment to increase the platform surface area and lead self-stable fiber-based support for the MOF/MoS_2 photocatalyst. The MB removal tests using PVP/SiO_2/MOF/MoS_2 fibers demonstrated efficiency above 90 % within 48 h. Additionally, it was observed that the PVP/SiO_2 fibers also contributed to the adsorption and photodegradation processes of the dye, indicating a synergistic effect. The material's stability was evaluated over five reuse cycles, maintaining high efficiency. Furthermore, the nanostructured platform demonstrated versatility by treating other dyes (methyl orange (MO) and rhodamine B (RhB) and antibiotic (tetracycline). These findings highlight the material's potential for environmental pollution remediation, showcasing the fiber's efficiency and stability.

Keywords: Solution-blow spinning, photocatalysis, organic contaminants, PVP/SiO_2 fibers, environmental remediation.

4.1 Introduction

Water resources are essential for sustaining life and play a fundamental role in various industrial sectors. Population growth, along with industrial development, has led to a substantial increase in water demand, as well as in the release of contaminants into the environment. However, the improper disposal of industrial wastes without prior treatment results in serious environmental impacts, compromising the balance of aquatic ecosystems and posing significant risks to human health [196–198]. Among various hazardous contaminants, dyes stand out due to their widespread use across multiple industries, particularly in the textile sector [1]. One of the most widely used dyes is methylene blue (MB), a cationic compound known for its high environmental persistence, toxicity, and potential carcinogenic and mutagenic effects [2]. Due to its high stability, simple photolysis is usually ineffective for MB degradation, thus necessitating the use of more advanced techniques for its efficient removal [4].

Photocatalysis has been extensively studied for contaminants removal, given its capability to convert toxic molecules into harmless, environmentally friendly compounds [1]. In this process, photocatalysts, when irradiated by light, promote the formation of electron-hole pairs (e^-/h^+), resulting from the transition of electrons from the valence band (VB) to the conduction band (CB) [199,200]. These charge carriers can directly react with contaminant molecules, breaking down their structures, and can also interact with H_2O and O_2 molecules, generating highly reactive radicals capable of degrading contaminants [23].

Conventional semiconductors based on metal oxides (such as TiO_2, ZnO, WO_3), have been widely employed in photocatalytic processes due to their advantageous properties including low cost, biocompatibility, and abundance [36,201,202]. Beyond traditional metal oxides, new materials such as metal-organic frameworks (MOFs) have been extensively investigated for photocatalytic applications. MOFs are notable for their high structural versatility, achieved by coordinating metal centers with various organic linkers, which enable tuning their final properties.[48] In MOFs, electron transfer to form e^-/h^+ pairs can occur via two mechanisms: ligand-to-metal charge transfer (LMCT) or metal-to-ligand charge transfer (MLCT), which is triggered by visible light absorption [37,48]. Among the most widely studied MOF classes are MIL, UiO, and ZIF [203]. However, iron-based MOFs (Fe-MOFs) present promising alternatives for the

degradation of organic contaminants due to their high stability, resulting from the strong bonding between Fe centers and organic ligands [55]. In addition to their chemical and aqueous stability, Fe-MOFs are advantageous considering the abundance of their raw materials, environmental compatibility, and cost-effectiveness [37,49].

However, standalone photocatalysts present some bottlenecks, such as the rapid recombination of charge carriers and, in some cases, light absorption limited to the ultraviolet spectrum [105,204]. The formation of heterojunctions in photocatalytic materials is an efficient strategy to overcome these limitations, as it enhances photocatalytic efficiency by combining two materials with complementary band structures.[104] Two-dimensional materials such as MoS_2 [104], g-C_3N_4 [204], and graphene oxide [205] are effective alternatives to yield effective heterojunctions for photocatalysis. In addition to enhancing the density of active sites and improving the efficiency of e^-/h^+ pair separation, they increase the catalyst's surface area [66]. MoS_2, for instance, contributes to the adsorption of cationic dyes on the catalyst surface, facilitating the capture of these pollutants [137]. Studies reported in the literature have investigated the photocatalytic efficiency of heterojunctions between MOFs and MoS_2 in the degradation of contaminants. [66,67,104]

Another drawback of using photocatalysts in aqueous systems is the difficulty of post-recovery and issues related to the aggregation of powdered materials [68,70]. Immobilizing photocatalysts on support materials offers a promising solution to tackle this limitation. Besides, depending on the chosen support, the photocatalytic process can be optimized by considering its interactions with target molecules [68].

In this context, here we report on a novel photocatalyst based on the iron-based MOF (MIL-88A) and MoS_2 deposited on PVP/SiO_2 fibers, as illustrated in Scheme 1. Specifically, MOF and MoS_2 were synthesized by a two-step hydrothermal route at relatively mild conditions, which assures the p-n junction formation. To confirm the photocatalyst MOF/MoS_2 p-n junction and shape morphology, the band-gap were calculated by photoluminescence analysis, and XRD and SEM analysis were performed. Then, the MOF/MoS_2 photocatalyst were assembled by airbrush spray onto partially calcined PVP/SiO_2 fibers produced by solution blow spinning (SBS) technique.

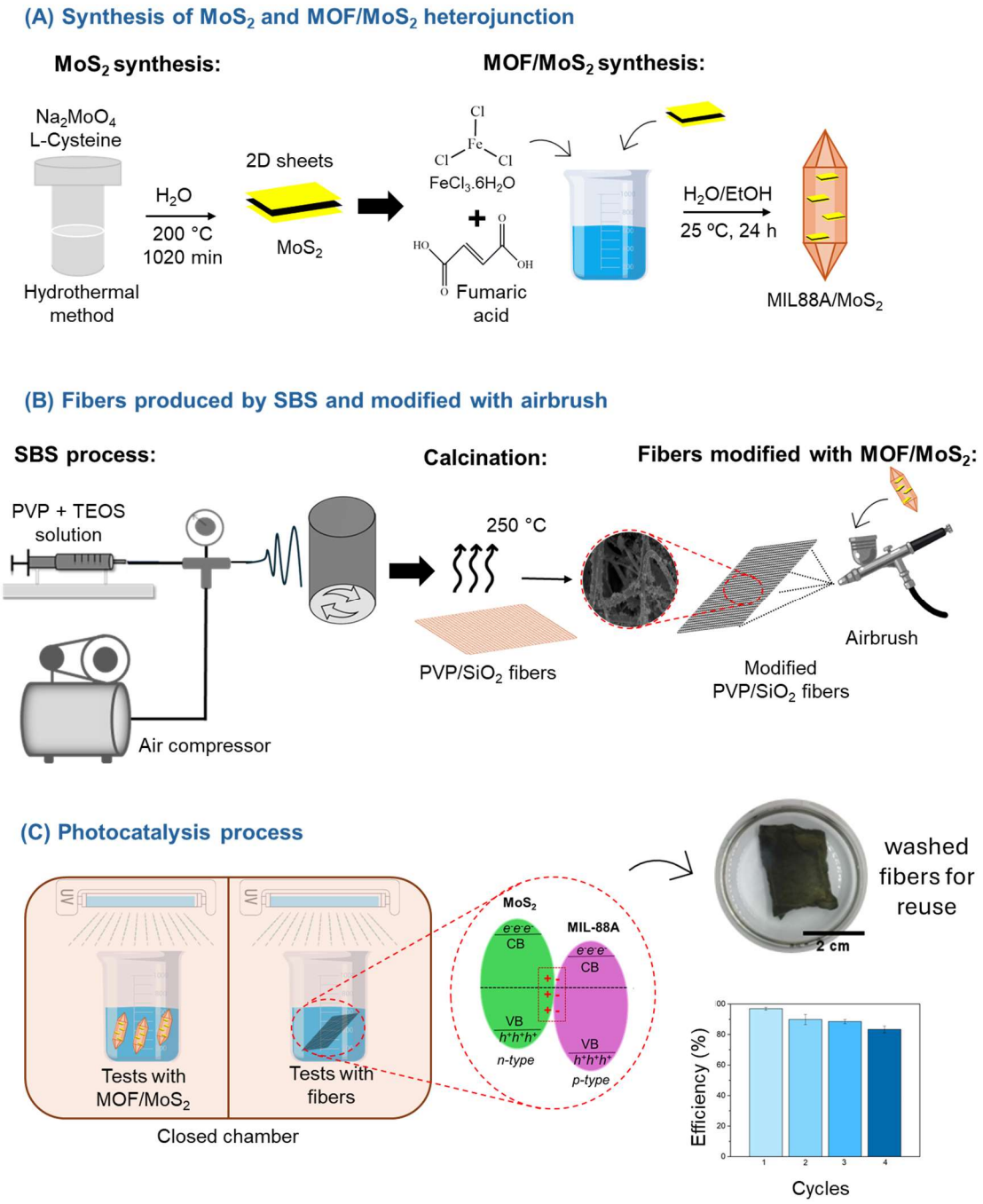

Scheme 2. Schematic illustration of the production of MOF/MoS_2 (A), fabrication and modification PVP/SiO_2 fibers (B) and adsorption/photodegradation of dyes in water (C).

4.2 Experimental

4.2.1 Materials

Polyvinylpyrrolidone (PVP) (M_w = 1,300,000.00 mg/mol), tetraethyl orthosilicate (TEOS, reagent 99 %), iron (III) chloride hexahydrate ($FeCl_3.6H_2O$), methyl orange and tetracycline were purchased from Sigma-Aldrich. Fumaric acid ($C_4H_4O_4$) was acquired from Exôdo Científica (Brazil). L-Cysteine ($C_3H_7NO_2S$) was obtained from Panreac,

while methylene blue was obtained from NEON (Brazil). Rhodamine B and sodium molybdate (Na_2MoO_4) were obtained from Synth (Brazil) and ethanol (≥ 99.5 %) from Exôdo Científica (Brazil).

4.2.2 Synthesis of MOF MIL-88A

The MOF MIL-88A was synthetized based on a methodology previously described in the literature [109]. Firstly, 1.0812 g of $FeCl_3.6H_2O$ was dissolved in 10 mL of ultrapure water and 0.464 g of fumaric acid was dissolved in 10 mL of ethanol, remaining under agitation until completely dissolved. Subsequently, the two solutions were combined and maintained under continuous stirring at room temperature for 24 hours. The orange precipitated power obtained was centrifuged at 8000 rpm for 10 minutes, washed three times with ultrapure water and ethanol, and then dried in a circulating air oven at 40 °C for 48 hours.

4.2.3 Synthesis of MoS_2

MoS_2 was synthesized via a hydrothermal process following the methodology described in [109,137]. Initially, 0.2517 g of L-cysteine and 0.19 g of sodium molybdate were separately dissolved in 15 mL and 10 mL of ultrapure water, respectively. After 5 minutes of stirring, the solutions were combined in a 50 mL Teflon vessel and placed inside a stainless steel reactor. The system was maintained at 200 °C for 1020 minutes with a heating rate of 3 ºC min^{-1}. At the end of the synthesis, the suspension was centrifuged at 8000 rpm for 10 minutes, and the resulting precipitate was washed three times with ultrapure water. Finally, the material was dried in a circulating air oven at 40 °C for 48 hours.

4.2.4 Heterojunction MOF/MoS_2

The heterojunction MOF/MoS_2 was obtained following the procedure described in item 4.2.2, with addition of MoS_2 in different amounts (60 e 100 mg) at the mixture of $FeCl_3.6H_2O$ and fumaric acid, forming the composites denominated MOF/$MoS_2$60 and MOF/$MoS_2$100.

4.2.5 Preparation of PVP/SiO_2 fibers by SBS

To obtain the PVP/SiO_2 fibers, a polyvinylpyrrolidone (PVP) solution was prepared at a concentration of 8 % (w/v) in ethanol. After the polymer was dissolved, a solution of tetraethyl orthosilicate (TEOS) was added, and the mixture was stirred for 2 h at room temperature. The TEOS solution was previously prepared by diluting 1 mL of TEOS into 2 mL of ethanol, followed by the addition of 50 µL of nitric acid to hydrolyze the TEOS and initiate the siloxane polymerization [206].

The PVP/SiO_2 fibers were obtained via solution blow spinning (SBS) technique. The spinning parameters employed were solution flow rate = 10 mL/h, solution ejection pressure = 2 bar, working distance = 40 cm, and collector rotation speed = 180 rpm. Humidity values remained between 30 % and 40 %, with the temperature around 25 °C. Finally, the fibers were partially calcined at 250 °C for 180 min [206].

4.2.6 Functionalization of fibers PVP/SiO_2 with zein, MOF and MOF/MoS_2

For the first functionalization of the PVP/SiO_2 fibers, zein (Z) solutions were prepared at concentrations of 0.1 % (w/v) in a 50/50 (v/v) ethanol/water solution. Approximately 100 mg of PVP/SiO_2 fibers were then immersed in the Z suspensions for 10 min. Subsequently, the PVP/SiO_2/Z fibers underwent a second modification, where they were sprayed on both sides, with suspensions of MOF and MOF/MoS_2, as illustrated in Scheme 1. The suspensions were prepared in 10 mL of ethanol, with MOF and MOF/$MoS_2$100 at a concentration of 2.5 mg/mL. The PVP/SiO_2/Z membrane was positioned 20 cm from the airbrush apparatus, and the pressure used was 4 bar. The resulting fibers were designated as PVP/SiO_2/MOF and PVP/SiO_2/MOF/MoS_2.

4.2.7 Characterizations

The morphology of MOF and MOF/MoS_2 were investigated by field emission gun – scanning electron microscopy (FEG-SEM) using a JEOL JSM-6701, while the fibers were evaluated by scanning electron microscopy (SEM) using a JEOL JSM-6510. The average particle sizes of MOF and MOF/MoS_2 were estimated using the ImageJ software, with 100 measurements. A FEI Tecnai G^2F20 Energy dispersive X-ray spectrometer (EDS) was employed to determine the material's chemical

composition and confirm the presence of components in the MOF/MoS_2. Fourier transform infrared spectroscopy (FTIR) spectra were collected in ATR mode with a Bruker Vertex 70 equipment, in the range of 4000 - 400 cm^{-1}, using 4 cm^{-1} resolution, to determine the vibrational modes of molecules in both, fibers and particulate materials. The Thermogravimetric Analysis (TGA) technique was employed using a SDT650 (TA instrument Thermal Analyzers) equipment, with a ramp rate of 10 °C min^{-1}, temperature range from 25 up to 600 °C under nitrogen atmosphere. The X-ray diffraction (Shimadzu XRD-6000) analysis was carried out in the range of 5 – 70° and scanning speed of 2° min^{-1}. The band gap (E_g) of MOF and MOF/MoS_2 were estimated using the methodology proposed by Wood and Tauc [207], with UV-Vis diffuse reflectance spectra between 200 – 800 nm (Shimadzu UV-2600). For the photoluminescence (PL) analysis, the excitation wavelength used was 280 nm on a Shimadzu spectrophotometer (RF-5301PC).

4.2.8 Photocatalytic performance and adsorption experiments

The photocatalysis experiments were conducted by adding 25 mg of the powder catalyst MOF and MOF/MoS_2 to 50 mL of the MB solutions with a concentration of 25 mg/L, without changing pH. The solutions were stirred in the dark for 30 min, and after this period a 2 mL aliquot was centrifuged at 8000 rpm for 5 min and analyzed in a UV-Vis spectrophotometer (Shimadzu UV-1601PC). Subsequently, the solutions were exposed to radiation from 6 UVC lamps (TUV Philips, 15W) in a closed chamber (Figure S1), and aliquots were analyzed at specific time intervals. The MB degradation was determined by monitoring the maximum absorption wavelength at 665 nm. All experiments were performed at room temperature, in triplicate.

For the experiments conducted with the fibers, approximately 25 mg of the samples were added to 50 mL of MB solutions at concentrations of 5 mg/L and 25 mg/L. The photodegradation analyses were carried out similarly to the procedure described previously for the powdered catalysts; however, the aliquots were not centrifuged for the analysis. The adsorption analyses were performed in the dark, without light irradiation. The degradation efficiency (R_t, %) and the pollutant-adsorbed quantity of at time t (q_t, mg/g) were calculated according to equation 1 and 2 [206], respectively:

$$R_t = \frac{C_0 - C_t}{C_0} \times 100 \quad (1)$$

$$q_t = \frac{(C_0 - C_t) \times V}{m} \quad (2)$$

, where C_0 is the initial dye concentration (mg/L), C_t is the concentration at time t (mg/L), m is the mass of adsorbent (g) and V is the volume of the solution (L).

The adsorption experiment results were evaluated using pseudo-first order and pseudo-second order kinetic models, according to equations 3 and 4 [206], respectively:

$$q_t = q_e(1 - \exp(-k_1 t)) \quad (3)$$

$$q_t = \frac{t}{\left(\frac{1}{k_2 q_e^2}\right) + \left(\frac{t}{q_e}\right)} \quad (4)$$

, where q_e (mg/g) is the amount of dye adsorbed in the equilibrium, k_1, and k_2 are the equilibrium constants of pseudo-first order and pseudo-second order, respectively, and t is the contact time (min).

Other contaminants were used to evaluate the efficiency of the PVP/SiO_2 fibers, including Rhodamine B (RhB), Methyl Orange (MO), and Tetracycline (TC). The concentration of the contaminants was assessed using a UV-Vis spectrophotometer (Shimadzu UV-1601PC) at wavelengths of 555 nm, 467 nm, and 357 nm, respectively.

4.3 Results and discussions

4.3.1 Characterizations

The morphological characteristics of MOF, MOF/MoS_2 are shown in SEM-FEG images displayed in Figure S11. The MOF MIL-88A crystals (Figure S11(a)) exhibit hexagonal shapes [204], with dimensions ranging from 90 to 150 nm and 200 to 300 nm for diameter and length, respectively. The SEM-FEG images of MOF/MoS_2 composites (Figure S11(b-d)) indicates a morphology similar to that observed for the MIL-88A, however, with a more elongated hexagonal structure. This can be associated with the effect caused by the presence of MoS_2 during the MOF nucleation and growth, and the preferred crystalline direction (length). The values obtained for diameters and lengths (Table S1) indicate that the increase of the amount of MoS_2 incorporated to the MOF contributes to the progressive increase in crystal sizes, consistent with previous results reported in the literature [117]. The presence of MoS_2 is perceptible only for

MOF/$MoS_2$100, due to its greater quantity, forming more visible clusters (Figure S11(c) and (d)).

The elemental mapping results obtained for MOF/$MoS_2$100 using EDS spectra (Figure S12) reveal the elements present in the samples, confirming the formation of the heterojunction. The brighter region highlighted in Figure S12 detected the elements Fe and Cl, derived from ferric chloride hexahydrate, both components of the MOF, while the presence of Mo and S represents the MoS_2 distribution, further confirming the formation of the MOF/MoS_2 composite.

The zeta potential analysis (ξ) for MOF, MOF/$MoS_2$60 and MOF/$MoS_2$100 were 23,4 ± 0,52; 1,56 ± 0,22 and -19,1 ± 0,25 mV, respectively, at neutral pH, where ξ ≥ | 30 | represents more stable suspensions[137]. Considering the low stability of the catalysts in aqueous systems, immobilizing them on supports, such as PVP/SiO_2 fibers, is an effective strategy to prevent particle agglomeration. Additionally, the negative values observed for MOF/$MoS_2$100 promote favorable interactions with cationic dyes, like MB. In this context, electrostatic interactions are favored, facilitating the adsorption and subsequent degradation of dyes [137].

The morphological features of PVP/SiO_2 fibers before and after modifications with zein and MOF/MoS_2 were investigated by SEM images shown in Figure 4.1. The PVP/SiO_2 fibers prior to zein functionalization (Figure 4.1(a)) exhibit average diameter of 850 ± 330 nm, with a smooth surface without the presence of beads. PVP/SiO_2/Z fibers show a similar morphology (Figure 4.1(b)), suggesting that a very thin zein layer is formed. The micrographs in Figures 4.1(c–d) show the fibers functionalized with MOF, while Figures 4.1(e–f) show fibers functionalized with MOF/MoS_2. In both cases, the MOFs and MOF/MoS_2 are uniformly distributed along the fibers, indicating that the airbrush spray method was effective in modifying the fibers.

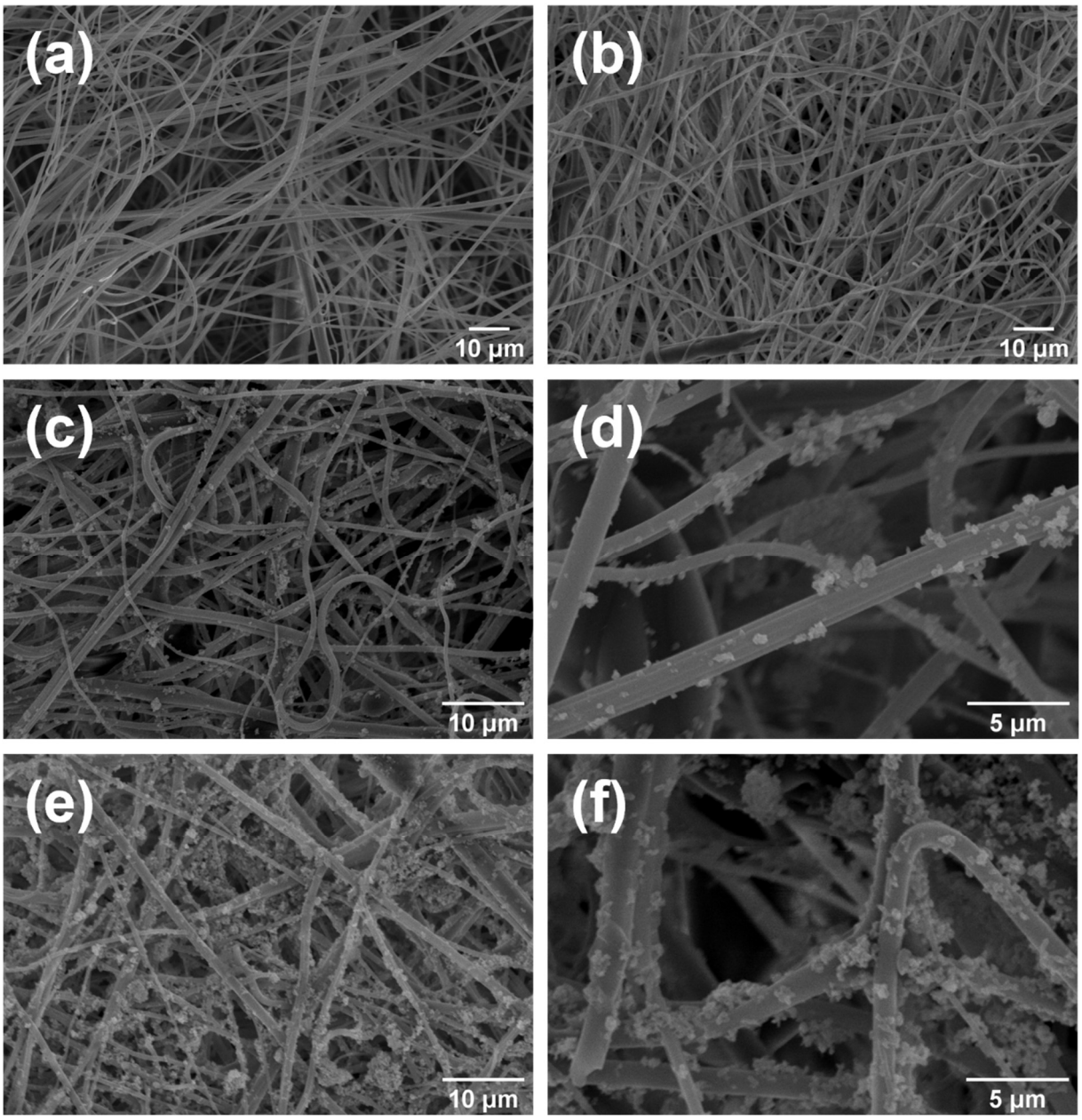

Figure 4.1. SEM images: (a) PVP/SiO_2; (b) PVP/SiO_2/Z; (c) and (d) PVP/SiO_2/MOF; (e) and (f) PVP/SiO_2/MOF/MoS_2. (d) and (f) are a magnified image of (c) and (e), respectively.

The identification of the main functional groups presents on the surface of MOFs, MoS_2, MOF/MoS_2 composites and PVP/SiO_2 fibers were performed using FTIR spectra shown in Figure 4.2 (a) and (b). In the Figure 4.2 (a), for MOF MIL88-A, the bands corresponding to the 1595 and 1395 cm^{-1} regions are attributed to the asymmetric and symmetric stretching of carboxylic groups (-COOH), respectively [208]. The band at 567 cm^{-1} can be associated with the Fe-O stretching originating from the bond formed between the carboxylic groups of the organic ligand fumaric acid and the

metal center [114]. For MoS_2, a weak band at 458 cm^{-1} is observed, attributed to the Mo-S stretching [170] and the band at 1104 cm^{-1} corresponds to the (-SO_3^-) group [209,210]. In the case of the composites, the presence of a broad band in the interval between 3500 – 3000 cm^{-1} can be attributed to the (-OH) arising from adsorbed water molecules on the material's surface. Additionally, characteristic bands from both components are observed at 567 cm^{-1}, corresponding to Fe-O, and the bands1104 cm^{-1} and 458 cm^{-1}, corresponding to -SO_3^- group and Mo-S stretching vibrations, respectively, thus confirming the presence of MOF and MoS_2 [66]. The characteristic bands of MoS_2 related to Mo-S stretching and the -SO_3^- group shifted from 458 to 442 cm^{-1} and from 1104 to 1081 cm^{-1}, respectively, indicating interactions with the MOF.

The FTIR spectra of the PVP/SiO_2 fibers, in Figure 4.2 (b), exhibit a peak at 1649 cm^{-1}, corresponding to the C=O bond characteristic of PVP, and bands at 1056, 955, and 791 cm^{-1}, attributed to the Si-O-Si, Si-OH, and Si-O-Si bonds, respectively, originating from the TEOS partially hydrolyzed into silicic acid and SiO_2 [102,211]. However, it is noted that the band corresponding to Si-O-Si shifts from 1056 to 1068 cm^{-1} after modification with zein, along with the appearance of a band at 1541 cm^{-1} (Figure 4.8 (c)), corresponding to the N-H stretching of the protein from starch. Additional features are observed after the fibers modification with MOF/MoS_2, such as the presence of a shoulder at 1607 cm^{-1} adjacent to the band at 1649 cm^{-1}, and the peak at 1395 cm^{-1}, associated with the stretching of (-COOH) groups characteristic of the MOF. In the region at 567 cm^{-1}, the presence of a band is also observed, characteristic of the Fe-O stretching of the MOF [212].

To determine the crystal structure of MOFs, MoS_2 and MOF/MoS_2 composites, XRD analyzes were performed. From Figure 4.2(d) it is possible to observe characteristic X-ray diffraction peaks at 8.4°, 10.6°, 13.4°, 15.7°, 19.2°, 20.6°, 22.9°, 28.8° and 31.1° which correspond to MOF crystallographic planes as described in the literature [67,212], and broad peaks characteristic of MoS_2 at 10.2º, 33.2º and 57.3º [104]. By incorporating different quantities of MoS_2 into the MOF structure, it is possible to observe changes in intensity and small displacements in some peaks, in addition to the appearance of a well-defined peak at 38.5° in the MOF/MoS_2 composites, indicating the heterojunction between the MOF and MoS_2 [66]. Furthermore, the intensity variation observed can be attributed to changes in size and morphology of the particles during synthesis, and the results obtained with the SEM-FEG images corroborate this hypothesis. Increasing the amount of MoS_2 in the synthesis leads to composites with

longer structures and a more pronounced rod-like morphology (Table S1). Notably, the higher MoS_2 amount in the MOF/MoS_2 composites causes shifts in the MOF X-ray diffraction peaks [213], as well as the emergence of more well-defined peaks.

The XRD patterns for the PVP/SiO_2 fibers, shown in Figure 4.2(e), reveal that the PVP/SiO_2 and PVP/SiO_2/Z fibers exhibit broad peaks at 11.0° and 22.9°, characteristic of amorphous PVP [214]. However, the peak at 22.9° shows greater intensity compared to patterns reported in the literature for pure PVP [102,214], due to the presence of TEOS and the amorphous O-Si-O bonds formed during calcination. The PVP/SiO_2/Z/MOF and PVP/SiO_2/Z/MOF/MoS_2 fibers, on the other hand, display more defined peaks at 10.2° and 13.0°, which are characteristic of the MOF and MOF/MoS_2 incorporated into the fibers [67,104].

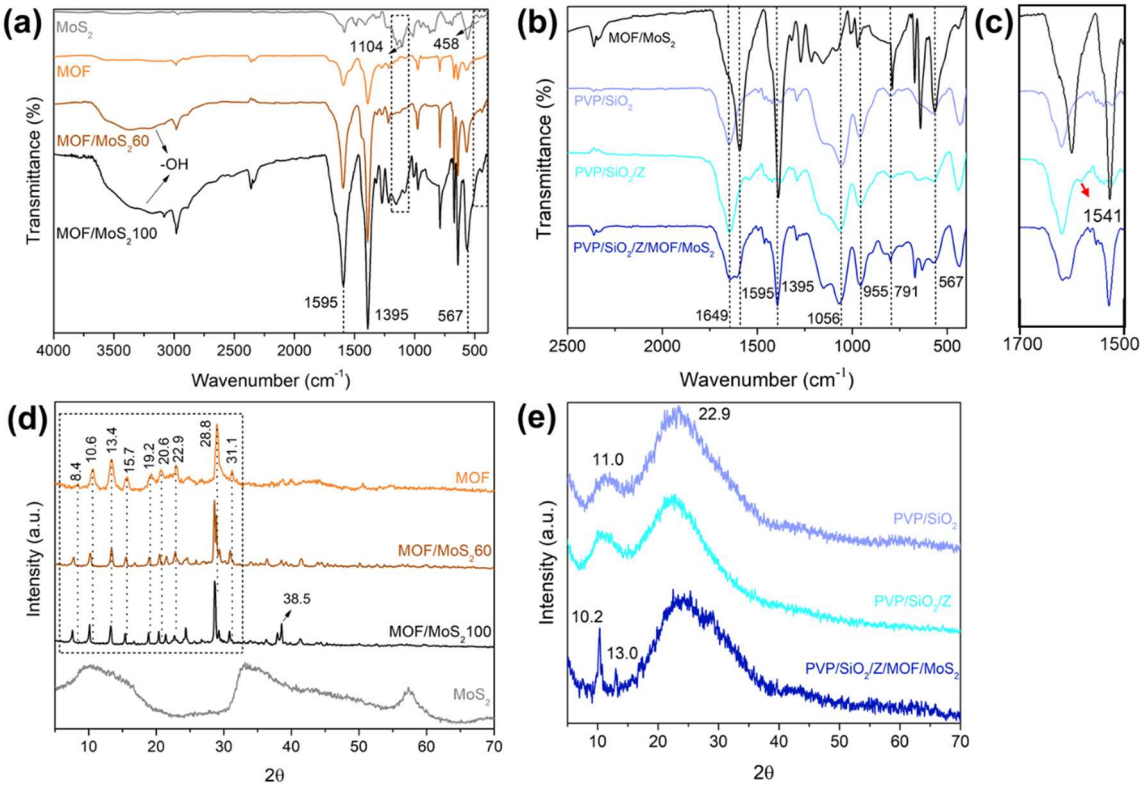

Figure 4.2. (a) and (b) FTIR spectra of MOF, MoS_2, MOF/MoS_2 and PVP/SiO_2 fibers before and after functionalization; (c) zoom of FTIR spectra of PVP/SiO_2 fibers; (d) and (e) DRX of MOF, MoS_2, MOF/MoS_2 and PVP/SiO_2 fibers before and after functionalization.

The thermal stability of MOF, MOF/MoS_2 composites, and PVP/SiO_2 fibers were investigated through TGA analysis, as shown in Figures S13(a) and (b). From Figure S13(a), an initial rapid mass loss is observed below 100 °C for all samples, indicating the loss of residual solvent from the washing process or the decomposition of residual

organic ligands [165]. For the MOF, a second mass loss occurs up to approximately 360 °C, resulting in 26.56 % residual mass. At this stage, the crystalline structure collapses, and the organic ligand degrades [205]. The MOF/MoS_2 composites exhibit degradation profiles similar the MOF; however, a higher percentage of residue is noted, with 28.75 % and 40.17 % for MOF/$MoS_2$60 and MOF/$MoS_2$100, respectively, confirming the presence of MoS_2.

The TGA curves for the fibers (Figure S13(b)) also show a first stage of mass loss below 100 °C, due to the loss of adsorbed water. The second stage of mass loss continues until approximately 480 °C, indicating the degradation of the polymeric chain corresponding to PVP [215]. The residual mass observed for PVP/SiO_2 and PVP/SiO_2/Z fibers is attributed to the silica and carbon phases, resulting from the calcination process. The PVP/SiO_2/MOF and PVP/SiO_2/MOF/MoS_2 fibers exhibited higher residual mass, due to the presence of MOF and MOF/MoS_2 immobilized on the fibers [216].

The generation of electron-hole pairs and their recombination rate are critical factors in the photocatalytic degradation process, directly influencing photocatalytic efficiency [67]. Photoluminescence (PL) spectra can be used to assess the effectiveness of charge carrier separation by analyzing the intensity of the PL signals. As shown in Figure S14, the MOF exhibits a higher PL intensity compared to MOF/$MoS_2$60 and MOF/$MoS_2$100, indicating that the heterojunctions achieved more efficient charge carrier separation, and thus, a lower recombination rate [117,208,217].

To estimate the bandgap energy (E_g) of the catalysts, diffuse reflectance spectroscopy (UV-Vis DRS) analyses were conducted. The reflectance spectra obtained was converted into absorbance spectra using the Kubelka-Munk function. From these spectra, the E_g was calculated using the Tauc equation (5) [218]:

$$\alpha h\nu = A(h\nu - E_g)^{n/2} \quad (5)$$

, where α, h, ν, E_g and A are the absorption coefficient, Planck's constant, light frequency, bandgap energy, and a constant, respectively. The value of n is associated with the type of optical transition in the semiconductor, where n = 4 represents direct transitions and n = 1 represents indirect transitions. The E_g value found for the MOF, 2.71 eV, is consistent with reports in the literature [66,219,220]. It is noted that the addition of MoS_2 leads to a change in light absorption. The E_g values obtained for MOF/$MoS_2$60,

and MOF/$MoS_2$100 were 2.87 and 2.97, respectively (Figure S15). The E_g value for PVP/SiO_2 fibers was also determined from the reflectance spectrum. Based on the Tauc plot shown in Figure S16, the PVP/SiO_2 fibers exhibited an E_g value of 4.33 eV, similar to that reported in the literature [103]. However, the E_g values for PVP/SiO_2 fibers may vary, depending on the percentage of polymer calcined and the presence of the SiO_2 nanostructures formed [103,215].

4.3.2 Adsorption and photodegradation performance

The photocatalytic activity of the MOFs and MOF/MoS_2 composites are presented in Figure 4.3. Initially, the catalysts were added to MB solutions at a concentration of 25 mg/L and kept in the dark for 30 min to allow MB adsorption on their surfaces. Subsequently, the samples were irradiated with UV light, and aliquots were collected at specific time intervals for analysis. Figure 4.3(a) illustrates that, during the initial adsorption period, the MOF does not significantly interact with MB, whereas the MOF/MoS_2 composite demonstrates higher adsorption efficiency. These results indicate that the incorporation of MoS_2 into the MOF enhances the catalyst's interaction with the dye, consistent with the zeta potential values. After the adsorption period, the samples remained under light irradiation for 100 min, yielding efficiency values of 45 %, 61 %, and 95 % for the MOF, MOF/$MoS_2$60, and MOF/$MoS_2$100, respectively. Figure 4.3(c) shows the MB solution at its initial concentration and after the adsorption/photodegradation process, illustrating its decolorization process. The degradation capacity of MB under UV light irradiation in the absence of catalysts was also evaluated to assess photolysis processes. Based on the results shown in Figure S17, MB solutions at a concentration of 25 mg/L exhibited degradation rates below 1% after 100 minutes of light irradiation, indicating the inefficiency of photolysis compared to the catalysts.

The degradation kinetics were described using the Langmuir-Hinshelwood (L-H) model, commonly applied for heterogeneous photodegradation systems, according to equation 6 [16]:

$$\frac{1}{r_0} = \frac{1}{k} + \frac{1}{kKC_0} \tag{6}$$

, where r_0 is the reaction rate (mg/L min^{-1}), k is the reaction rate constant (mg/L min^{-1}), K is the adsorption coefficient (L/mg), and C_0 is the initial dye concentration (mg/L).

However, the equation can be simplified, and the photodegradation rate can be determined using the linear expression shown in equation 7 [105]:

$$ln\left(\frac{C_0}{C_t}\right) = kt \quad (7)$$

, where C_0 is the initial dye concentration (mg/L), C_t is the dye concentration at time (min) and k is the apparent rate constant of pseudo-first-order kinetics (min^{-1}).

According to the results in Figure 4.3(b), MOF/$MoS_2$100 exhibited the highest k value (0.0214 min^{-1}), demonstrating the efficiency of the MOF/MoS_2 junction for MB removal through a combined adsorption/photodegradation process. However, the MOF alone showed a higher k value (0.0068 min^{-1}) compared to MOF/$MoS_2$60 (0.0034 min^{-1}), indicating that the MOF alone possesses good photocatalytic activity, while MoS_2 provides enhanced affinity for MB, aiding in the adsorption step [67].

Reuse tests were conducted with the catalysts, which, after each cycle, were centrifuged and washed multiple times with water and ethanol. After the third cycle, the MB removal efficiency dropped to 31 %, which may be attributed to the challenge of recovering the powdered catalyst during the washing process. To mitigate this limitation, the catalysts were immobilized, facilitating the washing and reuse process [221].

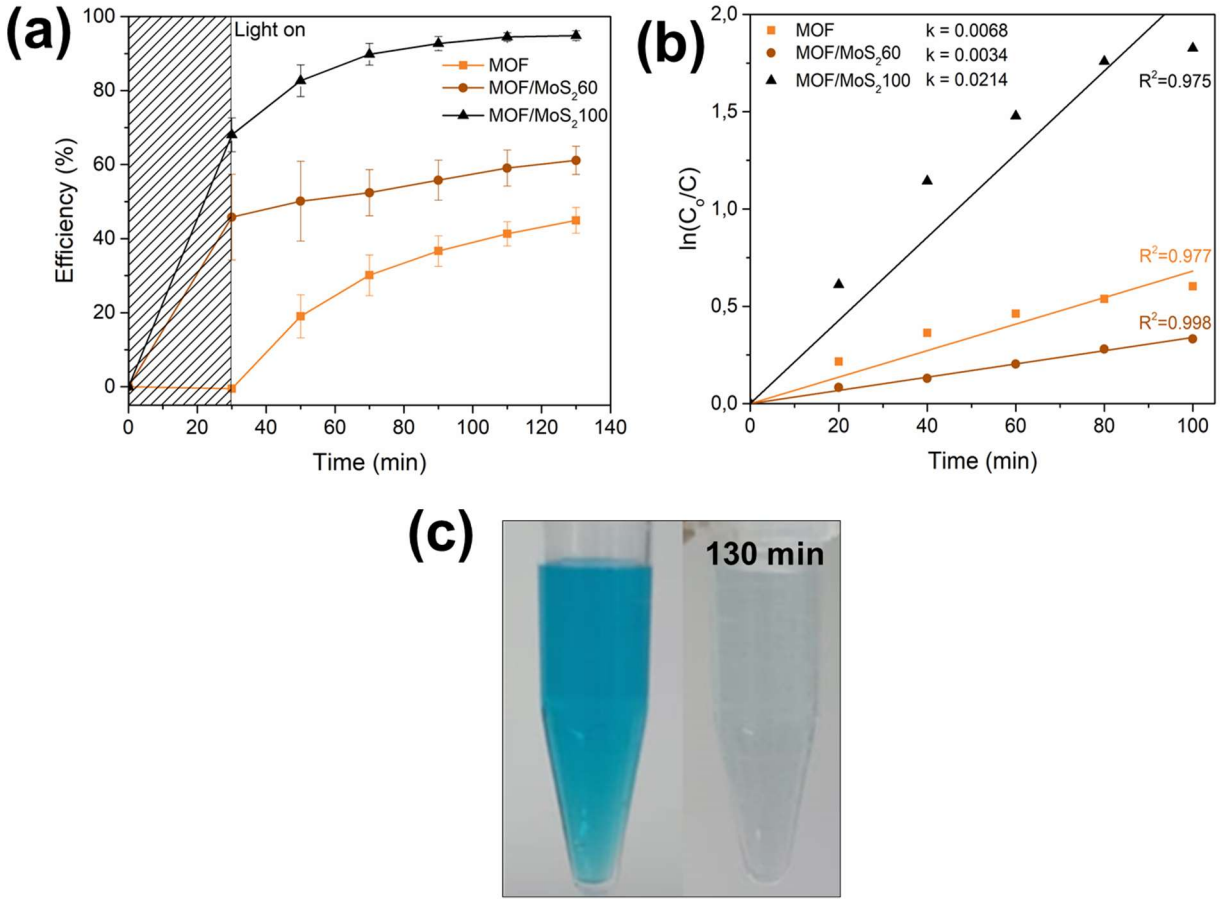

Figure 4.3. (a) MB adsorption/photodegradation analysis (25 mg/L) using MOF, MOF/$MoS_2$60, and MOF/$MoS_2$100 catalysts; (b) MB degradation kinetics; and (c) illustration of MB degradation and removal.

The efficiency and feasibility of the airbrush technique for self-standing immobilization of the MOF/MoS_2 photocatalyst onto the surface of blown-spun PVP/SiO_2 fibers were investigated by selecting the MOF/$MoS_2$100 catalyst. Samples of approximately 25 mg PVP/SiO_2/MOF/$MoS_2$100 were then immersed in MB solutions at a concentration of 5 mg/L. The adsorption/photodegradation results are shown in Figure 4.4(a). Adsorption/photodegradation tests were conducted as previously described, with the fibers kept in the dark for 30 min before being irradiated with UV light. After 6.5 h, the MB removal efficiencies for PVP/SiO_2, PVP/SiO_2/Z/MOF, and PVP/SiO_2/Z/MOF/MoS_2 fibers were 88 %, 49 %, and 77 %, respectively.

Based on these results, PVP/SiO_2 and PVP/SiO_2/MOF/MoS_2 fibers were selected for additional tests using MB solutions at a concentration of 25 mg/L, with results presented in Figure 4.4(b). MB removal efficiency was assessed over a period of 48 h, yielding efficiencies of 84 % and 98 % for PVP/SiO_2 and PVP/SiO_2/MOF/MoS_2 fibers, respectively. Photolysis analyses were conducted at time intervals of 24 h and

48 h, with degradation rates of 11% and 23%, respectively, confirming the efficiency of the proposed materials as catalysts. Adsorption tests without light irradiation were also conducted, and after 48 h, PVP/SiO_2 and PVP/SiO_2/MOF/MoS_2 fibers demonstrated efficiencies of 42 % and 47 %, respectively. Based on the adsorption and adsorption/photodegradation results, it was observed that the PVP/SiO_2 fibers exhibited an efficiency increase from 42% to 84%, indicating that the fibers themselves contribute to the MB degradation processes [100]. Thus, the fibers not only serve as support for catalyst immobilization, but also act synergistically with MOF/MoS_2 in dye degradation. Additionally, a faster interaction between MB molecules and PVP/SiO_2 fibers was observed in the initial hours compared to functionalized fibers. This is likely due to the high surface area of PVP/SiO_2 fibers, which enhances MB adsorption, while functionalized fibers may have a reduced surface area due to the immobilization of MOF/MoS_2 across their surface [6,100].

The kinetic assays for both adsorption and adsorption/photodegradation processes are presented in Figure 4.4(c) and (d). For the adsorption/photodegradation kinetics (Figure 4.4(c)), the PVP/SiO_2/MOF/MoS_2 fibers (k = 0.0882) exhibited a higher degradation rate constant compared to PVP/SiO_2 (k = 0.0348), confirming that the obtained composite offers superior photocatalytic performance [220]. On the other hand, the adsorption kinetics (Figure 4.4(d)) provides insight into and quantifies the mass transfer process [7]. For this purpose, both pseudo-first order and pseudo-second-order models were evaluated, with the obtained parameters presented in Table 4.1. For both PVP/SiO_2 and PVP/SiO_2/MOF/MoS_2 fibers, the R^2 values were higher for the pseudo-second-order model (R^2 = 0.997 e R^2 = 0.895, respectively), suggesting that the interactions between MB molecules and the fibers occur through chemisorption [222].

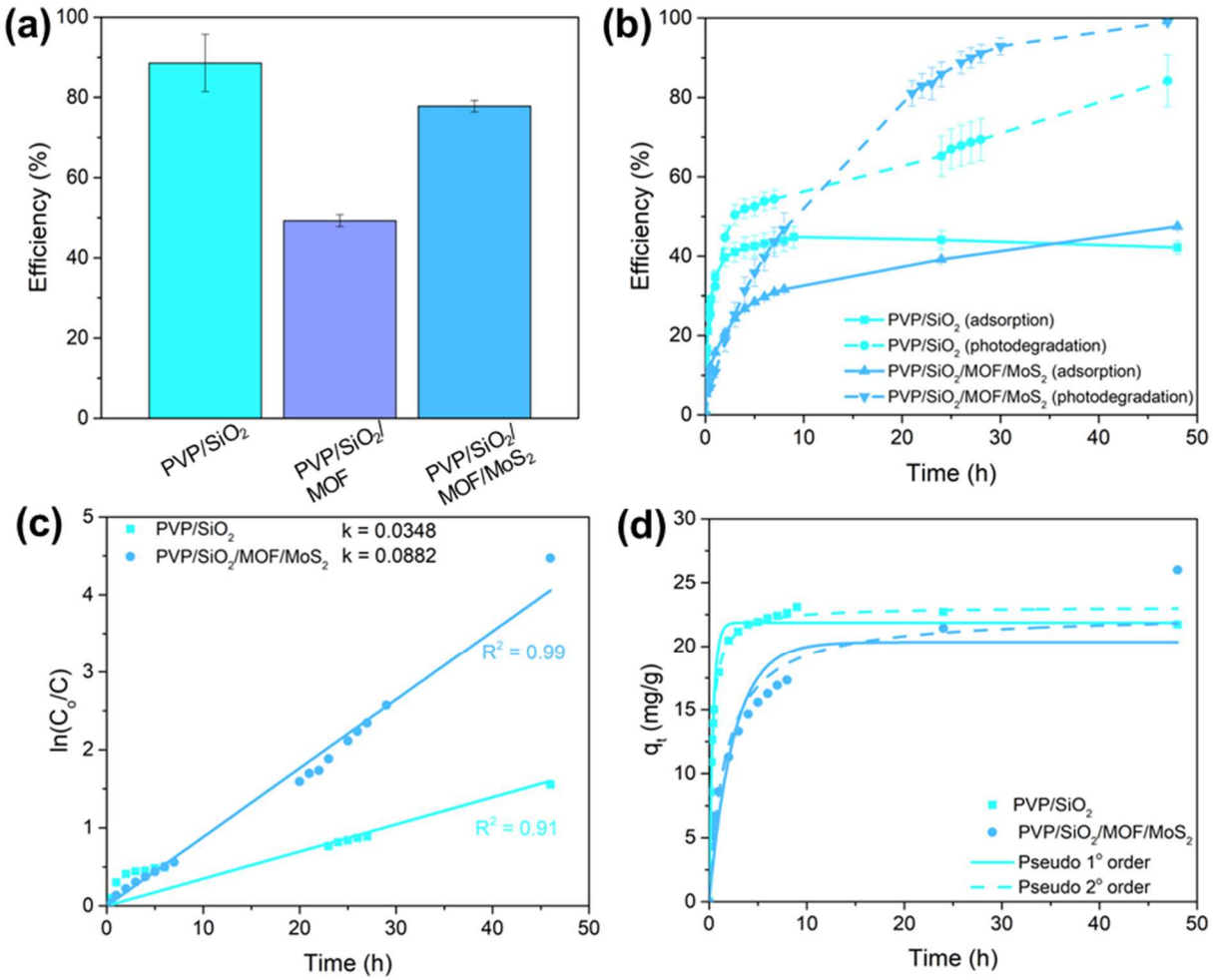

Figure 4.4. (a) Adsorption/photodegradation analysis of MB (5 mg/L) for functionalized and non-functionalized fibers after 7 hours; (b) adsorption and adsorption/photodegradation analysis of MB (25 mg/L) for PVP/SiO_2 and $PVP/SiO_2/MOF/MoS_2$ fibers after 48 hours; (c) MB degradation kinetics and (d) MB adsorption kinetics for PVP/SiO_2 and $PVP/SiO_2/MOF/MoS_2$ fibers.

Table 4.1. Kinetic parameters obtained from adsorption models for PVP/SiO_2 and $PVP/SiO_2/MOF/MoS_2$ fibers at 25 mg/L MB solutions.

Sample	Experimental	Pseudo 1° order			Pseudo 2° order		
	Q_{exp} (mg/g)	k_1 (min^{-1})	Q_{teo} (mg/g)	R^2	k_2 (g mg^{-1} min^{-1})	Q_{teo} (mg/g)	R^2
PVP/SiO_2	21.73	0.0418	21.86	0.983	742.88	23.09	0.997
$PVP/SiO_2/MOF/MoS_2$	25.99	0.0032	26.26	0.860	111.36	28.53	0.895

4.3.3 Study of the Adsorption and Photodegradation Mechanism for MB

The proposed integration between the MIL-88A MOF and MoS_2 for enhancing photocatalytic activity exploits the formation of a p-n heterojunction, where MIL-88A functions as a p-type semiconductor and MoS_2 as an n-type semiconductor [66]. Semiconductors with a low energy bandgap (Eg), such as MoS_2, act as reduction agents, while those semiconductors with high Eg are characteristic of oxidizing agents [223]. In this context, the representative schematic of the proposed heterojunction is illustrated in Figure 4.5.

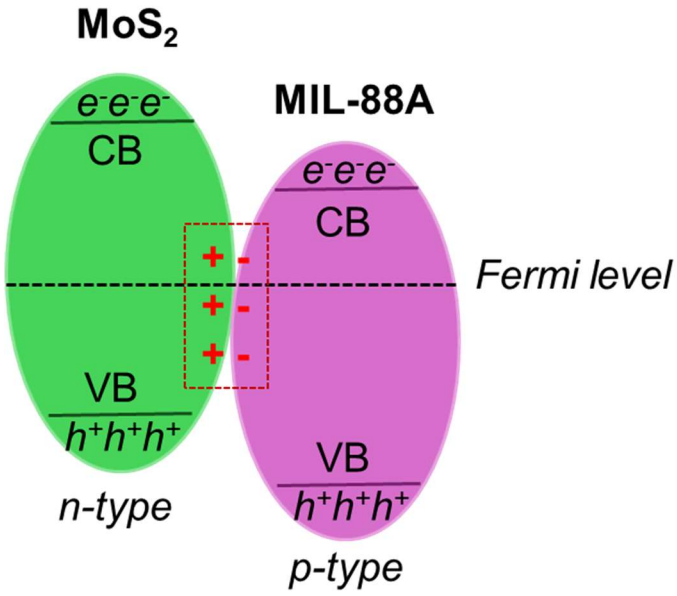

Figure 4.5. Proposed heterojunction for MOF/MoS_2.

Before the formation of the junction, the Fermi level of MoS_2 is located near the conduction band, while the Fermi level of MIL-88A is situated close to the valence band. Upon contact between the two structures, a natural migration of charge carriers occurs, resulting in the equalization of the Fermi levels and the formation of an internal electric field. This electric field not only facilitates the transfer of charge carriers but also enhances photocatalytic activity by inhibiting the rapid recombination of electron-hole pairs (e^-/h^+) [62]. Based on the proposed heterojunction model, the photocatalytic degradation mechanism can be outlined in several steps, which include: (a) adsorption of dye molecules; (b) generation of e^-/h^+ pairs and radicals under light irradiation; and

(c) interaction of the dye molecules with the radicals, leading to the degradation of the molecules [24,223].

In order to identify the active species involved in the photodegradation process of the functionalized PVP/SiO_2/MOF/MoS_2 fibers, trapping tests were conducted [33,66,104]. For this, ethylenediamine tetraacetic acid disodium salt (EDTA- 2Na, 2.5 mmol L^{-1}) was used to suppress holes (h^+), isopropanol (IPA, 2.5 mmol L^{-1}) to suppress hydroxyl radicals ($^{\bullet}OH$), hydrogen peroxide (H_2O_2. 2.5 mmol L^{-1}) to suppress electrons (e^-) and ascorbic acid (AA, 2.5 mmol L^{-1}) to suppress superoxide radicals ($^{\bullet}O_2^-$). Based on the results (Figure 4.6(a)), the addition of IPA led to significant changes in dye degradation, indicating that $^{\bullet}OH$ radicals play a major role in MB degradation. For PVP/SiO_2 fibers (Figure 4.6(b)), the addition of IPA and AA reduced the degradation efficiency, indicating that, along with $^{\bullet}OH$ radicals, $^{\bullet}O_2^-$ radicals are also predominant active species in the photodegradation process and may have an even greater influence. The generation of these radicals can occur as confined water molecules in the holes are converted into $^{\bullet}OH$ radicals, while oxygen molecules, upon interacting with photogenerated electrons, can also form radicals. Additionally, the introduction of H_2O_2 was observed to enhance degradation, likely due to an increased production of $^{\bullet}OH$ radicals. Therefore, the degradation steps can be described by equations (8–14):

$$MOF/MoS_2 \xrightarrow{h\nu} (h^+ + e^-)MOF/MoS_2 \quad (8)$$

$$H_2O + h^+ \rightarrow {}^{\bullet}OH \quad (9)$$

$$O_2 + e^- \rightarrow {}^{\bullet}O_2^- \quad (10)$$

$$^{\bullet}O_2^- + H^+ \rightarrow {}^{\bullet}OH \quad (11)$$

$$^{\bullet}OH + {}^{\bullet}OH \rightarrow H_2O_2 \quad (12)$$

$$H_2O_2 + e^- + H^+ \rightarrow {}^{\bullet}OH + H_2O \quad (13)$$

$$^{\bullet}OH + {}^{\bullet}O_2^- + h^+ + e^- + MB \rightarrow H_2O + CO_2 + \text{Inorganic salts} \quad (14)$$

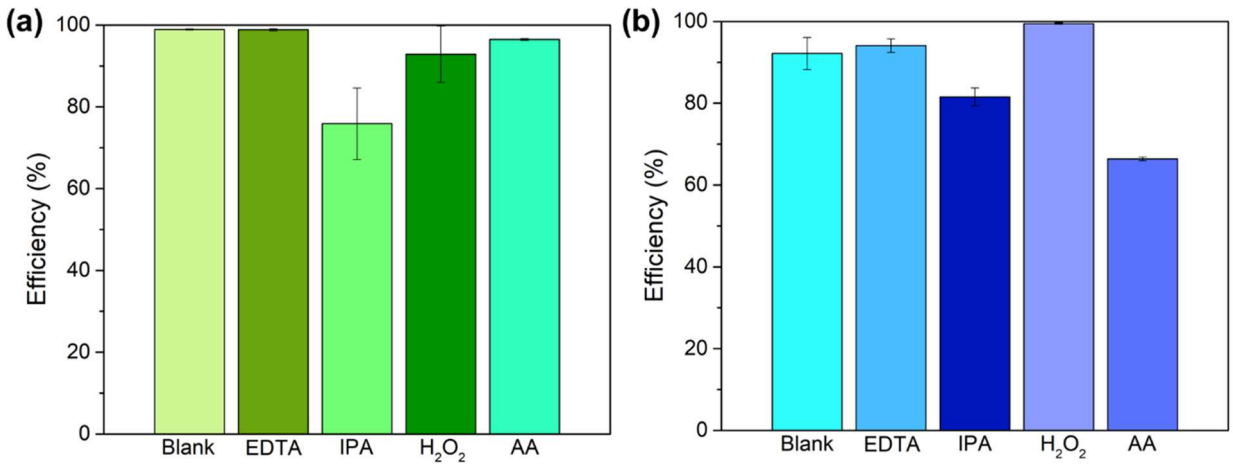

Figure 4.6. (a) Effect of different scavengers on MB degradation using (a) PVP/SiO_2 and (b) PVP/SiO_2/ MOF/MoS_2 fibers after 48 hours.

The PVP/SiO_2 fibers also contribute to the photocatalytic degradation process by promoting charge transitions that result in the formation of radicals, as well as by assisting in the adsorption of MB molecules due to their high surface area. To better understand how the interactions between MB and the fibers occurred, FTIR analyses of the fibers after the adsorption process were performed (Figure S18). The spectra show a reduction in the band intensity at 1649 cm^{-1}, which is associated with the C=O stretching of PVP, along with the emergence of a band at 1605 cm^{-1}, attributed to the vibration of C=C bonds in the aromatic rings present in MB [224]. Additionally, bands in the regions of 1068 cm^{-1} and 955 cm^{-1} also exhibited a decrease in intensity. Thus, the observed changes suggest π-π interactions or the formation of hydrogen bonds between the fibers and MB [206].

4.3.4 Reusability of PVP/SiO_2/MOF/MoS_2 fibers

Reusability tests for the PVP/SiO_2/MOF/MoS_2 fibers were conducted to evaluate the stability of the proposed material. After each use, the fibers were washed with a pH=2 solution and subsequently rinsed with water to remove any excess acidic solution. Following the washing process, the fibers were immersed in new MB solutions for another cycle of photocatalytic degradation. As shown in the results presented in Figure 4.7, after four cycles of reuse, the fibers maintained an efficiency exceeding 80 %, demonstrating their excellent stability.

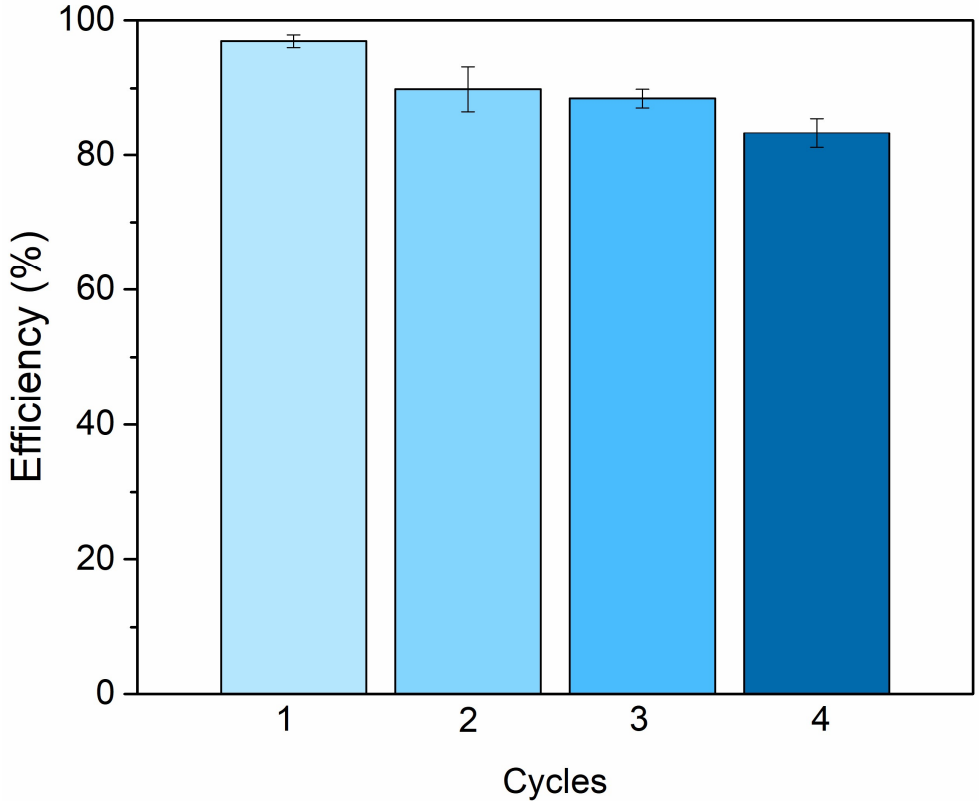

Figure4.7. Reusability analysis of PVP/SiO_2/MOF/MoS_2 fibers in a 25 mg/L MB solution over a 48 h period.

4.3.5 Photodegradation performance of PVP/SiO_2 and PVP/SiO_2/MOF/MoS_2 fibers for other contaminants

The photocatalytic efficiency of PVP/SiO_2 and PVP/SiO_2/MOF/MoS_2 fibers were evaluated for other types of dyes, in addition to the antibiotic tetracycline (TC). All solutions were prepared at a concentration of 5 mg/L. In Figure 4.8(a), the analyses were conducted over a time interval of 7 h, with TC being the only compound subjected to simple photolysis due to its photosensitivity [225]. The results indicate that, for TC, the efficiency of the PVP/SiO_2 fiber achieved by simple photolysis is notable, while the PVP/SiO_2/MOF/MoS_2 fibers exhibited a superior efficiency, approaching 80 %. For the cationic dye rhodamine B (RhB) and the anionic dye methyl orange (MO), both fibers, PVP/SiO_2 and PVP/SiO_2/MOF/MoS_2, demonstrated similar efficiency values. Subsequently, the analyses were extended to a period of 24 h, and the results obtained are presented in Figure 4.8(b). It was observed that for tetracycline, the use of fibers is unnecessary, as light irradiation alone proves to be efficient in its degradation. For RhB, both fibers showed good results, with efficiencies exceeding 90 %. However, for MO, the PVP/SiO_2 fibers exhibited greater efficiency.

Similar to MB, the dye RhB is cationic, which promotes effective interactions with the analyzed fibers. On the other hand, although MO is an anionic dye, the photocatalytic process achieved satisfactory degradation rates. In this context, despite the interactions between the fibers and MO did not significantly favor adsorption, the photocatalytic process proved effective in degrading the dye, albeit at a slower rate compared to the other dyes evaluated [226,227]. More efficient interactions between the fibers and MO could be observed in acidic media, where the protonation of functional groups on the fibers could enhance interactions with MO [227]

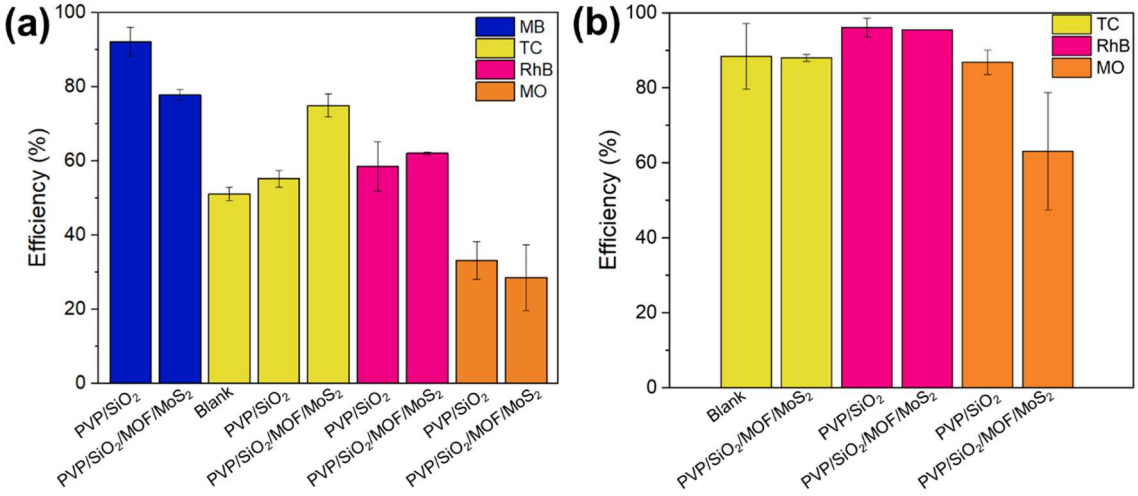

Figure 4.8. Evaluation of the efficiency of PVP/SiO_2 and PVP/SiO_2/MOF/MoS_2 fibers in the photodegradation of the dyes MB, RhB, and MO, as well as the antibiotic TC, at time intervals of (a) 7 h and (b) 24 h and concentrations of 5 mg/L.

The photocatalytic degradation efficiencies for the dyes MB, RhB and MO using other materials reported in the literature are presented in Table 4.2. The results obtained in the present study, when compared to previous works, demonstrate significant potential for photocatalytic applications, considering the efficiency of the materials produced, while also highlighting the stability of the functionalized fibers in reuse processes for MB degradation. Furthermore, it is noteworthy that no oxidizing agents, such as H_2O_2, were employed to enhance the process, making the process simpler.

Table 4.2. Comparison of photocatalytic processes for different dyes reported in the literature.

Catalysts	Dye	Concentration of dye, efficiency, irradiation time and reuse	References
TiO_2/graphene oxide on Polyacrylonitrile/β-cyclodextrin	MB	10 ppm, ~93 %, 5 h, efficiency of 80 % after 3 cycles	228
Zr-doped TiO_2 ceramic fibers	MB	10 mg/L, 94.3 %, 5 h	229
TiO_2/Carbon	MB	20 mg/L, 85.7 %, 6 h, constant performance after 3 cycles	230
g-C_3N_4	MB	20 mg/L, 8.29 %, without H_2O_2, 180 min 20 mg/L, 99.03 %, with H_2O_2, 90 min, stability in 5 reuse cycles	188
Mxene/g-C_3N_4	MB	10 mg/L, 69.4 %, 3 h	231
Cellulose/GO/TiO_2 hydrogel	MB	10 mg/L, 96 %, 120 min	232
TiO_2	RhB	0.7 – 3.4 mg/L, 96 %, 3 h	233
TiO_2 /g-C_3N_4	RhB	10 mg/L, 80 %, 300 min	234
MoS_2/g-C_3N_4	MO	20 mg/L, ~60%, 5 h	235
C/ZnO	MO	10 mg/L, 87.8 %, 300 min	236
MOF/MoS_2	MB	25 mg/L, 95 %, 120 min	This study
PVP/SiO_2	MB RhB MO	5 mg/L, ~90 %, 7 h 5 mg/L, ~60 %, 7 h and ~96 %, 24 h 5 mg/L, ~33 %, 7 h and 86 %, 24 h	This study
PVP/SiO_2/MOF/MoS_2	MB RhB MO	25 mg/L, ~98 %, 48 h, efficiency >80 % after 4 cycles 5 mg/L, ~60 %, 7 h and ~95 %, 24 h 5 mg/L, ~28 %, 7 h and ~62 %, 24 h	This study

g-C_3N_4 = Graphitic carbon nitride, GO = Graphene oxide.

4.4 Conclusions

A MOF/MoS_2 heterojunction was synthesized with different amounts of MoS_2 to evaluate the evolution of efficiency in the degradation of the MB dye. The results obtained for the composition containing 100 mg of MoS_2 showed an efficiency exceeding 90 % in 120 min, making it the selected material for subsequent stages. The confirmation of the heterojunction formation between MOF and MoS_2 was fully investigated through SEM, FTIR, EDS, and PL. Subsequently, the MOF/MoS_2 photocatalysts were immobilized in PVP/SiO_2 fibers, demonstrating an efficiency greater than 90 % after 48 h of analysis. The primary objective of immobilization was

to facilitate the recovery and reuse of the photocatalysts; however, it was observed that the fibers, in addition to serving as a support, synergistically contributed to the adsorption and photodegradation processes alongside the MOF/MoS_2. Regarding stability, the fibers maintained a removal efficiency greater than 80 % after five reuse cycles. In addition to MB, the dyes RhB and MO were also efficiently removed by the fibers, suggesting the potential of the PVP/SiO_2/MOF/MoS_2 as a strategy to mitigate environmental pollutants.

5. FINAL REMARKS AND FUTURE PERSPECTIVES

This thesis demonstrated the feasibility of synthesizing the MOF MIL-88A/MoS_2 heterojunction, resulting in a highly efficient for the removal of methylene blue (MB) dye, primarily through adsorption and photodegradation processes. The main objective of forming the heterojunction is to enhance the catalytic properties of the system compared to the individual materials, owing to the greater stability of h^+/e^- pairs, as evidenced by photoluminescence (PL) analyses for the MOF/MoS_2. The formation of the heterojunction was confirmed through morphological and spectroscopic characterizations, including scanning electron microscopy (SEM) imaging, Fourier-transform infrared spectroscopy (FTIR), and energy-dispersive spectroscopy (EDS).

In addition to the synthesis and characterization of the MOF/MoS_2 particulate material, its incorporation into aerogels obtained via 3D printing and PVP/SiO_2 fibers produced by *solution blow spinning* (SBS) was explored, aiming to facilitate its recovery and reuse over multiple cycles. The advantages of using aerogels in water contaminant removal applications include their high porosity, such as the aerogels obtained in this study (porosity > 80%), as well as their swelling ability and high water absorption capacity, while maintaining their original structure.

Meanwhile, the PVP/SiO_2 fibers proved to be an efficient support for the MOF/MoS_2 catalyst, in addition to contributing synergistically to the adsorption and photodegradation processes.

Based on the results obtained in this study, the novel developed platforms demonstrated significant potential for pollutant removal and degradation, opening perspectives for the enhancement of multifunctional material synthesis applicable to a wide range of contaminants.

Thus, future research perspectives include the development and exploration of new synthesis methods for aerogels, aiming to obtain highly porous structures with large surface areas, thereby maximizing their efficiency in applications related to contaminant removal. Additionally, the incorporation of new polymers and nanomaterials into aerogel compositions will be investigated, leading to the production of polymeric or composite aerogels with enhanced properties.

REFERENCES

1. Hasanpour, M. & Hatami, M. Photocatalytic performance of aerogels for organic dyes removal from wastewaters: Review study. *Journal of Molecular Liquids* vol. 309 Preprint at https://doi.org/10.1016/j.molliq.2020.113094 (2020).

2. Fito, J. *et al*. Adsorption of methylene blue from textile industrial wastewater using activated carbon developed from Rumex abyssinicus plant. *Sci Rep* **13**, (2023).

3. Sriram, G. *et al*. Recent trends in the application of metal-organic frameworks (MOFs) for the removal of toxic dyes and their removal mechanism-a review. *Sustainable Materials and Technologies* vol. 31 Preprint at https://doi.org/10.1016/j.susmat.2021.e00378 (2022).

4. Osorio-Aguilar, D. M. *et al*. Adsorption and Photocatalytic Degradation of Methylene Blue in Carbon Nanotubes: A Review with Bibliometric Analysis. *Catalysts* vol. 13 Preprint at https://doi.org/10.3390/catal13121480 (2023).

5. Van Der Bruggen, B., Daems, B., Wilms, D. & Vandecasteele, C. Mechanisms of retention and flux decline for the nanofiltration of dye baths from the textile industry. *Sep Purif Technol* **22–23**, 519–528 (2001).

6. Farias, R. M. D. C. *et al*. Green synthesis of porous N-Carbon/Silica nanofibers by solution blow spinning and evaluation of their efficiency in dye adsorption. *Journal of Materials Research and Technology* **9**, 3038–3046 (2020).

7. Alvarenga, A. D. & Correa, D. S. Composite nanofibers membranes produced by solution blow spinning modified with CO2-activated sugarcane bagasse fly ash for efficient removal of water pollutants. *J Clean Prod* **285**, (2021).

8. Lee, J. W., Choi, S. P., Thiruvenkatachari, R., Shim, W. G. & Moon, H. Evaluation of the performance of adsorption and coagulation processes for the maximum removal of reactive dyes. *Dyes and Pigments* **69**, 196–203 (2006).

9. Szyguła, A., Guibal, E., Palacín, M. A., Ruiz, M. & Sastre, A. M. Removal of an anionic dye (Acid Blue 92) by coagulation–flocculation using chitosan. *J Environ Manage* **90**, 2979–2986 (2009).

10. Ihaddaden, S., Aberkane, D., Boukerroui, A. & Robert, D. Removal of methylene blue (basic dye) by coagulation-flocculation with biomaterials (bentonite and Opuntia ficus indica). *Journal of Water Process Engineering* **49**, 102952 (2022).

11. Riera-Torres, M., Gutiérrez-Bouzán, C. & Crespi, M. Combination of coagulation–flocculation and nanofiltration techniques for dye removal and water reuse in textile effluents. *Desalination* **252**, 53–59 (2010).

12. Quynh, H. G. *et al*. Rapid removal of methylene blue by a heterogeneous photo-Fenton process using economical and simple-synthesized magnetite–zeolite composite. *Environ Technol Innov* **31**, 103155 (2023).

13. Gao, T. *et al*. Decolorization and detoxification of triphenylmethane dyes by isolated endophytic fungus, Bjerkandera adusta SWUSI4 under non-nutritive conditions. *Bioresour. Bioprocess* **7**, 53 (2020).

14. Montañez-Barragán, B. *et al*. Azo dyes decolorization under high alkalinity and salinity conditions by Halomonas sp. in batch and packed bed reactor. **24**, 239–247 (2020).

15. Xu, L. *et al*. Laccase production by Trametes versicolor in solid-state fermentation using tea residues as substrate and its application in dye decolorization. *J Environ Manage* **270**, 110904 (2020).

16. Natarajan, S., Bajaj, H. C. & Tayade, R. J. Recent advances based on the synergetic effect of adsorption for removal of dyes from waste water using photocatalytic process. *Journal of Environmental Sciences (China)* vol. 65 201–222 Preprint at https://doi.org/10.1016/j.jes.2017.03.011 (2018).

17. Lu, J. *et al*. Review on multi-dimensional assembled S-scheme heterojunction photocatalysts. *J Mater Sci Technol* **160**, 214–239 (2023).

18. Zu, D. *et al*. The Role of Point Defects in Heterojunction Photocatalysts: Perspectives and Outlooks. *Advanced Functional Materials* Preprint at https://doi.org/10.1002/adfm.202408213 (2024).

19. Eshete, M. *et al*. Charge Steering in Heterojunction Photocatalysis: General Principles, Design, Construction, and Challenges. *Small Science* vol. 3 Preprint at https://doi.org/10.1002/smsc.202200041 (2023).

20. Rathi, B. S., Kumar, P. S. & Vo, D. V. N. Critical review on hazardous pollutants in water environment: Occurrence, monitoring, fate, removal technologies and risk assessment. *Science of the Total Environment* **797**, (2021).

21. Zhang, X. *et al*. State-of-the-art strategies to enhance the mechanical properties of microneedles. *International Journal of Pharmaceutics* vol. 663 Preprint at https://doi.org/10.1016/j.ijpharm.2024.124547 (2024).

22. McNaught, A. D., Wilkinson, A. & Jenkins, A. D. *IUPAC Compendium of Chemical Terminology: The Gold Book*. (International Union of Pure and Applied Chemistry: Research Triangle Park, NC, USA, 2006).

23. Mishra, S. & Sundaram, B. A review of the photocatalysis process used for wastewater treatment. *Mater Today Proc* (2023) doi:10.1016/j.matpr.2023.07.147.

24. Nie, C. *et al*. Advancements in S-scheme heterojunction materials for photocatalytic environmental remediation. *Journal of Materials Science and Technology* vol. 169 182–198 Preprint at https://doi.org/10.1016/j.jmst.2023.06.011 (2024).

25. Belousov, A. S., Parkhacheva, A. A., Suleimanov, E. V. & Shafiq, I. Potential of Bi2WO6-based heterojunction photocatalysts for environmental remediation. *Materials Today Chemistry* vol. 32 Preprint at https://doi.org/10.1016/j.mtchem.2023.101633 (2023).

26. Shen, S., Zhao, L. & Guo, L. Morphology, structure and photocatalytic performance of ZnIn2S4 synthesized via a solvothermal/hydrothermal route in different solvents. *Journal of Physics and Chemistry of Solids* **69**, 2426–2432 (2008).

27. Li, G. *et al*. Microwave synthesis of BiPO4 nanostructures and their morphology-dependent photocatalytic performances. *J Colloid Interface Sci* **363**, 497–503 (2011).

28. Li, Y., Sun, S., Ma, M., Ouyang, Y. & Yan, W. Kinetic study and model of the photocatalytic degradation of rhodamine B (RhB) by a TiO2-coated activated carbon catalyst: Effects of

initial RhB content, light intensity and TiO2 content in the catalyst. *Chemical Engineering Journal* vol. 142 147–155 Preprint at https://doi.org/10.1016/j.cej.2008.01.009 (2008).

29. Reza, K. M., Kurny, A. & Gulshan, F. Parameters affecting the photocatalytic degradation of dyes using TiO2: a review. *Applied Water Science* vol. 7 1569–1578 Preprint at https://doi.org/10.1007/s13201-015-0367-y (2017).

30. Jabbar, Z. H. & Graimed, B. H. Recent developments in industrial organic degradation via semiconductor heterojunctions and the parameters affecting the photocatalytic process: A review study. *Journal of Water Process Engineering* vol. 47 Preprint at https://doi.org/10.1016/j.jwpe.2022.102671 (2022).

31. Marcelino, R. B. P. & Amorim, C. C. Towards visible-light photocatalysis for environmental applications: band-gap engineering versus photons absorption—a review. *Environmental Science and Pollution Research* vol. 26 4155–4170 Preprint at https://doi.org/10.1007/s11356-018-3117-5 (2019).

32. Yuan, L. *et al*. Metal-organic framework-based S-scheme heterojunction photocatalysts. *Nanoscale* vol. 16 5487–5503 Preprint at https://doi.org/10.1039/d3nr06677k (2024).

33. Puga, F., Navío, J. A. & Hidalgo, M. C. A critical view about use of scavengers for reactive species in heterogeneous photocatalysis. *Applied Catalysis A: General* vol. 685 Preprint at https://doi.org/10.1016/j.apcata.2024.119879 (2024).

34. Ibhadon, A. O. & Fitzpatrick, P. Heterogeneous photocatalysis: Recent advances and applications. *Catalysts* vol. 3 189–218 Preprint at https://doi.org/10.3390/catal3010189 (2013).

35. Ahmed, S. N. & Haider, W. Heterogeneous photocatalysis and its potential applications in water and wastewater treatment: A review. *Nanotechnology* vol. 29 Preprint at https://doi.org/10.1088/1361-6528/aac6ea (2018).

36. Byrne, C., Subramanian, G. & Pillai, S. C. Recent advances in photocatalysis for environmental applications. *J Environ Chem Eng* **6**, 3531–3555 (2018).

37. Li, S. *et al*. Photocatalytic degradation of hazardous organic pollutants in water by Fe-MOFs and their composites: A review. *Journal of Environmental Chemical Engineering* vol. 9 Preprint at https://doi.org/10.1016/j.jece.2021.105967 (2021).

38. Pi, Y. *et al*. Adsorptive and photocatalytic removal of Persistent Organic Pollutants (POPs) in water by metal-organic frameworks (MOFs). *Chemical Engineering Journal* vol. 337 351–371 Preprint at https://doi.org/10.1016/j.cej.2017.12.092 (2018).

39. Hasan, Z. & Jhung, S. H. Removal of hazardous organics from water using metal-organic frameworks (MOFs): Plausible mechanisms for selective adsorptions. *Journal of Hazardous Materials* vol. 283 329–339 Preprint at https://doi.org/10.1016/j.jhazmat.2014.09.046 (2015).

40. *Communications to the Editor*.

41. Tibbetts, I. & Kostakis, G. E. Recent bio-advances in metal-organic frameworks. *Molecules* vol. 25 Preprint at https://doi.org/10.3390/molecules25061291 (2020).

42. Pinar Gumus, Z. & Soylak, M. Metal organic frameworks as nanomaterials for analysis of toxic metals in food and environmental applications. *TrAC - Trends in Analytical Chemistry* vol. 143 Preprint at https://doi.org/10.1016/j.trac.2021.116417 (2021).

43. Tchinsa, A., Hossain, M. F., Wang, T. & Zhou, Y. Removal of organic pollutants from aqueous solution using metal organic frameworks (MOFs)-based adsorbents: A review. *Chemosphere* vol. 284 Preprint at https://doi.org/10.1016/j.chemosphere.2021.131393 (2021).

44. Kuppler, R. J. *et al*. Potential applications of metal-organic frameworks. *Coordination Chemistry Reviews* vol. 253 3042–3066 Preprint at https://doi.org/10.1016/j.ccr.2009.05.019 (2009).

45. Dhaka, S. *et al*. Metal–organic frameworks (MOFs) for the removal of emerging contaminants from aquatic environments. *Coordination Chemistry Reviews* vol. 380 330–352 Preprint at https://doi.org/10.1016/j.ccr.2018.10.003 (2019).

46. Gropp, C. *et al*. Standard Practices of Reticular Chemistry. *ACS Cent Sci* **6**, 1255–1273 (2020).

47. Zhao, X., Li, J., Li, X., Huo, P. & Shi, W. Design of metal-organic frameworks (MOFs)-based photocatalyst for solar fuel production and photo-degradation of pollutants. *Chinese Journal of Catalysis* vol. 42 872–903 Preprint at https://doi.org/10.1016/S1872-2067(20)63715-9 (2021).

48. Wen, Y. *et al*. Metal Organic Frameworks (MOFs) as Photocatalysts for the Degradation of Agricultural Pollutants in Water. *ACS ES and T Engineering* vol. 1 804–826 Preprint at https://doi.org/10.1021/acsestengg.1c00051 (2021).

49. Du, C. *et al*. Fe-based metal organic frameworks (Fe-MOFs) for organic pollutants removal via photo-Fenton: A review. *Chemical Engineering Journal* vol. 431 Preprint at https://doi.org/10.1016/j.cej.2021.133932 (2022).

50. Zhang, X., Wang, J., Dong, X. X. & Lv, Y. K. Functionalized metal-organic frameworks for photocatalytic degradation of organic pollutants in environment. *Chemosphere* vol. 242 Preprint at https://doi.org/10.1016/j.chemosphere.2019.125144 (2020).

51. Li, S. *et al*. Photocatalytic degradation of hazardous organic pollutants in water by Fe-MOFs and their composites: A review. *Journal of Environmental Chemical Engineering* vol. 9 Preprint at https://doi.org/10.1016/j.jece.2021.105967 (2021).

52. Wang, Z. *et al*. Application of MOFs driven by various energy sources for degradation the organic pollutants in water: A review. *Coordination Chemistry Reviews* vol. 499 Preprint at https://doi.org/10.1016/j.ccr.2023.215506 (2024).

53. Fu, H. *et al*. Room-temperature preparation of MIL-88A as a heterogeneous photo-Fenton catalyst for degradation of rhodamine B and bisphenol a under visible light. *Mater Res Bull* **125**, (2020).

54. Wang, Z. *et al*. Optimizing the performance of Fe-based metal-organic frameworks in photo-Fenton processes: Mechanisms, strategies and prospects. *Chemosphere* vol. 339 Preprint at https://doi.org/10.1016/j.chemosphere.2023.139673 (2023).

55. Wang, L. *et al*. The chemical stability of metal-organic frameworks in water treatments: Fundamentals, effect of water matrix and judging methods. *Chemical Engineering Journal* vol. 450 Preprint at https://doi.org/10.1016/j.cej.2022.138215 (2022).

56. Hmoudah, M. *et al*. Assessment of the robustness of MIL-88A in an aqueous solution: Experimental and DFT investigations. *Materials Science and Engineering: B* **288**, (2023).

57. Naghdi, S. *et al*. Recent advances in application of metal-organic frameworks (MOFs) as adsorbent and catalyst in removal of persistent organic pollutants (POPs). *Journal of Hazardous Materials* vol. 442 Preprint at https://doi.org/10.1016/j.jhazmat.2022.130127 (2023).

58. Yuan, L. *et al*. Metal-organic framework-based S-scheme heterojunction photocatalysts. *Nanoscale* vol. 16 5487–5503 Preprint at https://doi.org/10.1039/d3nr06677k (2024).

59. Yuan, Y. *et al*. Recent advances and perspectives of MoS2-based materials for photocatalytic dyes degradation: A review. *Colloids and Surfaces A: Physicochemical and Engineering Aspects* vol. 611 Preprint at https://doi.org/10.1016/j.colsurfa.2020.125836 (2021).

60. Thomas, N. *et al*. 2D MoS2: structure, mechanisms, and photocatalytic applications. *Materials Today Sustainability* **13**, (2021).

61. Li, Z., Meng, X. & Zhang, Z. Recent development on MoS2-based photocatalysis: A review. *Journal of Photochemistry and Photobiology C: Photochemistry Reviews* vol. 35 39–55 Preprint at https://doi.org/10.1016/j.jphotochemrev.2017.12.002 (2018).

62. Che, L., Pan, J., Cai, K., Cong, Y. & Lv, S. W. The construction of p-n heterojunction for enhancing photocatalytic performance in environmental application: A review. *Separation and Purification Technology* vol. 315 Preprint at https://doi.org/10.1016/j.seppur.2023.123708 (2023).

63. Salazar-Marín, D. *et al*. Distinguishing between type II and S-scheme heterojunction materials: A comprehensive review. *Applied Surface Science Advances* vol. 19 Preprint at https://doi.org/10.1016/j.apsadv.2023.100536 (2024).

64. Wang, Z., Yue, X. & Xiang, Q. MOFs-based S-scheme heterojunction photocatalysts. *Coordination Chemistry Reviews* vol. 504 Preprint at https://doi.org/10.1016/j.ccr.2024.215674 (2024).

65. Balakrishnan, A., Gaware, G. J. & Chinthala, M. Heterojunction photocatalysts for the removal of nitrophenol: A systematic review. *Chemosphere* vol. 310 Preprint at https://doi.org/10.1016/j.chemosphere.2022.136853 (2023).

66. Roy, D., Neogi, S. & De, S. Mechanistic investigation of photocatalytic degradation of Bisphenol-A using MIL-88A(Fe)/MoS2 Z-scheme heterojunction composite assisted peroxymonosulfate activation. *Chemical Engineering Journal* **428**, (2022).

67. Govarthanan, M., Mythili, R., Kim, W., Alfarraj, S. & Alharbi, S. A. Facile fabrication of (2D/2D) MoS2@MIL-88(Fe) interface-driven catalyst for efficient degradation of organic pollutants under visible light irradiation. *J Hazard Mater* **414**, (2021).

68. Yadav, M., Garg, S., Chandra, A. & Hernadi, K. Immobilization of green BiOX (X= Cl, Br and I) photocatalysts on ceramic fibers for enhanced photocatalytic degradation of recalcitrant organic pollutants and efficient regeneration process. *Ceram Int* **45**, 17715–17722 (2019).

69. Yadav, M., Garg, S., Chandra, A. & Hernadi, K. Immobilization of green BiOX (X= Cl, Br and I) photocatalysts on ceramic fibers for enhanced photocatalytic degradation of recalcitrant organic pollutants and efficient regeneration process. *Ceram Int* **45**, 17715–17722 (2019).

70. Wang, Y., Zhang, Y., Wang, S. & Guan, Y. A 3D printed synergistic aerogel microreactor toward stable and high-efficiency photocatalytic degradation. *Mater Today Chem* **22**, (2021).

71. Yanar, N. *et al*. A New era of water treatment technologies: 3D printing for membranes. *Journal of Industrial and Engineering Chemistry* vol. 91 1–14 Preprint at https://doi.org/10.1016/j.jiec.2020.07.043 (2020).

72. Ngo, T. D., Kashani, A., Imbalzano, G., Nguyen, K. T. Q. & Hui, D. Additive manufacturing (3D printing): A review of materials, methods, applications and challenges. *Composites Part B: Engineering* vol. 143 172–196 Preprint at https://doi.org/10.1016/j.compositesb.2018.02.012 (2018).

73. Rocha, V. G., Saiz, E., Tirichenko, I. S. & García-Tuñón, E. Direct ink writing advances in multi-material structures for a sustainable future. *Journal of Materials Chemistry A* vol. 8 15646–15657 Preprint at https://doi.org/10.1039/d0ta04181e (2020).

74. Tsang, A. C. H., Zhang, J., Hui, K. N., Hui, K. S. & Huang, H. Recent Development and Applications of Advanced Materials via Direct Ink Writing. *Advanced Materials Technologies* vol. 7 Preprint at https://doi.org/10.1002/admt.202101358 (2022).

75. Amorim, P. A. *et al*. Insights on shear rheology of inks for extrusion-based 3D bioprinting. *Bioprinting* vol. 22 Preprint at https://doi.org/10.1016/j.bprint.2021.e00129 (2021).

76. Feng, J. *et al*. Printed aerogels: Chemistry, processing, and applications. *Chemical Society Reviews* vol. 50 3842–3888 Preprint at https://doi.org/10.1039/c9cs00757a (2021).

77. Jungst, T., Smolan, W., Schacht, K., Scheibel, T. & Groll, J. Strategies and Molecular Design Criteria for 3D Printable Hydrogels. *Chemical Reviews* vol. 116 1496–1539 Preprint at https://doi.org/10.1021/acs.chemrev.5b00303 (2016).

78. Mewis, J. & Wagner, N. J. Thixotropy. *Adv Colloid Interface Sci* **147–148**, 214–227 (2009).

79. Weerasundara, L., Gabriele, B., Figoli, A., Ok, Y. S. & Bundschuh, J. Hydrogels: Novel materials for contaminant removal in water—A review. *Crit Rev Environ Sci Technol* **51**, 1970–2014 (2021).

80. Li, H., Tan, C. & Li, L. Review of 3D printable hydrogels and constructs. *Mater Des* **159**, 20–38 (2018).

81. Dai, H., Ou, S., Huang, Y., Liu, Z. & Huang, H. Enhanced swelling and multiple-responsive properties of gelatin/sodium alginate hydrogels by the addition of carboxymethyl cellulose isolated from pineapple peel. *Cellulose* **25**, 593–606 (2018).

82. Sathish, P. B. *et al*. Tricomposite gelatin-carboxymethylcellulose-alginate bioink for direct and indirect 3D printing of human knee meniscal scaffold. *Int J Biol Macromol* **195**, 179–189 (2022).

83. Janarthanan, G. & Noh, I. Recent trends in metal ion based hydrogel biomaterials for tissue engineering and other biomedical applications. *J Mater Sci Technol* **63**, 35–53 (2021).

84. GhavamiNejad, A., Ashammakhi, N., Wu, X. Y. & Khademhosseini, A. Crosslinking Strategies for 3D Bioprinting of Polymeric Hydrogels. *Small* vol. 16 Preprint at https://doi.org/10.1002/smll.202002931 (2020).

85. Zheng, W. *et al*. Layer-by-layer coating of carboxymethyl chitosan-gelatin-alginate on cotton gauze for hemostasis and wound healing. *Surf Coat Technol* **406**, (2021).

86. Sehaqui, H., Zhou, Q. & Berglund, L. A. High-porosity aerogels of high specific surface area prepared from nanofibrillated cellulose (NFC). *Compos Sci Technol* **71**, 1593–1599 (2011).

87. Fu, S. *et al*. 3D printing of layered mesoporous bioactive glass/sodium alginatesodium alginate scaffolds with controllable dual-drug release behaviors. *Biomedical Materials (Bristol)* **14**, (2019).

88. Wang, L., Xu, H., Gao, J., Yao, J. & Zhang, Q. Recent progress in metal-organic frameworks-based hydrogels and aerogels and their applications. *Coord Chem Rev* **398**, 213016 (2019).

89. Kumar, N., Gusain, R., Pandey, S. & Ray, S. S. Hydrogel Nanocomposite Adsorbents and Photocatalysts for Sustainable Water Purification. *Advanced Materials Interfaces* vol. 10 Preprint at https://doi.org/10.1002/admi.202201375 (2023).

90. Li, Y. *et al*. Fe3+-citric acid/sodium alginate hydrogel: A photo-responsive platform for rapid water purification. *Carbohydr Polym* **269**, (2021).

91. Karadeniz, D., Kahya, N. & Erim, F. B. Effective photocatalytic degradation of malachite green dye by Fe(III)-Cross-linked Alginate-Carboxymethyl cellulose composites. *J Photochem Photobiol A Chem* **428**, (2022).

92. Dos Santos, D. M., Correa, D. S., Medeiros, E. S., Oliveira, J. E. & Mattoso, L. H. C. Advances in Functional Polymer Nanofibers: From Spinning Fabrication Techniques to Recent Biomedical Applications. *ACS applied materials & interfaces* vol. 12 45673–45701 Preprint at https://doi.org/10.1021/acsami.0c12410 (2020).

93. Gao, Y. *et al*. Recent progress and challenges in solution blow spinning. *Materials Horizons* vol. 8 426–446 Preprint at https://doi.org/10.1039/d0mh01096k (2021).

94. Dadol, G. C. *et al*. Solution blow spinning (SBS) and SBS-spun nanofibers: Materials, methods, and applications. *Mater Today Commun* **25**, (2020).

95. Gao, Y. *et al*. Recent progress and challenges in solution blow spinning. *Materials Horizons* vol. 8 426–446 Preprint at https://doi.org/10.1039/d0mh01096k (2021).

96. Gonzalez-Abrego, M. *et al*. Mesoporous titania nanofibers by solution blow spinning. *J Solgel Sci Technol* **81**, 468–474 (2017).

97. Chen, Y. *et al*. Catalyst-free large-scale synthesis of composite SiC@SiO2/carbon nanofiber mats by blow-spinning. *J Mater Chem C Mater* **7**, 15233–15242 (2019).

98. You, Y. *et al*. Zirconia-Doped Alumina Submicron Fibers with Compressibility and High-Temperature Resistance Prepared by Solution Blow Spinning for Thermal Insulation. *ACS Appl Nano Mater* (2024) doi:10.1021/acsanm.4c04411.

99. Schneider, R. *et al*. Tailoring the Surface Properties of Micro/Nanofibers Using 0D, 1D, 2D, and 3D Nanostructures: A Review on Post-Modification Methods. *Advanced Materials Interfaces* vol. 8 Preprint at https://doi.org/10.1002/admi.202100430 (2021).

100. Ahmed, J. *et al*. Efficient Photocatalytic Degradation of Methyl Red Dye Using Electrospun Nanofibers: A Bio-Inspired Approach for Wastewater Remediation. *J Polym Environ* **32**, 1784–1795 (2024).

101. Hromádko, L., Koudelková, E., Bulánek, R. & Macak, J. M. SiO2 Fibers by Centrifugal Spinning with Excellent Textural Properties and Water Adsorption Performance. *ACS Omega* **2**, 5052–5059 (2017).

102. Tepekiran, B. N., Calisir, M. D., Polat, Y., Akgul, Y. & Kilic, A. Centrifugally spun silica (SiO2) nanofibers for high-temperature air filtration. *Aerosol Science and Technology* **53**, 921–932 (2019).

103. Tański, T., Matysiak, W., Krzemiński, Ł., Jarka, P. & Gołombek, K. Optical properties of thin fibrous PVP/SiO 2 composite mats prepared via the sol-gel and electrospinning methods. *Appl Surf Sci* **424**, 184–189 (2017).

104. Chen, W. Q. *et al*. MoS2/ZIF-8 Hybrid Materials for Environmental Catalysis: Solar-Driven Antibiotic-Degradation Engineering. *Engineering* **5**, 755–767 (2019).

105. Li, Q. *et al*. Rational design of MIL-88A(Fe)/Bi2WO6 heterojunctions as an efficient photocatalyst for organic pollutant degradation under visible light irradiation. *Opt Mater (Amst)* **118**, (2021).

106. Zhang, W. *et al*. Agar Aerogel Containing Small-Sized Zeolitic Imidazolate Framework Loaded Carbon Nitride: A Solar-Triggered Regenerable Decontaminant for Convenient and Enhanced Water Purification. *ACS Sustain Chem Eng* **5**, 9347–9354 (2017).

107. Jia, C., Xu, Z., Luo, D., Xiang, H. & Zhu, M. Flexible Ceramic Fibers: Recent Development in Preparation and Application. *Advanced Fiber Materials* vol. 4 573–603 Preprint at https://doi.org/10.1007/s42765-022-00133-y (2022).

108. Sawunyama, L., Oyewo, O. A., Seheri, N., Onjefu, S. A. & Onwudiwe, D. C. Metal oxide functionalized ceramic membranes for the removal of pharmaceuticals in wastewater. *Surfaces and Interfaces* vol. 38 Preprint at https://doi.org/10.1016/j.surfin.2023.102787 (2023).

109. Alves, A. L. M. M., dos Santos, F. V. & Correa, D. S. 3D-printed MOF/MoS2 aerogel for dye adsorption and photocatalytic degradation. *Mater Today Chem* **40**, (2024).

110. Mittal, H., Al Alili, A., Morajkar, P. P. & Alhassan, S. M. GO crosslinked hydrogel nanocomposites of chitosan/carboxymethyl cellulose – A versatile adsorbent for the treatment of dyes contaminated wastewater. *Int J Biol Macromol* **167**, 1248–1261 (2021).

111. Li, S. *et al*. Photocatalytic degradation of hazardous organic pollutants in water by Fe-MOFs and their composites: A review. *Journal of Environmental Chemical Engineering* vol. 9 Preprint at https://doi.org/10.1016/j.jece.2021.105967 (2021).

112. Chen, S. & Liu, Y. Study on the photocatalytic degradation of glyphosate by TiO2 photocatalyst. *Chemosphere* **67**, 1010–1017 (2007).

113. Li, Y. *et al*. Comparison of dye photodegradation and its coupling with light-to-electricity conversion over TiO2 and ZnO. *Langmuir* **26**, 591–597 (2010).

114. Zhang, Y., Zhou, J., Chen, X., Wang, L. & Cai, W. Coupling of heterogeneous advanced oxidation processes and photocatalysis in efficient degradation of tetracycline

hydrochloride by Fe-based MOFs: Synergistic effect and degradation pathway. *Chemical Engineering Journal* **369**, 745–757 (2019).

115. Quan, Y. *et al*. Construction of an MZO heterojunction system with improved photocatalytic activity for degradation of organic dyes. *CrystEngComm* **22**, 7059–7065 (2020).

116. Chang, X. *et al*. Photodegradation of Rhodamine B over unexcited semiconductor compounds of BiOCl and BiOBr. *J Colloid Interface Sci* **377**, 291–298 (2012).

117. Ramezanalizadeh, H. & Manteghi, F. Synthesis of a novel MOF/CuWO4 heterostructure for efficient photocatalytic degradation and removal of water pollutants. *J Clean Prod* **172**, 2655–2666 (2016).

118. Khalid, N. R., Israr, Z., Tahir, M. B. & Iqbal, T. Highly efficient Bi2O3/MoS2 p-n heterojunction photocatalyst for H2 evolution from water splitting. *Int J Hydrogen Energy* **45**, 8479–8489 (2020).

119. Guo, Y. *et al*. A simple and effective method for fabricating novel p-n heterojunction photocatalyst g-C3N4/Bi4Ti3O12 and its photocatalytic performances. *Appl Catal B* **192**, 57–71 (2016).

120. Li, X. *et al*. Growth of BiOBr/ZIF-67 Nanocomposites on Carbon Fiber Cloth as Filter-Membrane-Shaped Photocatalyst for Degrading Pollutants in Flowing Wastewater. *Advanced Fiber Materials* **4**, 1620–1631 (2022).

121. Li, S., Cai, M., Wang, C. & Liu, Y. Ta3N5/CdS Core–Shell S-scheme Heterojunction Nanofibers for Efficient Photocatalytic Removal of Antibiotic Tetracycline and Cr(VI): Performance and Mechanism Insights. *Advanced Fiber Materials* **5**, 994–1007 (2023).

122. Zhang, Y. *et al*. Fabrication of NH2-MIL-125(Ti) nanodots on carbon fiber/MoS2-based weavable photocatalysts for boosting the adsorption and photocatalytic performance. *J Colloid Interface Sci* **611**, 706–717 (2022).

123. Pereira, A. G. B., Rodrigues, F. H. A., Paulino, A. T., Martins, A. F. & Fajardo, A. R. Recent advances on composite hydrogels designed for the remediation of dye-contaminated water and wastewater: A review. *Journal of Cleaner Production* vol. 284 Preprint at https://doi.org/10.1016/j.jclepro.2020.124703 (2021).

124. Sivakumar, R. & Lee, N. Y. Adsorptive removal of organic pollutant methylene blue using polysaccharide-based composite hydrogels. *Chemosphere* **286**, (2022).

125. Ahmaruzzaman, M. *et al*. Polymeric hydrogels-based materials for wastewater treatment. *Chemosphere* vol. 331 Preprint at https://doi.org/10.1016/j.chemosphere.2023.138743 (2023).

126. Wang, Z. *et al*. Lightweight UiO-66/cellulose aerogels constructed through self-crosslinking strategy for adsorption applications. *Chemical Engineering Journal* **371**, 138–144 (2019).

127. Radoor, S. *et al*. Recent advances in cellulose- and alginate-based hydrogels for water and wastewater treatment: A review. *Carbohydrate Polymers* vol. 323 Preprint at https://doi.org/10.1016/j.carbpol.2023.121339 (2024).

128. Rigueto, C. V. T. *et al*. Production and environmental applications of gelatin-based composite adsorbents for contaminants removal: a review. *Environmental Chemistry Letters* vol. 19 2465–2486 Preprint at https://doi.org/10.1007/s10311-021-01184-0 (2021).

129. Zheng, D., Wang, K. & Bai, B. A critical review of sodium alginate-based composites in water treatment. *Carbohydrate Polymers* vol. 331 Preprint at https://doi.org/10.1016/j.carbpol.2024.121850 (2024).

130. Massana Roquero, D., Othman, A., Melman, A. & Katz, E. Iron(iii)-cross-linked alginate hydrogels: A critical review. *Materials Advances* vol. 3 1849–1873 Preprint at https://doi.org/10.1039/d1ma00959a (2022).

131. Li, S. S. *et al*. Modifying alginate beads using polycarboxyl component for enhanced metal ions removal. *Int J Biol Macromol* **158**, 493–501 (2020).

132. Shojaeiarani, J., Shirzadifar, A. & Bajwa, D. S. Robust and porous 3D-printed multifunctional hydrogels for efficient removal of cationic and anionic dyes from aqueous solution. *Microporous and Mesoporous Materials* **327**, (2021).

133. Finny, A. S., Cheng, N., Popoola, O. & Andreescu, S. 3D printable polyethyleneimine based hydrogel adsorbents for heavy metal ions removal†. *Environmental Science: Advances* **1**, 443–455 (2022).

134. Li, Y. *et al*. Material extrusion-based 3D printing for the fabrication of bacteria into functional biomaterials: The case study of ammonia removal application. *Addit Manuf* **60**, (2022).

135. Yang, L. *et al*. 3D-printed N-doped porous carbon aerogels for efficient flow-through degradation and disinfection of wastewater. *Sep Purif Technol* **320**, (2023).

136. Maleki, H. & Hüsing, N. Aerogels as promising materials for environmental remediation-A broad insight into the environmental pollutants removal through adsorption and (photo)catalytic processes. in *New Polymer Nanocomposites for Environmental Remediation* 389–436 (Elsevier Inc., 2018). doi:10.1016/B978-0-12-811033-1.00016-0.

137. Schneider, R. *et al*. Dye Adsorption Capacity of MoS2Nanoflakes Immobilized on Poly(lactic acid) Fibrous Membranes. *ACS Appl Nano Mater* **4**, 4881–4894 (2021).

138. Antunes, M. *et al*. Development of alginate-based hydrogels for blood vessel engineering. *Materials Science and Engineering C* (2021) doi:10.1016/j.msec.2021.112588.

139. Bierhalz, A. C. K., da Silva, M. A., Braga, M. E. M., Sousa, H. J. C. & Kieckbusch, T. G. Effect of calcium and/or barium crosslinking on the physical and antimicrobial properties of natamycin-loaded alginate films. *LWT* **57**, 494–501 (2014).

140. Li, G., Zhang, G., Sun, R. & Wong, C. P. Mechanical strengthened alginate/polyacrylamide hydrogel crosslinked by barium and ferric dual ions. *J Mater Sci* **52**, 8538–8545 (2017).

141. Dodero, A. *et al*. Alginate-based hydrogels prepared via ionic gelation: An experimental design approach to predict the crosslinking degree. *Eur Polym J* **118**, 586–594 (2019).

142. Gao, N. *et al*. Ba2+/Ca2+ co-crosslinked alginate hydrogel filtration membrane with high strength, high flux and stability for dye/salt separation. *Chinese Chemical Letters* 108820 (2023) doi:10.1016/j.cclet.2023.108820.

143. Lee, K. H. *et al*. Porous Aerogel Structures as Promising Materials for Photocatalysis, Thermal Insulation Textiles, and Technical Applications: A Review. *Catalysts* vol. 13 Preprint at https://doi.org/10.3390/catal13091286 (2023).

144. Baigorria, E., Souza dos Santos, S., de Moura, M. R. & Fraceto, L. F. Nanocomposite hydrogels 3D printed for application in water remediation. *Mater Today Chem* **30**, (2023).

145. Bercea, M. Rheology as a Tool for Fine-Tuning the Properties of Printable Bioinspired Gels. *Molecules* **28**, 1–28 (2023).

146. Pössl, A., Hartzke, D., Schmidts, T. M., Runkel, F. E. & Schlupp, P. A targeted rheological bioink development guideline and its systematic correlation with printing behavior. *Biofabrication* **13**, 035021 (2021).

147. Perin, F. *et al*. Modeling a Dynamic Printability Window on Polysaccharide Blend Inks for Extrusion Bioprinting. *ACS Biomater Sci Eng* **9**, 1320–1331 (2023).

148. Karvinen, J. & Kellomäki, M. Design aspects and characterization of hydrogel-based bioinks for extrusion-based bioprinting. *Bioprinting* **32**, e00274 (2023).

149. Dávila, J. L. & d'Ávila, M. A. Rheological evaluation of Laponite/alginate inks for 3D extrusion-based printing. *International Journal of Advanced Manufacturing Technology* **101**, 675–686 (2019).

150. Iervolino, F. *et al*. Versatile and non-cytotoxic GelMA-xanthan gum biomaterial ink for extrusion-based 3D bioprinting. *Bioprinting* **31**, (2023).

151. Wei, Y., Guo, Y., Li, R., Ma, A. & Zhang, H. Food Hydrocolloids Rheological characterization of polysaccharide thickeners oriented for dysphagia management : Carboxymethylated curdlan , konjac glucomannan and their mixtures compared to xanthan gum. *Food Hydrocoll* **110**, 106198 (2021).

152. Alcala-orozco, C. R. *et al*. Bioprinting Design and characterisation of multi-functional strontium-gelatin nanocomposite bioinks with improved print fi delity and osteogenic capacity. *Bioprinting* **18**, e00073 (2020).

153. Zhang, T. *et al*. Bioink design for extrusion-based bioprinting. *Appl Mater Today* **25**, 101227 (2021).

154. Ramesh, S. *et al*. Extrusion bioprinting: Recent progress, challenges, and future opportunities. *Bioprinting* **21**, e00116 (2021).

155. Sánchez-sánchez, R., Rodríguez-rego, J. M., Macías-garcía, A. & Díaz-parralejo, A. Relationship between shear-thinning rheological properties of bioinks and bioprinting parameters. *International Journal Bioprinting* **9**, 422–431 (2023).

156. Cross, M. M. Rheology of non-Newtonian fluids: A new flow equation for pseudoplastic systems. *J Colloid Sci* **437**, 417–437 (1964).

157. Malda, J. *et al*. 25th anniversary article: Engineering hydrogels for biofabrication. *Advanced Materials* **25**, 5011–5028 (2013).

158. Amorim, P. A. *et al*. Insights on shear rheology of inks for extrusion-based 3D bioprinting. *Bioprinting* **22**, e00129 (2021).

159. Jiang, Y. *et al*. Rheological behavior, 3D printability and the formation of scaffolds with cellulose nanocrystals/gelatin hydrogels. *J Mater Sci* **55**, 15709–15725 (2020).

160. Li, H., Tan, Y. J. & Li, L. A strategy for strong interface bonding by 3D bioprinting of oppositely charged κ-carrageenan and gelatin hydrogels. *Carbohydr Polym* **198**, 261–269 (2018).

161. Boonlai, W., Tantishaiyakul, V. & Hirun, N. Characterization of κ-carrageenan/methylcellulose/cellulose nanocrystal hydrogels for 3D bioprinting. *Polym Int* **71**, 181–191 (2022).

162. Li, H., Tan, Y. J., Leong, K. F. & Li, L. 3D Bioprinting of Highly Thixotropic Alginate/Methylcellulose Hydrogel with Strong Interface Bonding. *ACS Appl Mater Interfaces* **9**, 20086–20097 (2017).

163. Peak, C. W., Stein, J., Gold, K. A. & Gaharwar, A. K. Nanoengineered Colloidal Inks for 3D Bioprinting. *Langmuir* **34**, 917–925 (2018).

164. Taniguchi Nagahara, M. H., Caiado Decarli, M., Inforçatti Neto, P., Lopes da Silva, J. V. & Moraes, Â. M. Crosslinked alginate-xanthan gum blends as effective hydrogels for 3D bioprinting of biological tissues. *J Appl Polym Sci* **139**, 1–15 (2022).

165. El Asmar, R. *et al*. Iron-based metal organic framework MIL-88-A for the degradation of naproxen in water through persulfate activation. *Chemical Engineering Journal* **405**, (2021).

166. Wang, Z. *et al*. Lightweight UiO-66/cellulose aerogels constructed through self-crosslinking strategy for adsorption applications. *Chemical Engineering Journal* **371**, 138–144 (2019).

167. Williams, J. C. *et al*. Highly porous, rigid-rod polyamide aerogels with superior mechanical properties and unusually high thermal conductivity. *ACS Appl Mater Interfaces* **9**, 1801–1809 (2017).

168. Iglesias-Mejuto, A. & García-González, C. A. 3D-printed alginate-hydroxyapatite aerogel scaffolds for bone tissue engineering. *Materials Science and Engineering C* **131**, (2021).

169. Fu, J., Yap, J. X., Leo, C. P. & Chang, C. K. Carboxymethyl cellulose/sodium alginate beads incorporated with calcium carbonate nanoparticles and bentonite for phosphate recovery. *Int J Biol Macromol* **234**, (2023).

170. Zhao, J., Zhang, Z., Yang, S., Zheng, H. & Li, Y. Facile synthesis of MoS2 nanosheet-silver nanoparticles composite for surface enhanced Raman scattering and electrochemical activity. *J Alloys Compd* **559**, 87–91 (2013).

171. Li, D. *et al*. Rapid Synthesis of Porous Graphene Microspheres through a Three-Dimensionally Printed Inkjet Nozzle for Selective Pollutant Removal from Water. *ACS Omega* **4**, 20509–20518 (2019).

172. Zafar, A., Khosa, M. K., Noor, A., Qayyum, S. & Saif, M. J. Carboxymethyl Cellulose/Gelatin Hydrogel Films Loaded with Zinc Oxide Nanoparticles for Sustainable Food Packaging Applications. *Polymers (Basel)* **14**, (2022).

173. Chen, B. *et al*. Structuring alginate/dopamine powder into macroscopic aerogel microsphere for exceptional removal of tetracycline from water: Performance and mechanisms. *Int J Biol Macromol* **242**, (2023).

174. Chen, L. *et al*. Fabrication of starch-based high-performance adsorptive hydrogels using a novel effective pretreatment and adsorption for cationic methylene blue dye: Behavior and mechanism. *Chemical Engineering Journal* **405**, (2021).

175. Deptuła, M. *et al*. Application of 3D- printed hydrogels in wound healing and regenerative medicine. *Biomedicine and Pharmacotherapy* vol. 167 Preprint at https://doi.org/10.1016/j.biopha.2023.115416 (2023).

176. Zhu, W. *et al*. Fabrication of reusable carboxymethyl cellulose/graphene oxide composite aerogel with large surface area for adsorption of methylene blue. *Nanomaterials* **11**, (2021).

177. Song, R., Yao, J., Yang, M. & Ye, Z. Insights into High-Performance and Selective Elimination of Cationic Dye from Multicomponent Systems by Using Fe-Based Metal-Organic Frameworks. *Langmuir* **38**, 9400–9409 (2022).

178. Wang, Z. *et al*. Controllable synthesis and adsorption mechanism of flower-like MoS2/g-C3N4 nanocomposites for the removal of methylene blue in water. *Journal of Nanoparticle Research* **24**, (2022).

179. Liu, Y. *et al*. Bio-based barium alginate film: Preparation, flame retardancy and thermal degradation behavior. *Carbohydr Polym* **139**, 106–114 (2016).

180. Kahya, N., Gölcü, A. & Erim, F. B. Barium ion cross-linked alginate-carboxymethyl cellulose composites for controlled release of anticancer drug methotrexate. *J Drug Deliv Sci Technol* **54**, (2019).

181. Bohač, M. *et al*. Novel, simple and low-cost preparation of Ba-modified TiO2 nanotubes for diclofenac degradation under UV/Vis radiation. *Nanomaterials* **11**, (2021).

182. Geng, Q. *et al*. Optimizing the Electronic Structure of BiOBr Nanosheets via Combined Ba Doping and Oxygen Vacancies for Promoted Photocatalysis. *Journal of Physical Chemistry C* **125**, 8597–8605 (2021).

183. Liu, X. *et al*. A general and programmable preparation of α-MnO2/GO/CS aerogels used for efficient degradation of MB in wastewater. *Sep Purif Technol* **301**, (2022).

184. Zhang, J. *et al*. A TiO 2 Coated Carbon Aerogel Derived from Bamboo Pulp Fibers for Enhanced Visible Light Photo-Catalytic Degradation of Methylene Blue. **11**, 239 (2021).

185. Sun, H. *et al*. MnO2 aerogels for highly efficient oxidative degradation of Rhodamine B. *RSC Adv* **7**, 30283–30288 (2017).

186. Kappadan, S., Gebreab, T. W., Thomas, S. & Kalarikkal, N. Tetragonal BaTiO3 nanoparticles: An efficient photocatalyst for the degradation of organic pollutants. *Mater Sci Semicond Process* **51**, 42–47 (2016).

187. Li, R., Li, Q., Zong, L., Wang, X. & Yang, J. BaTiO3/TiO2 heterostructure nanotube arrays for improved photoelectrochemical and photocatalytic activity. *Electrochim Acta* **91**, 30–35 (2013).

188. Wang, X., Li, D. & Nan, Z. Effect of N content in g-C3N4 as metal-free catalyst on H2O2 decomposition for MB degradation. *Sep Purif Technol* **224**, 152–162 (2019).

189. Jin, Y. *et al*. Highly efficient degradation of dye pollutants by Ce-doped MoO3 catalyst at room temperature. *Dalton Transactions* **43**, 12860–12870 (2014).

190. Zhang, T., Xiao, S., Fan, K., He, H. & Qin, Z. Preparation and adsorption properties of green cellulose-based composite aerogel with selective adsorption of methylene blue. *Polymer (Guildf)* **258**, (2022).

191. Wei, X. *et al*. Bio-inspired functionalization of microcrystalline cellulose aerogel with high adsorption performance toward dyes. *Carbohydr Polym* **198**, 546–555 (2018).

192. Yang, Z. *et al*. Preparation of β-cyclodextrin/graphene oxide and its adsorption properties for methylene blue. *Colloids Surf B Biointerfaces* **200**, (2021).

193. Han, X., Wang, W. & Ma, X. Adsorption characteristics of methylene blue onto low cost biomass material lotus leaf. *Chemical Engineering Journal* **171**, 1–8 (2011).

194. Abdel Ghafar, H. H., Ali, G. A. M., Fouad, O. A. & Makhlouf, S. A. Enhancement of adsorption efficiency of methylene blue on Co3O4/SiO2 nanocomposite. *Desalination Water Treat* **53**, 2980–2989 (2015).

195. Wang, Z. *et al*. Efficient adsorption of methylene blue from aqueous solution by graphene oxide modified persimmon tannins. *Materials Science and Engineering C* **108**, (2020).

196. Shojaeiarani, J., Shirzadifar, A. & Bajwa, D. S. Robust and porous 3D-printed multifunctional hydrogels for efficient removal of cationic and anionic dyes from aqueous solution. *Microporous and Mesoporous Materials* **327**, (2021).

197. Appuhamillage, G. A. *et al*. A biopolymer-based 3D printable hydrogel for toxic metal adsorption from water. *Polym Int* **68**, 964–971 (2019).

198. Zheng, D., Wang, K. & Bai, B. A critical review of sodium alginate-based composites in water treatment. *Carbohydr Polym* **331**, 121850 (2024).

199. Jabbar, Z. H. *et al*. The latest progress in the design and application of semiconductor photocatalysis systems for degradation of environmental pollutants in wastewater: Mechanism insight and theoretical calculations. *Materials Science in Semiconductor Processing* vol. 173 Preprint at https://doi.org/10.1016/j.mssp.2024.108153 (2024).

200. Rengifo-Herrera, J. A. & Pulgarin, C. Why five decades of massive research on heterogeneous photocatalysis, especially on TiO2, has not yet driven to water disinfection and detoxification applications? Critical review of drawbacks and challenges. *Chemical Engineering Journal* vol. 477 Preprint at https://doi.org/10.1016/j.cej.2023.146875 (2023).

201. Dutta, V. *et al*. An overview on WO3 based photocatalyst for environmental remediation. *J Environ Chem Eng* **9**, 105018 (2021).

202. Chen, X., Wu, Z., Liu, D. & Gao, Z. Preparation of ZnO Photocatalyst for the Efficient and Rapid Photocatalytic Degradation of Azo Dyes. *Nanoscale Res Lett* **12**, (2017).

203. García-Salcido, V., Mercado-Oliva, P., Guzmán-Mar, J. L., Kharisov, B. I. & Hinojosa-Reyes, L. MOF-based composites for visible-light-driven heterogeneous photocatalysis: Synthesis, characterization and environmental application studies. *J Solid State Chem* **307**, (2022).

204. Tan, C. E., Su, E. C. & Wey, M. Y. Development of physicochemically stable Z-scheme MIL-88A/g-C3N4 heterojunction photocatalyst with excellent charge transfer for improving acid red 1 dye decomposition efficiency. *Appl Surf Sci* **590**, (2022).

205. Wu, Y., Luo, H. & Wang, H. Synthesis of iron(iii)-based metal-organic framework/graphene oxide composites with increased photocatalytic performance for dye degradation. *RSC Adv* **4**, 40435–40438 (2014).

206. Alvarenga, A. D., Andre, R. S., Alves, A. L. M. M. & Correa, D. S. Optimization of polyvinylpyrrolidone-SiO2 microfiber membranes for efficient water purification. *Journal of Water Process Engineering* **67**, (2024).

207. Wang, T. *et al*. Fe–O–P bond in MIL-88A(Fe)/BOHP heterojunctions as a highway for rapid electron transfer to enhance photo-Fenton abatement of enrofloxacin. *Appl Catal B* **334**, (2023).

208. Liu, N. *et al*. Ultrathin graphene oxide encapsulated in uniform MIL-88A(Fe) for enhanced visible light-driven photodegradation of RhB. *Appl Catal B* **221**, 119–128 (2018).

209. Ma, H. *et al*. Investigating the exfoliation behavior of MoS2 and graphite in water: A comparative study. *Appl Surf Sci* **512**, (2020).

210. Ma, H., Shen, Z. & Ben, S. Understanding the exfoliation and dispersion of MoS2 nanosheets in pure water. *J Colloid Interface Sci* **517**, 204–212 (2018).

211. Calisir, M. D. & Kilic, A. A comparative study on SiO2 nanofiber production via two novel non-electrospinning methods: Centrifugal spinning vs solution blowing. *Mater Lett* **258**, (2020).

212. Zheng, S. *et al*. MIL-88A grown in-situ on graphitic carbon nitride (g-C3N4) as a novel sorbent: Synthesis, characterization, and high-performance of tetracycline removal and mechanism. *Advanced Powder Technology* **31**, 4344–4353 (2020).

213. Wang, L. *et al*. The MIL-88A-Derived Fe 3 O 4 -Carbon Hierarchical Nanocomposites for Electrochemical Sensing. *Sci Rep* **5**, (2015).

214. Zhang, R., Wan, W., Qiu, L. & Zhou, Y. Facile synthesis route for MoS2-polyvinylpyrrolidone aerogels. *Mater Lett* **181**, 321–324 (2016).

215. Matysiak, W. & Tański, T. Analysis of the morphology, structure and optical properties of 1D SiO2 nanostructures obtained with sol-gel and electrospinning methods. *Appl Surf Sci* **489**, 34–43 (2019).

216. Farias, R. M. da C. *et al*. Solution blow spun silica nanofibers: Influence of polymeric additives on the physical properties and dye adsorption capacity. *Nanomaterials* **11**, (2021).

217. Fan, J. *et al*. Carbon Dots as an Electron Acceptor in the ZnIn2S4@MIL-88A Heterojunction for Enhanced Visible-Light-Driven Photocatalytic Hydrogen Evolution. *Langmuir* **39**, 12467–12475 (2023).

218. Wang, T. *et al*. Fe–O–P bond in MIL-88A(Fe)/BOHP heterojunctions as a highway for rapid electron transfer to enhance photo-Fenton abatement of enrofloxacin. *Appl Catal B* **334**, (2023).

219. Li, M. *et al*. Citric acid-modified MIL-88A(Fe) for enhanced photo-Fenton oxidation in water decontamination. *Sep Purif Technol* **308**, (2023).

220. Shao, Z. *et al*. Fabrication of MIL-88A/g-C3N4 direct Z-scheme heterojunction with enhanced visible-light photocatalytic activity. *Sep Purif Technol* **220**, 16–24 (2019).

221. Sawunyama, L., Oyewo, O. A., Seheri, N., Onjefu, S. A. & Onwudiwe, D. C. Metal oxide functionalized ceramic membranes for the removal of pharmaceuticals in wastewater. *Surfaces and Interfaces* vol. 38 Preprint at https://doi.org/10.1016/j.surfin.2023.102787 (2023).

222. Cheng, L., Zhang, Y., Fan, W. & Ji, Y. Synergistic adsorption-photocatalysis for dyes removal by a novel biochar–based Z-scheme heterojunction BC/2ZIS/WO3: Mechanistic investigation and degradation pathways. *Chemical Engineering Journal* **445**, (2022).

223. Che, L., Pan, J., Cai, K., Cong, Y. & Lv, S. W. The construction of p-n heterojunction for enhancing photocatalytic performance in environmental application: A review. *Separation and Purification Technology* vol. 315 Preprint at https://doi.org/10.1016/j.seppur.2023.123708 (2023).

224. Zhang, Y., Wang, W., Zhang, J., Liu, P. & Wang, A. A comparative study about adsorption of natural palygorskite for methylene blue. *Chemical Engineering Journal* **262**, 390–398 (2015).

225. Gómez-Pacheco, C. V., Sánchez-Polo, M., Rivera-Utrilla, J. & López-Peñalver, J. J. Tetracycline degradation in aqueous phase by ultraviolet radiation. *Chemical Engineering Journal* **187**, 89–95 (2012).

226. Acedo-Mendoza, A. G. *et al*. Photodegradation of methylene blue and methyl orange with CuO supported on ZnO photocatalysts: The effect of copper loading and reaction temperature. *Mater Sci Semicond Process* **119**, 105257 (2020).

227. Sayed, A., Mahmoud, G. A., Said, H. & Diab, A. A. Characterization and optimization of magnetic Gum-PVP/SiO2 nanocomposite hydrogel for removal of contaminated dyes. *Mater Chem Phys* **280**, 125731 (2022).

228. Zhang, R. *et al*. Enhanced photocatalytic degradation of organic dyes by ultrasonic-assisted electrospray TiO2/graphene oxide on polyacrylonitrile/β-cyclodextrin nanofibrous membranes. *Ultrason Sonochem* **70**, 105343 (2021).

229. Zhang, D. *et al*. Zr-doped TiO2 ceramic nanofibrous membranes for enhancing photocatalytic organic pollutants degradation and antibacterial activity. *Colloids Surf A Physicochem Eng Asp* **665**, (2023).

230. Li, J., Wang, S., Du, Y. & Liao, W. Enhanced photocatalytic performance of TiO2@C nanosheets derived from two-dimensional Ti2CTx. *Ceram Int* **44**, 7042–7046 (2018).

231. Nasri, M. S. I., Samsudin, M. F. R., Tahir, A. A. & Sufian, S. Effect of MXene Loaded on g-C3N4 Photocatalyst for the Photocatalytic Degradation of Methylene Blue. *Energies (Basel)* **15**, (2022).

232. Chen, Y., Xiang, Z., Wang, D., Kang, J. & Qi, H. Effective photocatalytic degradation and physical adsorption of methylene blue using cellulose/GO/TiO2hydrogels. *RSC Adv* **10**, 23936–23943 (2020).

233. Natarajan, T. S., Thomas, M., Natarajan, K., Bajaj, H. C. & Tayade, R. J. Study on UV-LED/TiO2 process for degradation of Rhodamine B dye. *Chemical Engineering Journal* **169**, 126–134 (2011).

234. Lu, X., Wang, Q. & Cui, D. Preparation and Photocatalytic Properties of g-C3N4/TiO2 Hybrid Composite. *J Mater Sci Technol* **26**, 925–930 (2010).

235. Peng, W. C. & Li, X. Y. Synthesis of MoS2/g-C3N4 as a solar light-responsive photocatalyst for organic degradation. *Catal Commun* **49**, 63–67 (2014).

236. Farag, M., El-Dafrawy, S. M. & Hassan, S. M. ZnO and C/ZnO Catalysts Synthesized via Plant Mediated Extracts for Photodegradation of Crystal Violet and Methyl Orange Dyes. *Journal of Inorganic and Organometallic Polymers and Materials* vol. 34 930–943 Preprint at https://doi.org/10.1007/s10904-023-02811-9 (2024).

APPENDIX I

Supplementary Material

3D-printed MOF/MoS_2 aerogel for dye adsorption and photocatalytic degradation

Ana Laura M.M Alves[a,b], Francisco V. dos Santos[a,c], Daniel S. Correa[a,b,c*]

[a]Nanotechnology National Laboratory for Agriculture, Embrapa Instrumentação, 13560-970, São Carlos, SP, Brazil

[b]PPGQ, Department of Chemistry, Center for Exact Sciences and Technology, Federal University of São Carlos, 13565-905, São Carlos, SP, Brazil

[c]Materials Engineering Department, São Carlos School of Engineering, University of São Paulo, 13563–120 São Carlos, SP, Brazil

Corresponding author: daniel.correa@embrapa.br

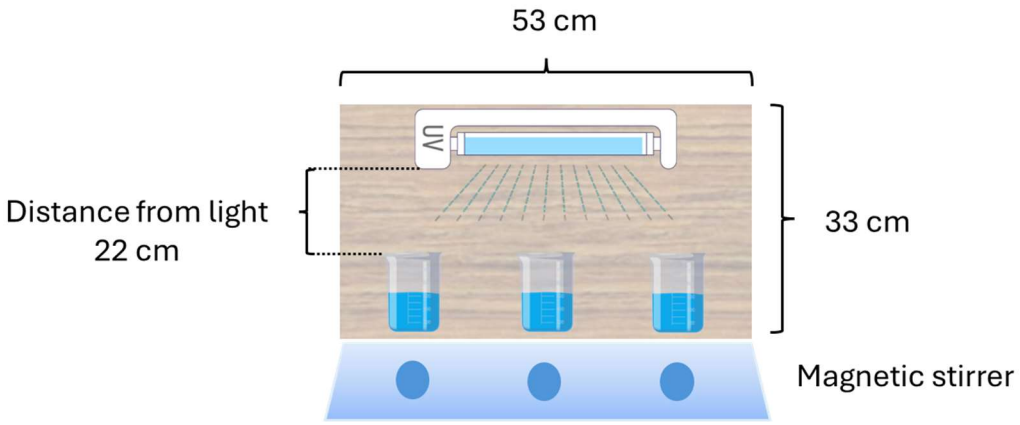

Figure S1. Scheme of the reactor used in the photodegradation tests, which used 6 UV lamps in parallel inside the test box.

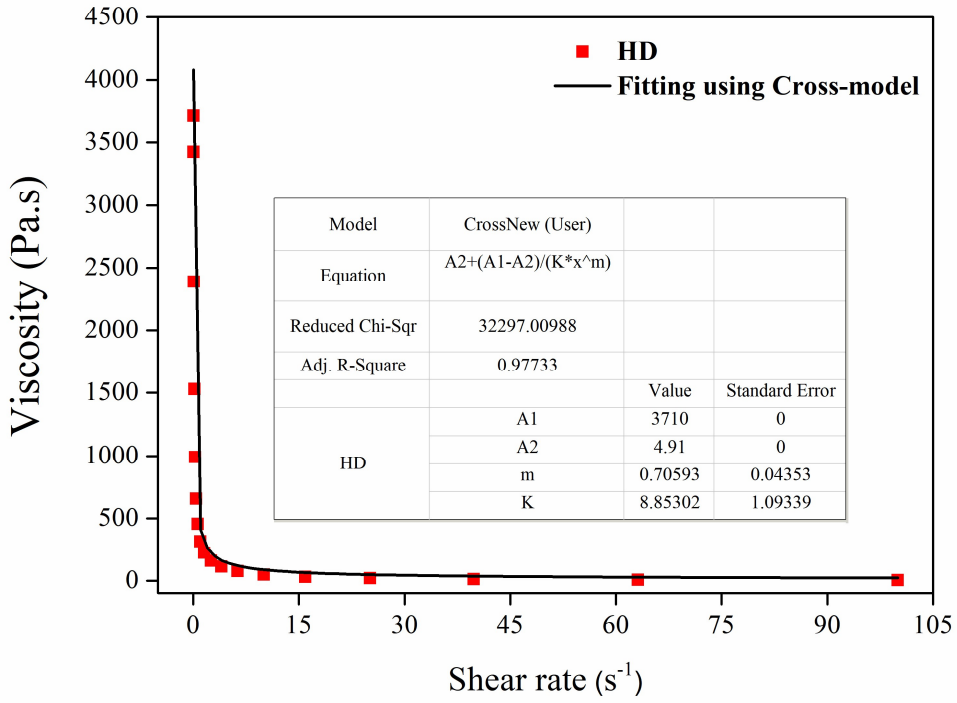

Figure S2. Adjustment of the viscosity curve as a function of the shear rate for HD ink using the Cross model, where A1 and A2 represent zero viscosity (ηo) and infinity (η∞), respectively. Reprinted with permission from dos Alves et al[109] Copyright 2024, Elsevier.

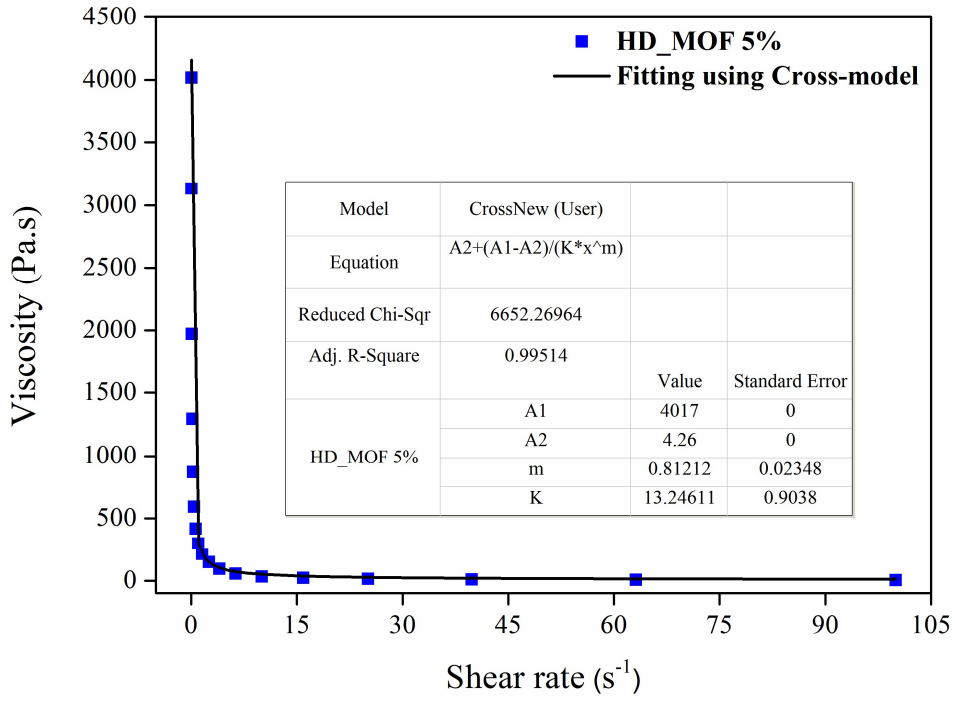

Figure S3. Adjustment of the viscosity curve as a function of the shear rate for HD/MOF/MoS_2 5 % ink using the Cross model, where A1 and A2 represent zero viscosity (ηo) and infinity (η∞), respectively. Reprinted with permission from dos Alves et al[109] Copyright 2024, Elsevier.

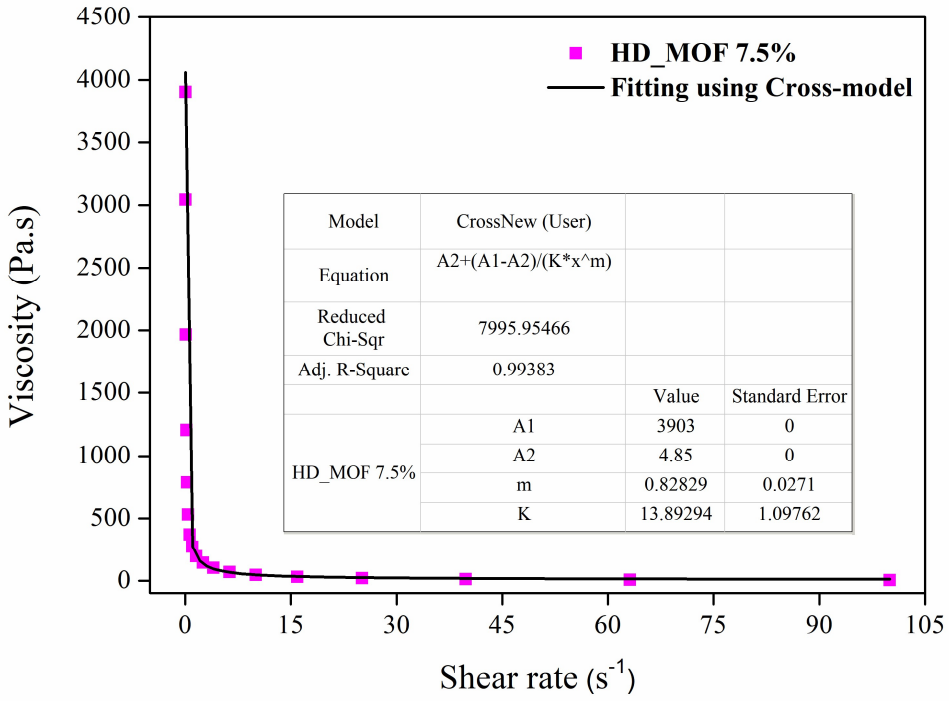

Figure S4. Adjustment of the viscosity curve as a function of shear rate for HD/MOF/MoS_2 7.5 % ink using the Cross model, where A1 and A2 represent zero viscosity (ηo) and infinity (η∞), respectively. Reprinted with permission from dos Alves et al[109] Copyright 2024, Elsevier.

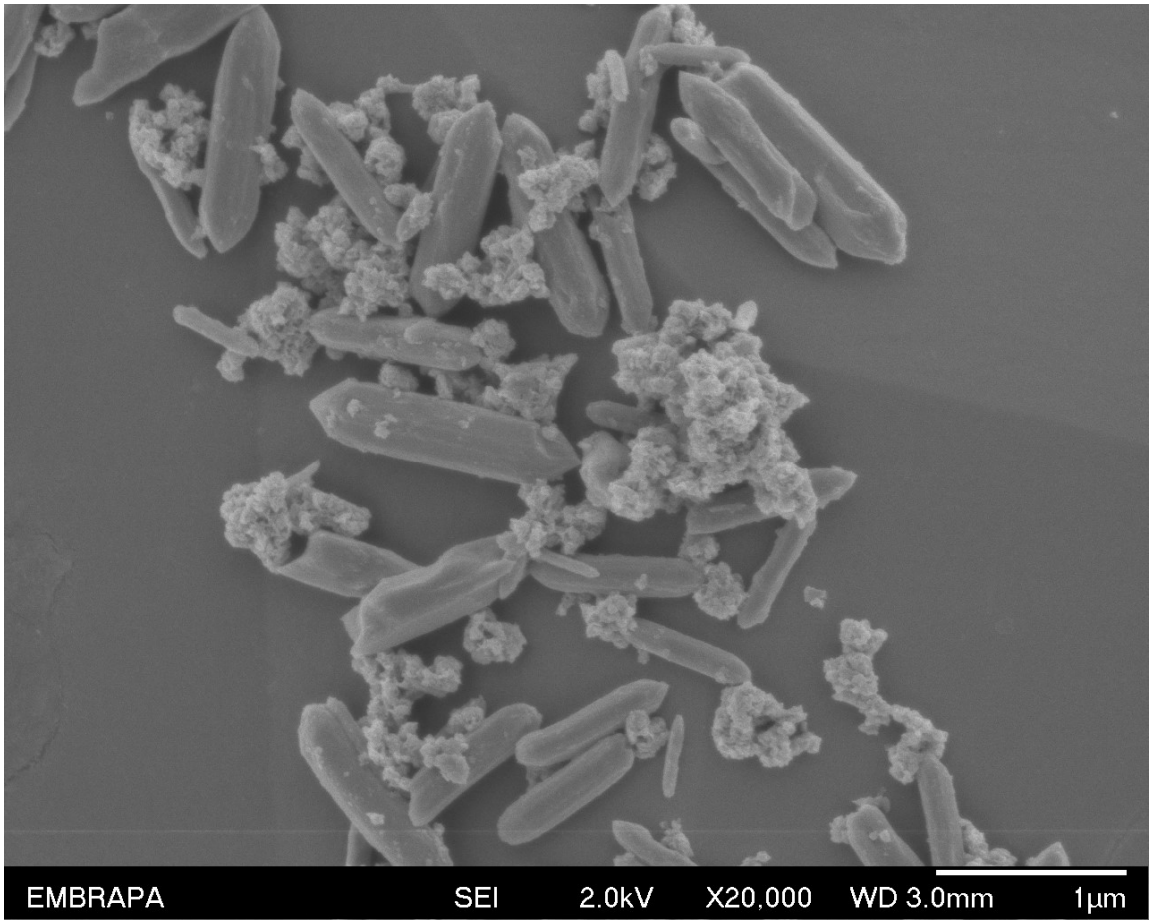

Figure S5. SEM of the produced MOF/MoS_2. Reprinted with permission from dos Alves et al[109] Copyright 2024, Elsevier.

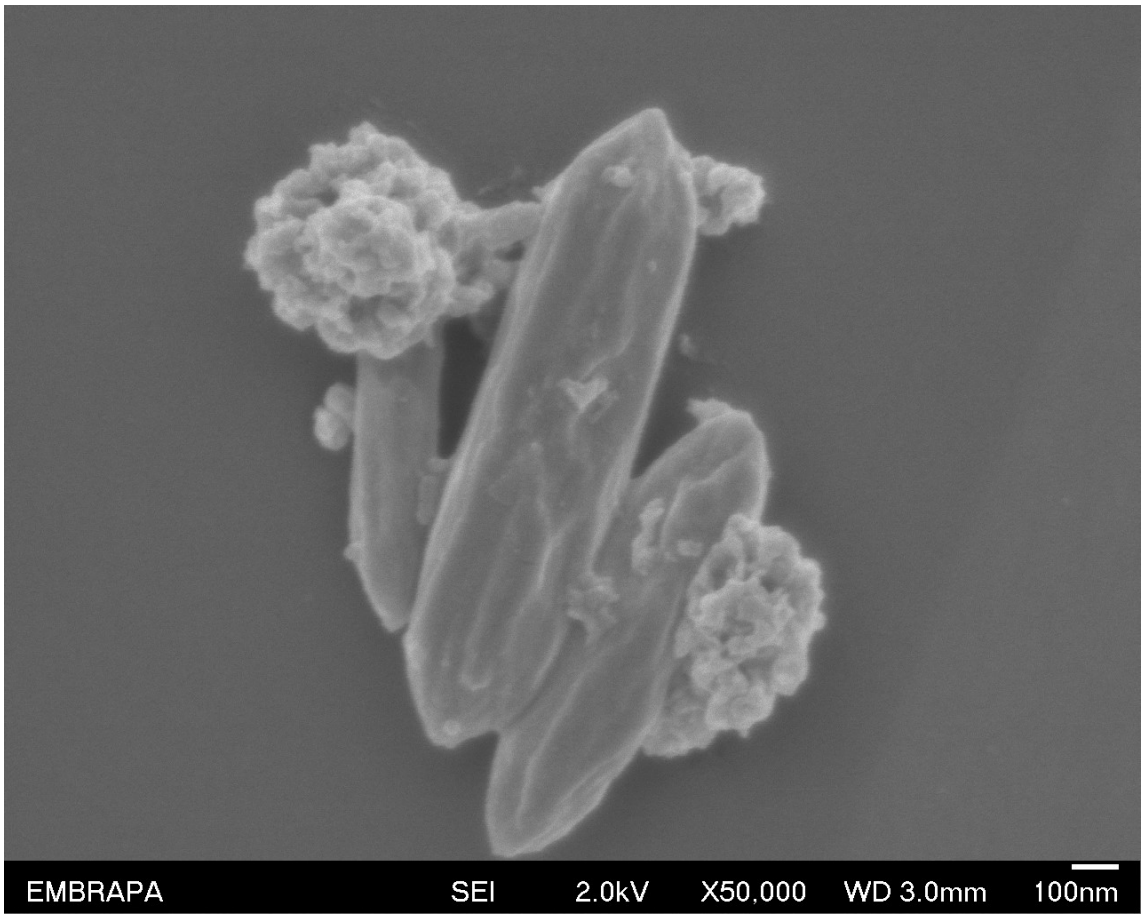

Figure S6. SEM image (50000×) of the morphology of the MOF/MoS_2. Reprinted with permission from dos Alves et al[109] Copyright 2024, Elsevier.

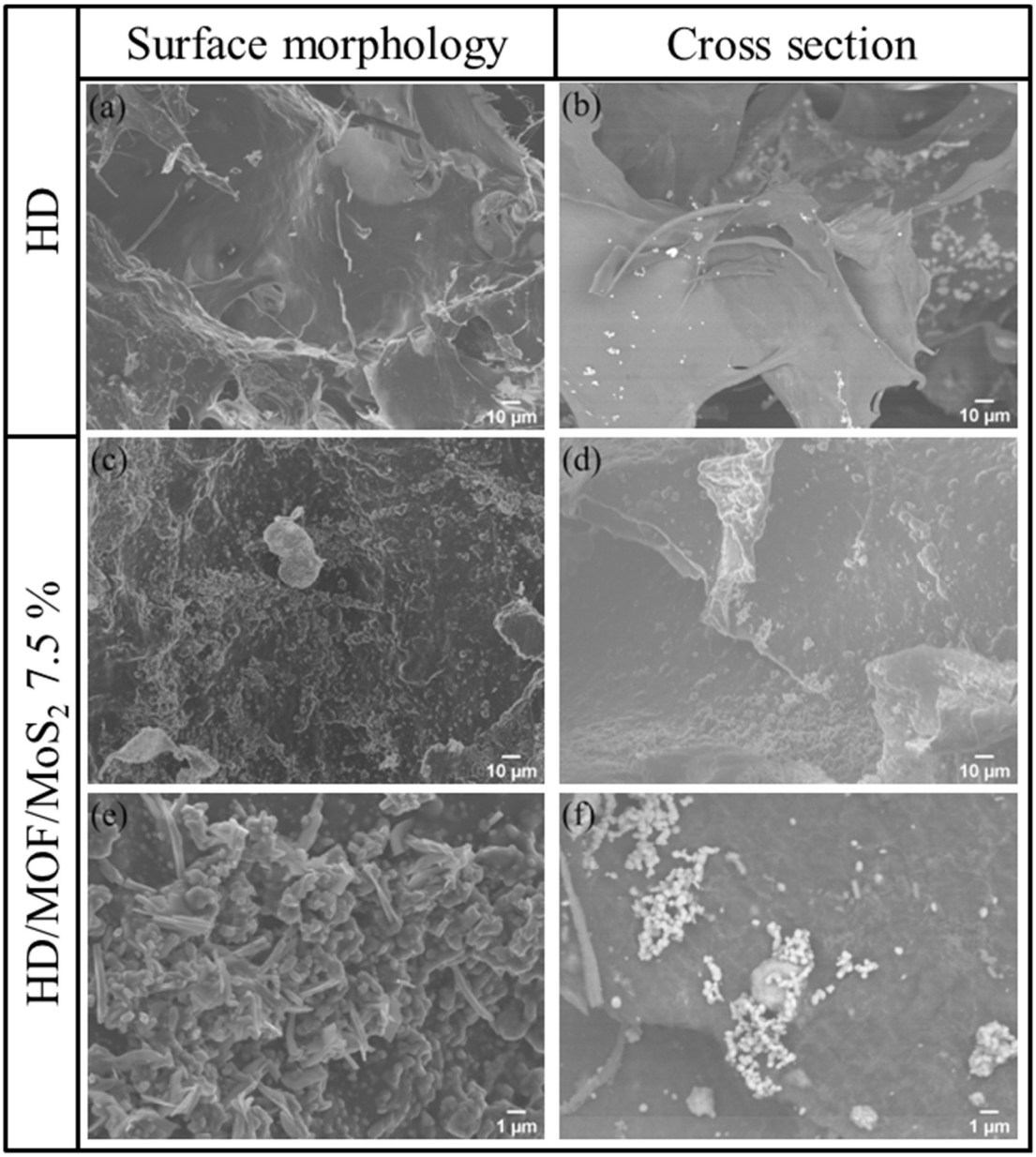

Figure S7. SEM images of HD and HD/MOF/MoS2 7.5 % printed aerogels. Reprinted with permission from dos Alves et al[109] Copyright 2024, Elsevier.

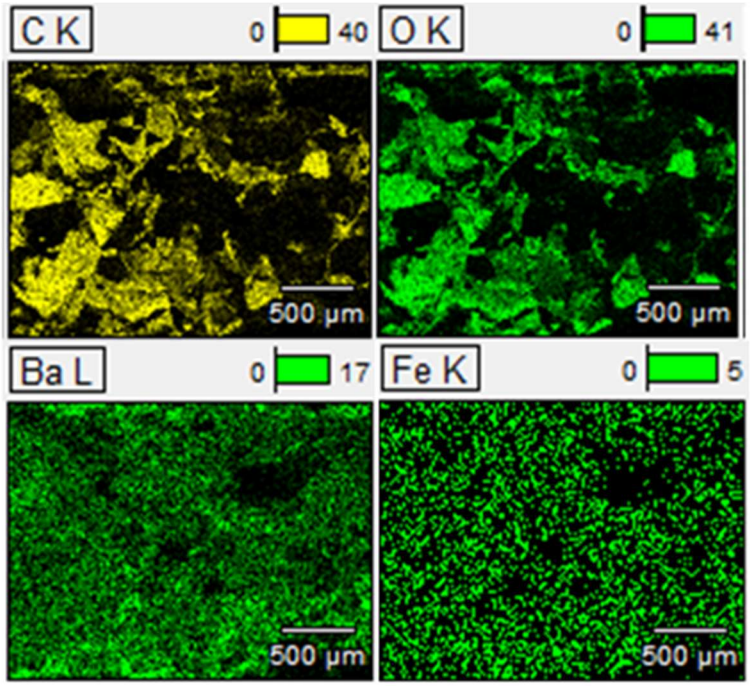

Figure S8. Elemental mapping images obtained by EDS, displaying the presence of the elements carbon, oxygen, barium, and iron in the HD/MOF/MoS_2 7.5 %. Reprinted with permission from dos Alves et al[109] Copyright 2024, Elsevier.

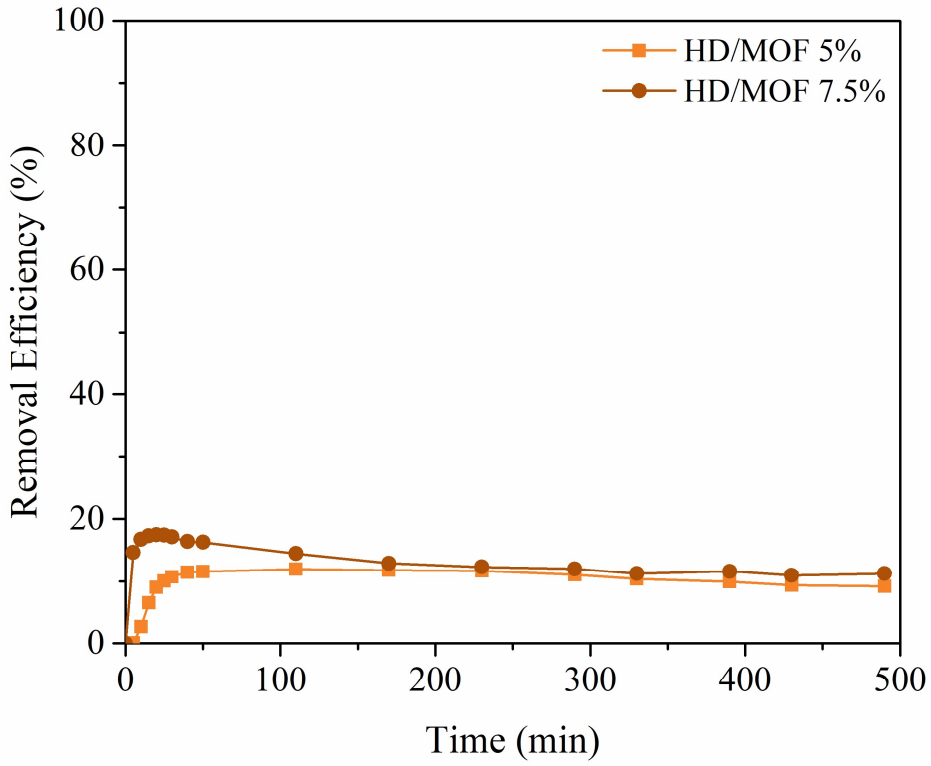

Figure S9. Removal efficiency by adsorption for HD/MOF 5 % and HD/MOF 7.5 %. Reprinted with permission from dos Alves et al[109] Copyright 2024, Elsevier.

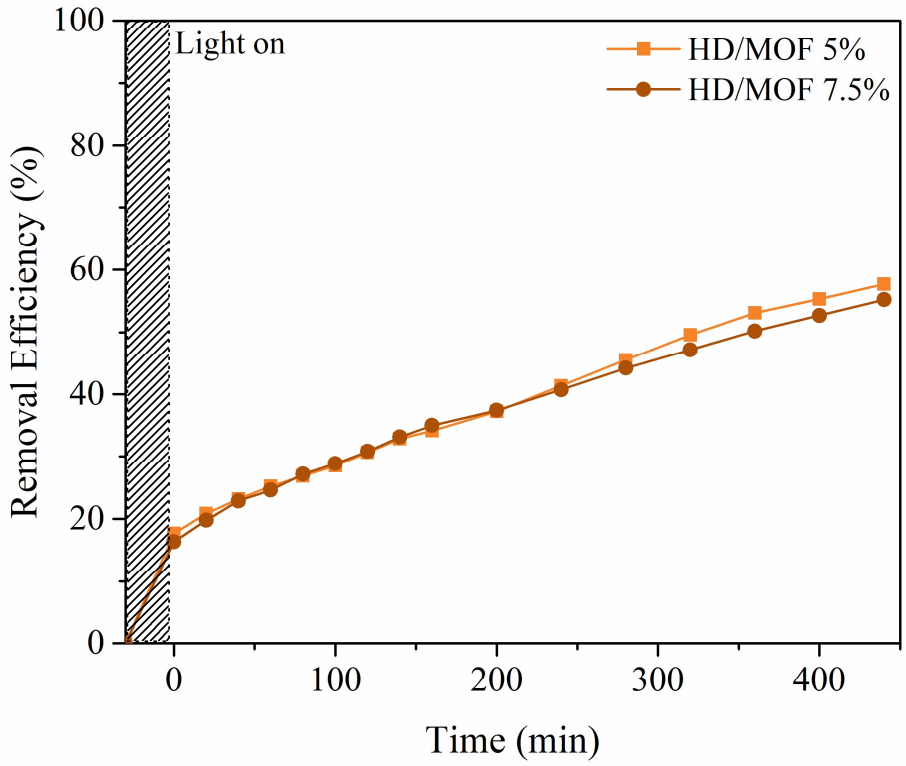

Figure S10. Removal efficiency by photocatalytic degradation for HD/MOF 5 % and HD/MOF 7.5 %. Reprinted with permission from dos Alves et al[109] Copyright 2024, Elsevier.

APPENDIX II

SUPPLEMENTARY MATERIAL

MIL88A/MoS_2 heterojuntion supported on PVP/SiO_2 fibers for mitigating environmental pollutants

Ana Laura M. M. Alves[1,2], Rodrigo Schneider[3], Rafaela S. Andre[4], Daniel S. Correa[1]

[1] Nanotechnology National Laboratory for Agriculture (LNNA), Embrapa Instrumentação, 13560-970, São Carlos, SP, Brazil

[2] PPGQ, Department of Chemistry, Center for Exact Sciences and Technology, Federal University of São Carlos (UFSCar), 13565-905, São Carlos, SP, Brazil

[3] Institut Charles Gerhardt Montpellier (ICGM), Université de Montpellier, 00034293, Montpellier, France

[4] THOTECH Soluções & Serviços LTDA, 13500-171, Rio Claro, SP, Brazil

Corresponding author: daniel.correa@embrapa.br

Table S1. Measurements of the average diameters and lengths of MOF and MOF/MoS_2. (Average of 100 measurements).

	Diameter (nm)	**Length (nm)**
MOF	119 ± 17	267 ± 41
MOF/$MoS_2$60	216 ± 46	718 ± 91
MOF/$MoS_2$100	221 ± 60	1063 ± 235

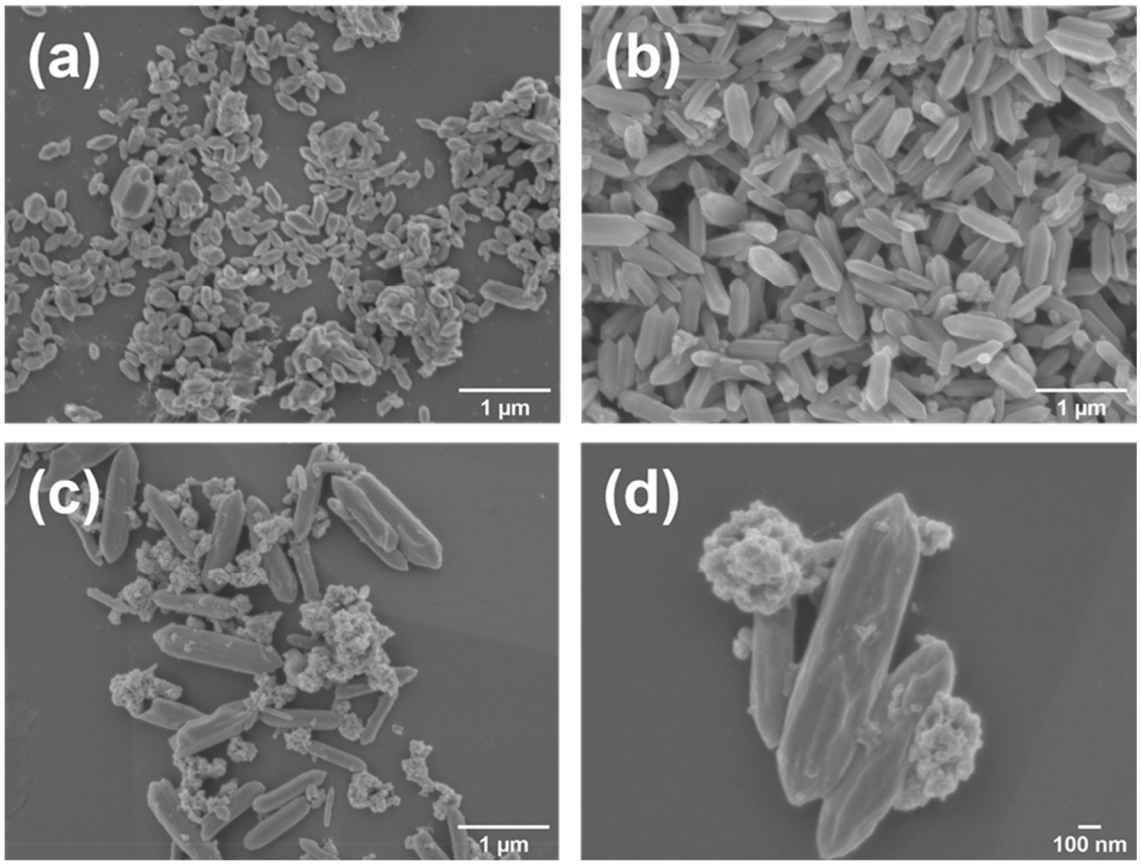

Figure S11. SEM-FEG images: (a) MOF MIL88-A; (b) MOF/$MoS_2$60; (c) and (d) MOF/$MoS_2$100. (d) is a magnified image of (c).

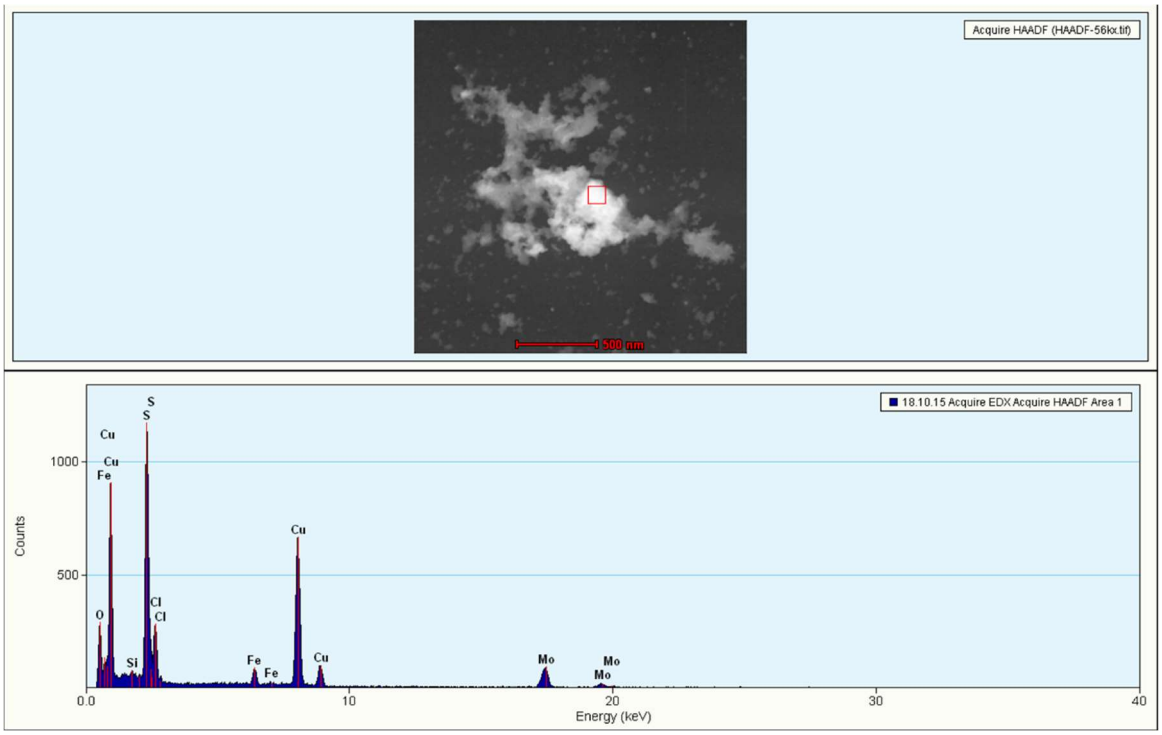

Figure S12. EDS spectra of MOF/$MoS_2$100.

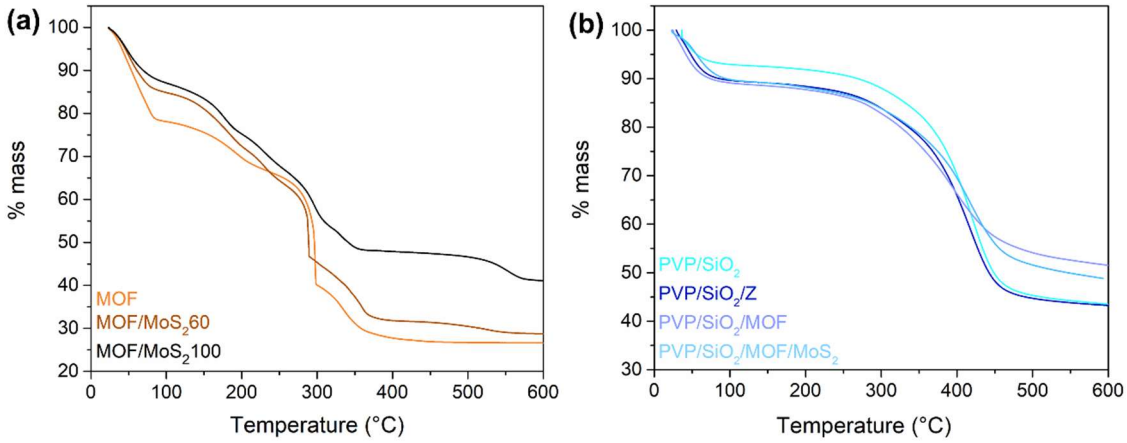

Figure S13. TGA curves of (a) MOF and MOF/MoS_2 and (b) PVP/SiO_2 fibers.

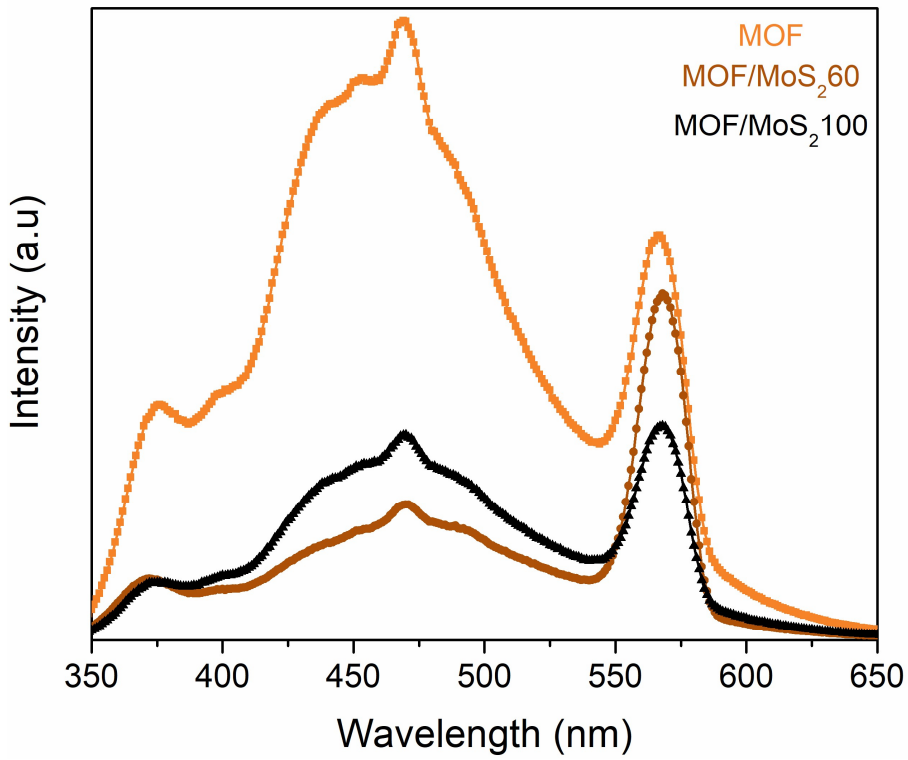

Figure S14. Photoluminescence spectra of MOF, MOF/$MoS_2$60 and MOF/$MoS_2$100.

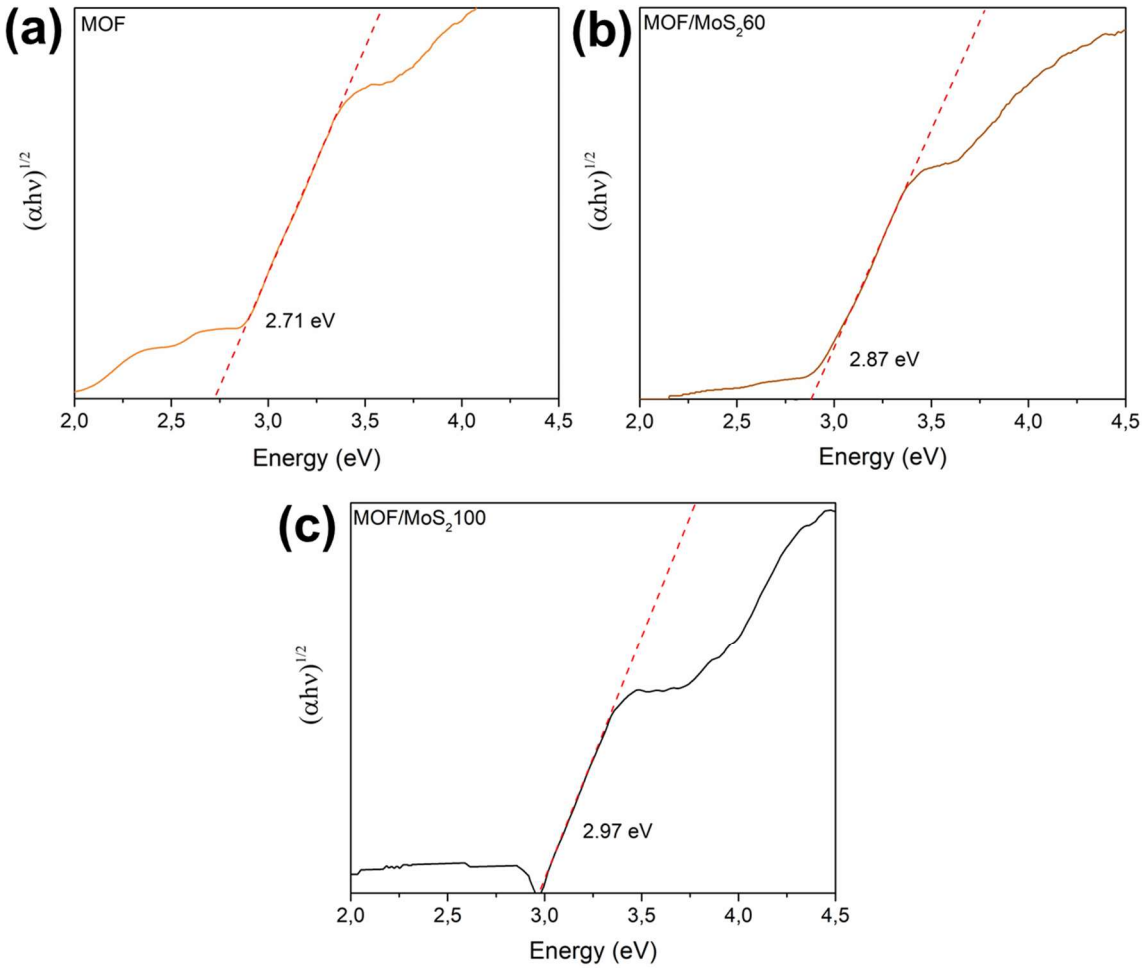

Figure S15. Tauc curves of (a) MOF; (b) MOF/$MoS_2$60 and (c) MOF/$MoS_2$100.

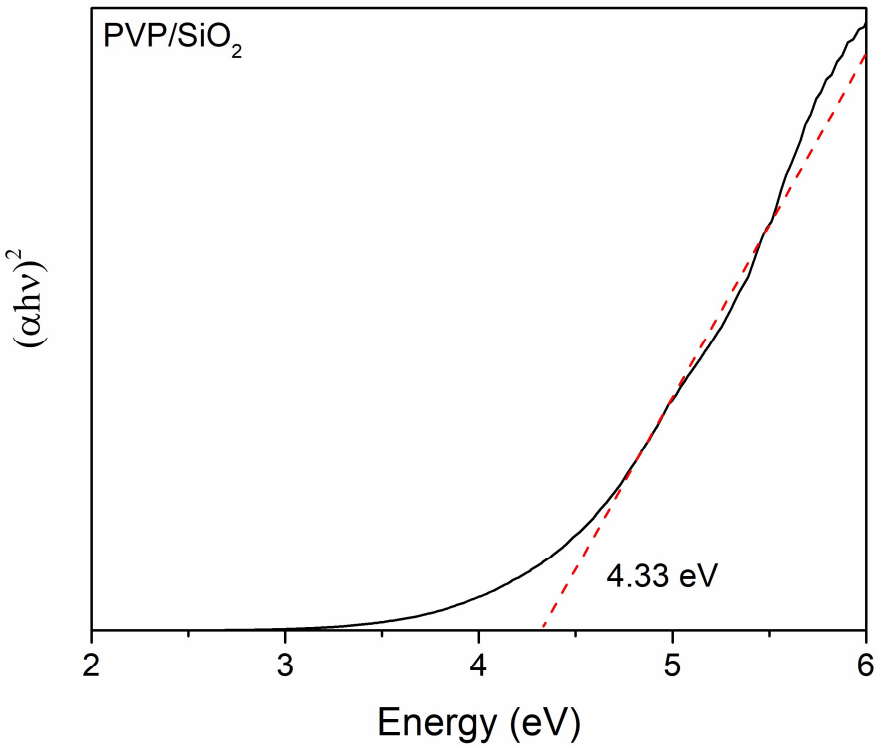

Figure S16. Tauc curve of PVP/SiO_2 fibers.

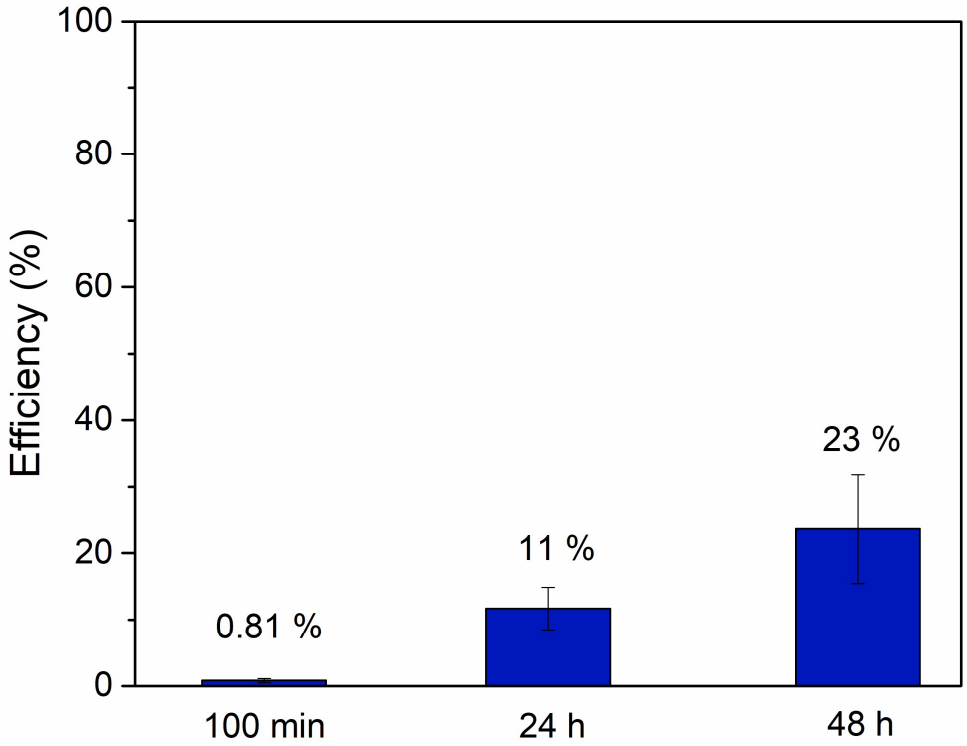

Figure S17. Photolysis results at different time intervals with MB solutions at 25 mg/L.

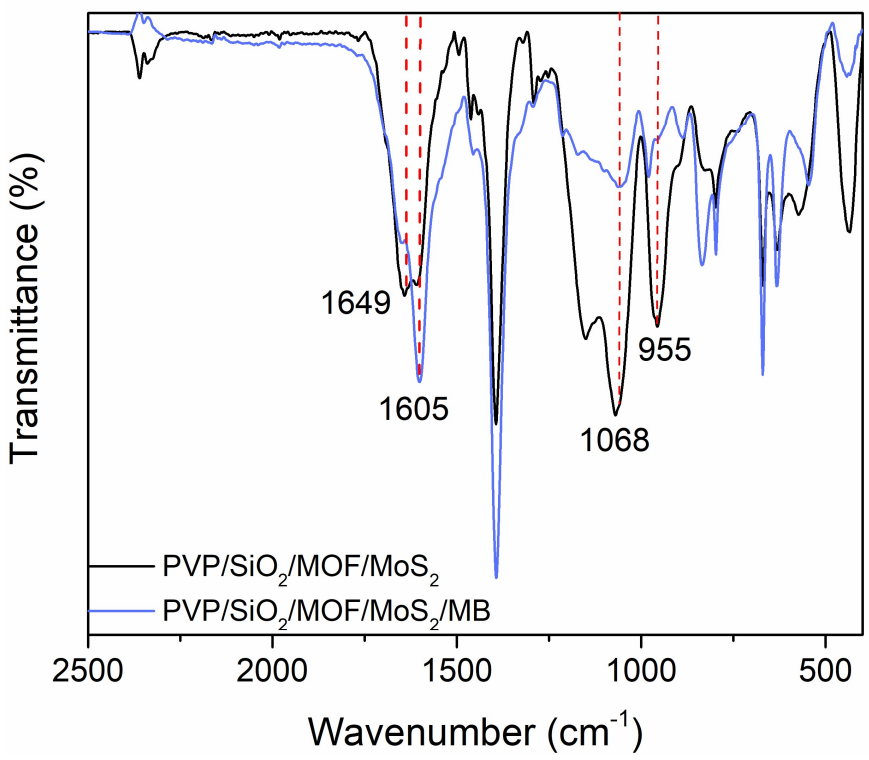

Figure S18. FTIR spectra of PVP/SiO_2 fibers before and after the adsorption process.

Anexo III

Autorizações de uso das imagens:

RightsLink

The construction of p-n heterojunction for enhancing photocatalytic performance in environmental application: A review

Author: Lin Che,Jialu Pan,Kexin Cai,Yanqing Cong,Shi-Wen Lv
Publication: Separation and Purification Technology
Publisher: Elsevier
Date: 15 June 2023

Order Completed

Thank you for your order.

This Agreement between Ana Laura Martins Mulkson Alves ("You") and Elsevier ("Elsevier") consists of your license details and the terms and conditions provided by Elsevier and Copyright Clearance Center.

Your confirmation email will contain your order number for future reference.

License Number	5933021342645
License date	Dec 20, 2024

Printable Details

Licensed Content

Licensed Content Publisher	Elsevier
Licensed Content Publication	Separation and Purification Technology
Licensed Content Title	The construction of p-n heterojunction for enhancing photocatalytic performance in environmental application: A review
Licensed Content Author	Lin Che,Jialu Pan,Kexin Cai,Yanqing Cong,Shi-Wen Lv
Licensed Content Date	Jun 15, 2023
Licensed Content Volume	315
Licensed Content Issue	n/a
Licensed Content Pages	1

Order Details

Type of Use	reuse in a thesis/dissertation
Portion	figures/tables/illustrations
Number of figures/ tables/illustrations	1
Format	both print and electronic
Are you the author of this Elsevier article?	No
Will you be translating?	No

About Your Work

Title of new work	3D PRINTED AEROGELS AND SOLUTION-BLOW SPUN FIBERS MODIFIED WITH MOF/ MoS2 FOR ADSORPTION AND PHOTODEGRADATION OF ENVIRONMENTAL CONTAMINANTS
Institution name	Federal University of São Carlos
Expected presentation date	Jan 2025

Additional Data

Portions	Figure 3
The Requesting Person / Organization to Appear on the License	Ana Laura Martins Mulkson Alves

Requestor Location

Requestor Location	Ana Alves Avenida São Carlos, 2160, Centro São Carlos, 13560001 Brazil

Tax Details

Publisher Tax ID	GB 494 6272 12

Total: 0.00 USD

CLOSE WINDOW ORDER MORE

RightsLink

The construction of p-n heterojunction for enhancing photocatalytic performance in environmental application: A review

Author: Lin Che,Jialu Pan,Kexin Cai,Yanqing Cong,Shi-Wen Lv

Publication: Separation and Purification Technology

Publisher: Elsevier

Date: 15 June 2023

Order Completed

Thank you for your order.

This Agreement between Ana Laura Martins Mulkson Alves ("You") and Elsevier ("Elsevier") consists of your license details and the terms and conditions provided by Elsevier and Copyright Clearance Center.

Your confirmation email will contain your order number for future reference.

License Number	5933030217911
License date	Dec 20, 2024

Printable Details

Licensed Content

Licensed Content Publisher	Elsevier
Licensed Content Publication	Separation and Purification Technology
Licensed Content Title	The construction of p-n heterojunction for enhancing photocatalytic performance in environmental application: A review
Licensed Content Author	Lin Che,Jialu Pan,Kexin Cai,Yanqing Cong,Shi-Wen Lv
Licensed Content Date	Jun 15, 2023
Licensed Content Volume	315
Licensed Content Issue	n/a
Licensed Content Pages	1

Order Details

Type of Use	reuse in a thesis/dissertation
Portion	figures/tables/illustrations
Number of figures/ tables/illustrations	1
Format	both print and electronic
Are you the author of this Elsevier article?	No
Will you be translating?	No

About Your Work

Title of new work	3D PRINTED AEROGELS AND SOLUTION-BLOW SPUN FIBERS MODIFIED WITH MOF/ MoS2 FOR ADSORPTION AND PHOTODEGRADATION OF ENVIRONMENTAL CONTAMINANTS
Institution name	Federal University of São Carlos
Expected presentation date	Jan 2025

Additional Data

Portions	Figure 1 (c)
The Requesting Person / Organization to Appear on the License	Ana Laura Martins Mulkson Alves

Requestor Location

Requestor Location	Ana Alves Avenida São Carlos, 2160, Centro São Carlos, 13560001 Brazil

Tax Details

Publisher Tax ID	GB 494 6272 12

Total: 0.00 USD

CLOSE WINDOW ORDER MORE

Distinguishing between type II and S-scheme heterojunction materials: A comprehensive review

Author:
D. Salazar-Marín,Goldie Oza,J.A. Díaz Real,A. Cervantes-Uribe,H. Pérez-Vidal,M.K. Kesarla,J.G. Torres Torres,S. Godavarthi

Publication: Applied Surface Science Advances

Publisher: Elsevier

Date: February 2024

RightsLink

Layer-by-layer coating of carboxymethyl chitosan-gelatin-alginate on cotton gauze for hemostasis and wound healing

Author:
Weishi Zheng,Chuntao Chen,Xujun Zhang,Xiaodong Wen,Yuanxiang Xiao,Lin Li,Qingbo Xu,Feiya Fu,Hongyan Diao,Xiangdong Liu

Publication: Surface and Coatings Technology

Publisher: Elsevier

Date: 25 January 2021

Order Completed

Thank you for your order.

This Agreement between Ana Laura Martins Mulkson Alves ("You") and Elsevier ("Elsevier") consists of your license details and the terms and conditions provided by Elsevier and Copyright Clearance Center.

Your confirmation email will contain your order number for future reference.

License Number	5933040810038
License date	Dec 20, 2024

Printable Details

Licensed Content

Licensed Content Publisher	Elsevier
Licensed Content Publication	Surface and Coatings Technology
Licensed Content Title	Layer-by-layer coating of carboxymethyl chitosan-gelatin-alginate on cotton gauze for hemostasis and wound healing
Licensed Content Author	Weishi Zheng,Chuntao Chen,Xujun Zhang,Xiaodong Wen,Yuanxiang Xiao,Lin Li,Qingbo Xu,Feiya Fu,Hongyan Diao,Xiangdong Liu
Licensed Content Date	Jan 25, 2021
Licensed Content Volume	406
Licensed Content Issue	n/a
Licensed Content Pages	1

Order Details

Type of Use	reuse in a thesis/dissertation
Portion	figures/tables/illustrations
Number of figures/ tables/illustrations	1
Format	both print and electronic
Are you the author of this Elsevier article?	No
Will you be translating?	No

About Your Work

Title of new work	3D PRINTED AEROGELS AND SOLUTION-BLOW SPUN FIBERS MODIFIED WITH MOF/ MoS2 FOR ADSORPTION AND PHOTODEGRADATION OF ENVIRONMENTAL CONTAMINANTS
Institution name	Federal University of São Carlos
Expected presentation date	Jan 2025

Additional Data

Portions	scheme 1
The Requesting Person / Organization to Appear on the License	Ana Laura Martins Mulkson Alves

Requestor Location

Requestor Location	Ana Alves Avenida São Carlos, 2160, Centro São Carlos, 13560001 Brazil

Tax Details

Publisher Tax ID	GB 494 6272 12

Total: 0.00 USD

CLOSE WINDOW ORDER MORE

RightsLink

Advances in Functional Polymer Nanofibers: From Spinning Fabrication Techniques to Recent Biomedical Applications

Author: Danilo M. dos Santos, Daniel S. Correa, Eliton S. Medeiros, et al

Publication: Applied Materials

Publisher: American Chemical Society

Date: Oct 1, 2020

PERMISSION/LICENSE IS GRANTED FOR YOUR ORDER AT NO CHARGE

This type of permission/license, instead of the standard Terms and Conditions, is sent to you because no fee is being charged for your order. Please note the following:

- Permission is granted for your request in both print and electronic formats, and translations.
- If figures and/or tables were requested, they may be adapted or used in part.
- Please print this page for your records and send a copy of it to your publisher/graduate school.
- Appropriate credit for the requested material should be given as follows: "Reprinted (adapted) with permission from {COMPLETE REFERENCE CITATION}. Copyright {YEAR} American Chemical Society." Insert appropriate information in place of the capitalized words.
- One-time permission is granted only for the use specified in your RightsLink request. No additional uses are granted (such as derivative works or other editions). For any uses, please submit a new request.

If credit is given to another source for the material you requested from RightsLink, permission must be obtained from that source.

BACK CLOSE WINDOW

RightsLink

Metal Organic Frameworks (MOFs) as Photocatalysts for the Degradation of Agricultural Pollutants in Water

Author: Yinghao Wen, Mingbao Feng, Peng Zhang, et al

Publication: ACS ES&T Engineering

Publisher: American Chemical Society

Date: May 1, 2021

PERMISSION/LICENSE IS GRANTED FOR YOUR ORDER AT NO CHARGE

This type of permission/license, instead of the standard Terms and Conditions, is sent to you because no fee is being charged for your order. Please note the following:

- Permission is granted for your request in both print and electronic formats, and translations.
- If figures and/or tables were requested, they may be adapted or used in part.
- Please print this page for your records and send a copy of it to your publisher/graduate school.
- Appropriate credit for the requested material should be given as follows: "Reprinted (adapted) with permission from {COMPLETE REFERENCE CITATION}. Copyright {YEAR} American Chemical Society." Insert appropriate information in place of the capitalized words.
- One-time permission is granted only for the use specified in your RightsLink request. No additional uses are granted (such as derivative works or other editions). For any uses, please submit a new request.

If credit is given to another source for the material you requested from RightsLink, permission must be obtained from that source.

BACK CLOSE WINDOW

RightsLink

3D-printed MOF/MoS2 aerogel for dye adsorption and photocatalytic degradation

Author: Ana Laura M.M. Alves,Francisco V. dos Santos,Daniel S. Correa

Publication: Materials Today Chemistry

Publisher: Elsevier

Date: September 2024

Journal Author Rights

BACK CLOSE WINDOW